# SEARCH FOR $W' \to e\nu$ AND $W' \to \mu\nu$ IN $\bar{p}p$ COLLISIONS AT $\sqrt{s} = 1.8$ TEV

BY

DAVID W. GERDES

DECEMBER, 1992

THE UNIVERSITY OF CHICAGO

# SEARCH FOR $W' \to e\nu$ AND $W' \to \mu\nu$ IN $\bar{p}p$ COLLISIONS AT $\sqrt{s} = 1.8$ TEV

A DISSERTATION SUBMITTED TO
THE FACULTY OF THE DIVISION OF THE PHYSICAL SCIENCES
IN CANDIDACY FOR THE DEGREE OF
DOCTOR OF PHILOSOPHY

DEPARTMENT OF PHYSICS

BY
DAVID W. GERDES

CHICAGO, ILLINOIS
DECEMBER, 1992

# ACKNOWLEDGEMENTS

Although this thesis has one name one it, its existence is possible only because of the help and support of many people. I must begin by thanking the technical staff of Fermilab, whose expertise makes doing physics with CDF possible. Thanks are also due to my colleagues on the CDF collaboration, who have provided and continue to provide a great atmosphere to work and learn. In particular, I would like to thank the members of the Electroweak Group, especially Steve Errede, Cathy Newman-Holmes, and Melissa Franklin, for their helpful comments and criticisms while this analysis was in progress. John Skarha and J. C. Yun served as diligent godparents to this analysis in its final stages, and helped see it through the review and publication process with remarkable smoothness. I would also like to thank the General Electric Foundation and the National Science Foundation for financial support, and Peter Arnold for calculating $W'$ $P_T$ distributions.

It has been my privilege to work with a number of gifted postdocs and research scientists during by time in Chicago. Many thanks to Milciades Contreras, Marshall Miller, Greg Sullivan, Carla Grosso-Pilcher, and especially to Sarah Eno and Claudio Campagnari, for their help, patience, and friendship. Also, thanks to my fellow graduate students, David Saltzberg, Jim Romano, Jinsong Wang, and Sacha Song-Kopp, for making the group an even more enjoyable place to work.

Special thanks are due to Henry Frisch, for encouraging me to join CDF and for being a friend and mentor these past few years. He is never too busy not to keep his door open and to offer words of advice and encouragement. To my advisor, Mel Shochet, many thanks are due for his help and support, and for allowing me to pursue this analysis as a thesis topic. Together, Henry and Mel have provided the group with outstanding scientific and educational leadership. Their common-sense, careful approach to problem-solving has made a deep impression on me, and is one I hope to be able to emulate.

To the many friends who have helped make my time in Chicago a most enjoyable one, more personal thanks are due. Thanks to Tim and Aprille McKay, Lynne Orr, Adam Simon, Hans Krimm, Geoff Harris, Roy Briere, Mike Leibig, Mike Booth, Markus Luty, Carlo Graziani, Aaron Roodman, Rogerio Rosenfeld, Dave Leitner, Ken Bloom, Todd Zedak, Frank Sottile, Rose Kirsch, Lou Stewart, and the members of the Little Bingo softball team—even though I understand that my number will not be retired. Thanks also to Sam and Hobbes—it's a lot easier to get to work early when your cats get you up every morning at six. Special thanks to Paul Derwent, my roommate, golf partner, colleague, and best man, for his friendship, encouragement, and Notre Dame tickets.

Finally, I would like to thank my parents and sister for their unfailing love and support. And deepest thanks of all to my wife Blair, whose love knows no limits. This thesis is dedicated to you.

# TABLE OF CONTENTS

ACKNOWLEDGEMENTS . . . . . ii

LIST OF TABLES . . . . . vi

LIST OF ILLUSTRATIONS . . . . . vii

ABSTRACT . . . . . xi

Chapter

1. INTRODUCTION . . . . . 1
   - 1.1 The Role of Symmetry . . . . . 1
   - 1.2 Parity Lost: Parity Violation in Weak Interactions . . . . . 2
   - 1.3 Parity Regained: Overview of Left-Right Symmetric Models 4
   - 1.4 Some Important Variables . . . . . 14
   - 1.5 Previous Limits . . . . . 18
   - 1.6 Outline of this Paper . . . . . 22

2. THE TEVATRON . . . . . 25
   - 2.1 Luminosity . . . . . 25
   - 2.2 Antiproton Collection . . . . . 27
   - 2.3 Collider Operation . . . . . 30

3. THE CDF DETECTOR . . . . . 32
   - 3.1 Tracking Chambers . . . . . 32
   - 3.2 Calorimeters . . . . . 37
   - 3.3 Muon Chambers . . . . . 38
   - 3.4 Luminosity Monitors . . . . . 41

4. ELECTRON AND MUON TRIGGERS . . . . . 42
   - 4.1 Hardware Triggers: Levels 0, 1, and 2 . . . . . 43
   - 4.2 Software Trigger: Level 3 . . . . . 48

5. EVENT SELECTION . . . . . 50
5.1 Production . . . . . 50
5.2 Electron Sample . . . . . 51
5.3 Muon Sample . . . . . 54
5.4 Events in the Tail . . . . . 61

6. EFFICIENCIES . . . . . 81
6.1 Muon Selection Efficiencies . . . . . 82
6.2 Electron Selection Efficiencies . . . . . 89

7. MONTE CARLO . . . . . 97
7.1 Event Generation . . . . . 98
7.2 Detector Simulation . . . . . 99
7.3 Acceptance . . . . . 108
7.4 Transverse Mass Distributions . . . . . 111

8. RESULTS . . . . . 115
8.1 Number of $W'$ Events Expected . . . . . 116
8.2 Fitting Transverse Mass . . . . . 116
8.3 Systematic Uncertainties . . . . . 123
8.4 Limits on $W'$ Production and Decay . . . . . 129
8.5 Future Prospects . . . . . 137

Appendix

A. A WORD ON JET CORRECTIONS . . . . . 139

B. TEXT OF THE $W'$ PAPER IN *PHYSICAL REVIEW LETTERS* . 151

REFERENCES . . . . . 157

# LIST OF TABLES


1. Efficiencies of cuts used in the $W' \to \mu\nu$ sample . . . . . 85
2. Efficiencies of cuts used in the $W' \to e\nu$ sample . . . . . 96
3. Number of $W' \to e\nu$ events expected in $\mathcal{L} = 4.15\ \mathrm{pb}^{-1}$ . . . . . 117
4. Number of $W' \to \mu\nu$ events expected in $\mathcal{L} = 3.54\ \mathrm{pb}^{-1}$ . . . . . 118
5. Summary of results . . . . . 136

# LIST OF ILLUSTRATIONS


1 . The Drell-Yan process of quark-antiquark annihilation. . . . . 11

2 . The $W'$ production cross section as a function of mass. . . . . 12

3 . Polar coordinate system used in the description of hadron collisions. 15

4 . Transverse mass distribution for the process $W \rightarrow e\nu$. . . . . 19

5 . $W_R$ mass limits. . . . . 21

6 . Two of the box diagrams responsible for the $K_L$–$K_S$ mass difference. 23

7 . The Fermilab accelerator complex. . . . . 28

8 . Highly schematic view of the Stochastic Cooling system. . . . . 29

9 . Energy distribution of antiprotons in the Accumulator ring as a function of time. . . . . 30

10. Cutaway view of one half of the CDF detector. . . . . 33

11. Perspective view of the CDF detector. . . . . 34

12. End view of the Central Tracking Chamber. . . . . 36

13. A central calorimeter wedge. . . . . 37

14. View of a central calorimeter wedge, showing the location of the central muon chambers. . . . . 39

15. View of the four planes of drift chambers in a 15-degree central muon module. . . . . 40

16. Beam's-eye view of one of the beam-beam counters. . . . . 41

17. Electron identification variables. . . . . 55

18. Observed transverse mass distribution for the electron sample. . . . 56

19. Muon identification variables. . . . . 60

20. Observed transverse mass distribution for the muon sample. . . . . 62

21. Total transverse energy contained in jets for events in the muon sample. . . . . 63

22. Transverse mass distributions for events in the muon sample with $\sum E_T(jet)$ greater than 30 GeV (left) and less than 30 GeV (right). 64

23. Event vertex distribution for events with $M_T$ less than 120 GeV (left) and greater than 120 GeV (right). . . . . 65

24. Impact parameter distribution for events with $M_T$ less than 120 GeV (left) and greater than 120 GeV (right). . . . . 66

25. EM energy in the calorimeter tower traversed by the muon candidate, for events with $M_T$ less than 120 GeV (left) and greater than 120 GeV (right). . . . . 66

26. Hadronic energy in the calorimeter tower traversed by the muon candidate, for events with $M_T$ less than 120 GeV (left) and greater than 120 GeV (right). . . . . 67

27. Transverse energy in the calorimeter towers surrounding the tower traversed by the muon candidate, for events with $M_T$ less than 120 GeV (left) and greater than 120 GeV (right). . . . . 68

28. Muon pseudorapidity distribution for events with $M_T$ less than 120 GeV (left) and greater than 120 GeV (right). . . . . 69

29. Azimuthal angle $\phi$ distribution for events with $M_T$ less than 120 GeV (left) and greater than 120 GeV (right). . . . . 69

30. $R$-$\phi$ distance between the extrapolated CTC track and the track segment in the muon chambers, for events with $M_T$ less than 120 GeV (left) and greater than 120 GeV (right). . . . . 70

31. Axial vs. stereo $\chi^2$ for the muon track, for events with $M_T$ less than 120 GeV (left) and greater than 120 GeV (right). . . . . 70

32. Curvature error for events with $M_T$ less than 120 GeV (left) and greater than 120 GeV (right). . . . . 71

33. Time-of-flight measurements for muon candidate tracks, as determined from the hadron TDC's. . . . . 72

34. Comparison of electron-neutrino transverse mass derived from calorimeter information, and from tracking information alone. . . . . 74

35. Number of jets per event in the muon and electron samples. . . . . 75

36. Lepton $P_T$ distributions for the electron and and muon samples. . . 76

37. Distribution of $E_T$ in the underlying event for the electron and muon samples. . . . . 77

38. Monte Carlo transverse mass distributions for misidentified $Z \rightarrow \mu\mu$ events. . . . . 80

39. Dimuon invariant mass distribution for the $Z \to \mu^+\mu^-$ sample used to determine the muon identification efficiencies. . . . . 84
40. Distributions of the cut variables for muons in the efficiency sample. 86
41. Energy in random cones for events in the $W' \to \mu\nu$ sample. . . . . 87
42. $E/P$ distributions for electrons from $W$ decay—data and Monte Carlo. 92
43. $E/P$ distributions for $W'$'s of mass 125, 200, 350, and 500 GeV, as determined from the radiative Monte Carlo. . . . . 93
44. Efficiency of the $E/P$ cut versus $W'$ mass. . . . . 94
45. Border tower energy distributions for $W'$'s of mass 125, 200, 350, and 500 GeV, as determined from the radiative Monte Carlo. . . . . 95
46. Efficiency of the border tower energy cut versus $W'$ mass. . . . . 96
47. Measured $W$ boson $P_T$ distribution at CDF, together with the QCD prediction. . . . . 101
48. $P_T$ distributions for $W$, 125 GeV $W'$, and 200 GeV $W'$ bosons. . . . 102
49. Decomposition of the observed underlying event vector. . . . . 104
50. Scatter plots of the reconstructed $u_\perp$ (left) and $u_\parallel$ (right) versus the generated $P_T$ of the $W$. . . . . 105
51. The reconstructed perpendicular component of the underlying event, $u_\perp$, for various intervals of $P_{T,W}$. . . . . 106
52. Fit of $\sigma_{u_\perp}$ as a function of $P_T$. . . . . 107
53. Fit of $u_\parallel$ as a function of $P_T$. . . . . 107
54. Difference between the actual and fitted values of $u_\parallel$ for various intervals of $P_{T,W}$. . . . . 109
55. Geometrical and kinematic acceptance for the decays $W' \to e\nu$ and $W' \to \mu\nu$, as a function of $M_{W'}$. . . . . 110
56. Monte Carlo transverse mass distributions for $W$ and $W'$ decays in the electron channel. . . . . 112
57. Monte Carlo transverse mass distributions for $W$ and $W'$ decays in the muon channel. . . . . 113
58. Transverse mass of $Z \to e^+e^-$ events with one electron removed. . . 114
59. A 300 GeV $W'$ as it would appear in the electron sample if present with standard-strength couplings. . . . . 119
60. Probability distribution for the $W'$ fraction $\alpha$ in the muon sample, for $M_{W'}$ = 125 GeV and 300 GeV. . . . . 121

61. Effect of varying the $W$ $P_T$ distribution. . . . . 124

62. Probability distributions for a 250 GeV $W'$ in the muon channel, before and after smearing. . . . . 127

63. Probability distributions for a 250 GeV $W'$ in the muon channel, before and after smearing. . . . . 128

64. 95% confidence-level limits on $\sigma \cdot B(W' \to e\nu)$ and $\sigma \cdot B(W' \to \mu\nu)$. 130

65. 95% confidence-level limits on the ratio of $\lambda^2 B$ to its standard-strength value, in the electron and muon channels. . . . . 131

66. Smeared electron, muon, and combined probability distributions for $M_{W'} = 250$ GeV. . . . . 133

67. 95% confidence-level limits on the $W'$ cross section times branching ratio in the electron, muon, and combined channels. . . . . 134

68. 95% confidence-level limits on the ratio of $\lambda^2 B$ to its nominal value of 1/12, for the electron, muon, and combined channels. . . . . 135

69. Prospective $W'$ limit versus integrated luminosity. . . . . 138

70. Uncorrected energy of the highest-$E_T$ jet for events in the electron sample. . . . . 142

71. Jet correction factor versus jet $\eta$. . . . . 143

72. Difference in $M_T$ for events in the electron sample before and after jet and underlying event corrections. . . . . 144

73. Difference in $M_T$ for events in the electron sample before and after corrections, for various intervals of uncorrected $\sum E_T(jet)$. . . . . 145

74. Difference in $M_T$ for events in the muon sample before and after jet and underlying event corrections. . . . . 146

75. Difference in $M_T$ for events in the muon sample before and after corrections, for various intervals of uncorrected $\sum E_T(jet)$. . . . . 147

76. Comparison of $M_T$ distributions for the electron sample before and after jet and underlying event corrections. . . . . 149

77. Comparison of $M_T$ distributions for the muon sample before and after jet and underlying event corrections. . . . . 150

# ABSTRACT

The $W'$ is a hypothetical charged, heavy, vector boson that appears in some attempts to extend the gauge group of the standard model. This thesis describes a search for such an object by looking for its decay to an electron or muon and a neutrino, using data collected with the Collider Detector at Fermilab during the 1988–89 Tevatron collider run. The nonobservation of these processes leads to limits on the production cross section times the leptonic branching ratio, limits which constrain the presence of a right-handed scale in weak interactions. Assuming that the $W'$ has standard-strength couplings to three generations of light fermions, we find that $M_{W'} > 520$ GeV at the 95% confidence level.

# CHAPTER 1

# INTRODUCTION

> I hold that the chief merit of a theory is, that it shall guide experiment, without impeding the progress of the true theory when it appears.
>
> James Clerk Maxwell, *On Faraday's Lines of Force*

This thesis describes a search for new heavy, charged, vector bosons, denoted $W'$. Such particles are predicted to exist by some attempts to extend the gauge group of the standard model. In particular, $W'$'s are a prediction of models that restore left-right symmetry at some high energy scale $\Lambda \sim M_{W'}$. To understand why such models are attractive and well-motivated, and therefore why a search like this is worth undertaking, let us begin with a discussion of the central role that symmetry has come to play in modern physics, and how a major symmetry was overturned by the surprising discovery that weak interactions violate parity.

## 1.1 The Role of Symmetry

Perhaps the chief accomplishment of modern physics has been the discovery of symmetry as nature's central organizing principle. Beginning with the spatial and temporal invariances of classical mechanics, physicists have gone on to enumerate the deeper and more abstract symmetries that form the basis for our current understanding of the world: the Lorentz invariance of special relativity and the "general

covariance" of the general theory; discrete symmetries such as charge conjugation, parity, and time reversal, which are tied together with profound consequences by the CPT theorem; the unbroken gauge symmetry of electromagnetism and its non-abelian cousin, the strong force; and the broken symmetry of the weak interaction. The search for more encompassing symmetry principles continues to animate both theorists and experimentalists alike. It is what leads theorists to postulate grand unified theories based on larger and larger groups, and to speculate that major unsolved problems remain unsolved for lack of the appropriate symmetry principle. Such problems may include the origin of fermion masses, the vanishing of the cosmological constant, and the question of why there are apparently three generations of fermions. It is also what drives experimentalists to seek relics of the primordial symmetry in the halos of galaxies, to spend years at the bottom of mineshafts looking for decaying protons, and to construct gigantic accelerators and complicated detectors like CDF. The search for a higher symmetry to shed light on another puzzle, the left-handed character of the weak interaction, is what motivates the work described in this thesis.

## 1.2 Parity Lost: Parity Violation in Weak Interactions

That the weak interaction violates parity conservation—that is, prefers left to right—has been known since 1956, when the so-called $\tau$–$\theta$ paradox was resolved by T. D. Lee and C. N. Yang. The "paradox" was this: two particles, the $\tau$ and the $\theta$, were observed to have the same mass, spin, lifetime, and production properties, and seemed to differ only in that one decayed into two pions ($\pi^{\pm}\pi^{0}$) while the other decayed into three (either $\pi^{\pm}\pi^{+}\pi^{-}$ or $\pi^{\pm}\pi^{0}\pi^{0}$). The $2\pi$ and $3\pi$ final states have opposite parity, and it was a mystery why two otherwise identical particles should be distinguished in this respect alone. Lee and Yang proposed[1] that the $\tau$ and the $\theta$ were really the same particle (today we know it as the $K^{\pm}$); both the $2\pi$ and $3\pi$

decays were allowed because of a parity-violating component of the weak interaction. They suggested several experiments that would detect this parity violation. Shortly thereafter, C. S. Wu[2] confirmed their hypothesis with an explicit demonstration of parity violation in the beta decay of $^{60}$Co. Subsequently, Goldhaber and Sunyar[3], in an ingenious and beautiful experiment, showed that the neutrino is purely left-handed: there are no right-handed neutrinos produced in weak decays. The weak interaction, therefore, not only violated parity, it did so "maximally."

We have just claimed that modern physics has made a steady progression towards deeper and deeper symmetries, but parity violation seems more like a retreat from symmetry than any sort of progress. Indeed, many found the abandonment of a fundamental spacetime symmetry extremely disturbing. However, the maximal nature of the phenomenon gave a clue that something deeper might be at work. That "something deeper" turned out, about a decade later, to be what we now know as the standard model of electroweak interactions[4, 5, 6]. The standard model "unifies" the weak and electromagnetic interactions under the banner of the $SU(2)_L \times U(1)_Y$ gauge group. (The term "unifies" is used advisedly because the theory contains two independent coupling constants, one associated with the $SU(2)$ generators and one with the $U(1)$. A truly unified theory would presumably contain only one gauge coupling.) The $SU(2)$ acts on left-handed doublets of quarks and leptons, while the right-handed components transform trivially, as scalars, which is another way of saying that right-handed particles do not participate in the weak interaction. (Actually, weak neutral current processes can involve right-handed interactions, but these are outside the scope of the work we will describe, which is confined to charged-current weak processes.) The left-handedness of the weak interaction is thus built into the fundamental gauge structure of the standard model, a theory that has put together over two decades of outstanding successes. Among its many achievements are the correct prediction of the masses and lifetimes of the $W$ and $Z$ bosons, the charged and neutral carriers of the weak interaction.

Nevertheless, there is something unsatisfying about all this. Parity violation is happily accommodated by the standard model, but is not really *explained* by it. The standard model offers no guidance on the question of why nature chose a left-handed world to begin with, rather than a right-handed one or a symmetric one. It presents us with a gauge group that explains the data—which of course is a feat that the entire previous generation of theories was unable to accomplish—but does not attempt to explain where such a group could have come from. Because of this apparent incompleteness, and because, guided by symmetry precepts, many physicists continued to find the idea of a fundamentally left-handed world unpalatable, a class of theories soon arose[7, 8, 9] in which left-right symmetry is restored at higher energy scales. In this view, the standard model, with its built-in parity violation, emerges as the low-energy limit of the underlying symmetric theory. Admittedly, left-right symmetry is every bit as "hardwired" into these theories as left-right *a*symmetry is hardwired into the standard model—to which partisans of left-right symmetry can only reply that it is prettier that way.

## 1.3 Parity Regained: Overview of Left-Right Symmetric Models

Let us now describe these models in more detail, with the aim of showing how the breakdown of left-right symmetry leads to new charged and neutral gauge bosons with large masses. We will also show that the theory requires the presence of right-handed neutrinos, which may themselves be quite massive. The reader is assumed to have some familiarity with symmetry-breaking as it occurs in the standard model[10], but for the sake of completeness, and to motivate what follows, we will briefly review it here.

### 1.3.1 Symmetry Breaking in the Standard Model

The Lagrangian of any gauge theory can be written quite generally as

$$\mathcal{L} = \mathcal{L}_{kin}^{gauge} + \mathcal{L}_{kin}^{matter} + \mathcal{L}_{kin}^{Higgs} + \mathcal{L}_{Yukawa} - V(\phi),$$

where $\phi$ is the Higgs field (or fields) and $V(\phi)$ is the Higgs potential, the minima of which determine the ground state of the theory. Note that there are no mass terms for the gauge or matter fields—such terms would explicitly break gauge invariance. Mass terms arise "spontaneously" if the minimum of $V(\phi)$ (call it $v$) occurs for nonzero values of the field $\phi$. In that case, one defines a new field, $\phi'$, that has a vacuum expectation value of zero, and rewrites the Lagrangian in terms of the shifted field. For example, a typical Yukawa term can be expressed as

$$\begin{aligned} f\bar{\psi}\psi\phi &= f\bar{\psi}\psi(\phi' + v) \\ &= fv\bar{\psi}\psi + f\bar{\psi}\psi\phi', \end{aligned}$$

which now includes a mass term for a fermion with mass $fv$. In the limit where $v$ approaches zero, the fermion becomes massless.

Mass terms for the gauge fields arise in a way that is only slightly more complicated. They come about when the kinetic term for the Higgs field,

$$\mathcal{L}_{kin}^{Higgs} = |D_\mu \phi|^2,$$

is rewritten in terms of the shifted field. In the standard model, the gauge-covariant derivative $D_\mu$ is

$$D_\mu = \partial_\mu - \frac{ig}{2}\tau \cdot \mathbf{W}_\mu - \frac{ig'}{2}B_\mu,$$

where $\mathbf{W}_\mu$ is the triplet of gauge fields associated with $SU(2)_L$, $B_\mu$ is the $U(1)$ gauge field, and $g$ and $g'$ are the coupling constants. This operator acts on the standard model Higgs field, which is a doublet of complex fields

$$\phi = \begin{pmatrix} \phi^+ \\ \phi^0 \end{pmatrix}.$$

The Higgs potential $V(\phi)$ is chosen such that $\phi$ has a minimum at

$$\phi_0 = \frac{1}{\sqrt{2}} \begin{pmatrix} 0 \\ v \end{pmatrix}.$$

Inserting $\phi' = \phi - \phi_0$ and writing out the expression for $|D_\mu \phi|^2$, we obtain a term

$$\frac{1}{8} v^2 \left[ g^2 W_\mu^+ W^{-\mu} + (g W_{3\mu} - g' B_\mu)^2 \right],$$

where $W^\pm = \frac{1}{\sqrt{2}}(W_1 \pm i W_2)$. This expression can be made a little clearer by defining the normalized field

$$Z_\mu^0 = \frac{1}{\sqrt{g^2 + g'^2}} (g W_{3\mu} - g' B_\mu).$$

Then we are left with the terms

$$\frac{1}{2} M_W^2 W_\mu^+ W^{-\mu} + \frac{1}{2} M_{Z^0}^2 Z_\mu^0 Z^{0\mu},$$

where $M_W = vg/2$ and $M_{Z^0} = \frac{1}{2} v \sqrt{g^2 + g'^2}$. These are the mass terms for the $W$ and $Z^0$ bosons, and they lead to the famous relation

$$1 - \frac{M_W^2}{M_{Z^0}^2} = \frac{g'^2}{g'^2 + g^2} = \sin^2 \theta_W,$$

where $\theta_W$ is the weak mixing angle or Weinberg angle. No mass term appears for the orthogonal combination

$$A_\mu = \frac{1}{\sqrt{g'^2 + g^2}} (g' W_{3\mu} + g B_\mu),$$

which becomes the massless photon.

We note that the masses of the gauge bosons depend on three free parameters of the theory: $g, g'$, and $v$. These parameters in turn can be inferred from measurements of $\alpha$ (in any electromagnetic process), $G_F$ (in muon decay), and $\sin^2 \theta_W$ (in neutral current processes). The latter measurement is the most difficult to make, but it was finally done in experiments beginning in 1973[11]. The knowledge of all three of these parameters allowed the masses of the $W$ and $Z^0$ to be predicted with reasonable confidence in advance of their discovery at CERN in 1983[12, 13, 14].

We emphasize that this prediction was possible because the number of parameters involved is small and because they all have large, measurable effects on low-energy processes. As we shall now see, the situation is less favorable for left-right symmetric models.

### *1.3.2 Gauge Boson Masses in Left-Right Symmetric Models*

Most models with left-right symmetry are based on the group $SU(2)_L \times SU(2)_R \times U(1)_{B-L}$. The $SU(2)$ generators couple to left- and right-handed fermion doublets, while the $U(1)$ generator couples to $B - L$, baryon number minus lepton number. (The fact that the appropriate U(1) generator for this class of models turns out to be $B - L$ is an appealing feature, as it points to a deeper symmetry between quarks and leptons. By contrast, the $U(1)$ generator in the standard model, "weak hypercharge," does not appear to have any physical significance, the quantum numbers being merely handed out *post facto* to ensure the correct electromagnetic charge assignments and the cancellation of anomalies.) The left- and right-handed $SU(2)$ groups may either be fundamental or may arise at some intermediate stage of symmetry breaking in a theory with still higher symmetry. For example, in grand unified theories based on $SO(10)$, $SO(10)$ may break down to $SO(6) \times SO(4)$. The physics arising from the $SO(4)$ is identical to that coming from $SU(2)_L \times SU(2)_R$, if the two coupling constants $g_L$ and $g_R$ are equal, as is the case with true left-right symmetry. In what follows we shall assume $g_L = g_R = g$.

The pattern of symmetry breaking is now more complicated[15] and requires additional Higgs multiplets. The minimal model (more elaborate variants are possible) contains three such multiplets, $\Delta_R$, $\Delta_L$, and $\phi$, whose minima are arranged to ensure the correct pattern of symmetry-breaking—that is, a pattern whose end result is the low-energy, left-handed world we know. The field $\Delta_R$ controls the breaking of right-handed symmetry, while the fields $\Delta_L$ and $\phi$ govern the subsequent breaking

of left-handed and $B - L$ symmetry. The $W'$ gets its mass at the first stage:

$$M_{W'} = g v_R,$$

where $v_R$ is related to the minimum of $\Delta_R$. By contrast, the ordinary $W$ boson gets its mass at the second stage:

$$M_W = \frac{g}{\sqrt{2}}(\kappa^2 + \kappa'^2)^{1/2},$$

where $\kappa$ and $\kappa'$ are related to the minimum of $\phi$. Since it is the $W$ that controls low-energy charged-current phenomenology, it is extremely difficult to learn anything about $v_R$, and hence about $M_{W'}$, from low-energy physics. One needs to look for departures from a purely left-handed interaction in weak processes, and such a departure has never been observed. The mass of the $W'$ is therefore hard to predict.

### *1.3.3 Coupling the $W'$ to Fermions*

Although there are many possibilities for the Higgs sector in a theory—left-right symmetric or otherwise—that contains a $W'$, the coupling of the $W'$ to fermions is more constrained. Lorentz-invariance and renormalizability restrict the $W'$–fermion–fermion coupling to be of the form

$$\frac{ig}{2\sqrt{2}}\bar{\psi}_i(a + b\gamma_5)\gamma_\mu W'^\mu \psi_j U_{ij},$$

where $a$ and $b$ are constants and $U_{ij}$ is a CKM matrix element connecting fermions $i$ and $j$. Gauge-invariance may further restrict the form of the coupling; for example, the $SU(2)_L$ invariance of the standard model leads to the $V - A$ character of the weak interaction, with $a = 1$, $b = -1$. For lack of a compelling alternative, we shall assume throughout this analysis that the right-handed CKM matrix is identical to the familiar left-handed one—that is, essentially diagonal. We do not consider the possibility of a fourth generation of quarks and leptons, which is severely constrained by present data.

From this form of the coupling, we may calculate the partial width of a $W'$ into a massless quark $i$ and an antiquark $j$:

$$\Gamma_{ij} = \frac{a^2 + b^2}{2} \frac{N_c G_F M_W^2 M_{W'}}{6\sqrt{2}\pi} |U_{ij}|^2,$$

where $N_c$ is the color factor of three. We define the parameter $\lambda^2$ as

$$\lambda^2 = \frac{a^2 + b^2}{2},$$

which is equal to one in, among other cases, the standard model. It is also equal to one in a left-right symmetric model in which the left- and right-handed gauge sectors couple to matter with equal strengths. We refer to the case $\lambda^2 = 1$ as *standard strength* couplings. The parameter $\lambda^2$ is less than one if the $W'$ couples to quarks with less than standard strength. The analysis presented in this thesis will allow us to place upper limits on $\lambda^2 B$, where $B$ is the branching ratio to leptons.

The partial width of the $W'$ to a charged lepton and neutrino is given by the above expression, except that there is no color factor and no CKM factor. We shall consider only those models in which, as in the standard model, there are no Cabibbo-like angles in the leptonic sector.

We note that the presence of a right-handed scale would invite several possibilities for neutrino masses. The neutrino could be a Dirac particle, with the left- and right-handed neutrinos degenerate in mass. Or, the neutrinos could be Majorana particles, and the masses of left- and right-handed neutrinos could differ substantially, with the $\nu_R$ possibly quite heavy. If the $W'$ couples to a massive neutrino, there are three possibilities:

1. The neutrino may be so heavy that the decay $W' \to l\nu$ is kinematically forbidden. In this case, the branching ratios to the channels that are the focus of this analysis are zero.

2. The neutrino may decay into observable particles within the volume of the detector. In this case, the missing energy that we rely upon as the signature

of a neutrino will not be present. However, the decay of the $W'$ will still be characterized by an electron or muon with high momentum.

3. The neutrino may be light and stable. In this case the experimental signature of the decay $W' \to l\nu$ is very much like that of the familiar process $W \to l\nu$.

It is the last case that is the focus of this analysis, as well as of other direct searches that have been carried out to date. We will discuss these searches in Section 1.5.

### *1.3.4 Production Properties of W' 's*

With the couplings given above, the dominant production mechanism for $W'$'s at a hadron collider is the Drell-Yan process, shown in Figure 1. This process is also responsible for the production of $W$ and $Z$ bosons. A quark $a$ and an antiquark $b$ from the two colliding hadrons annihilate to form a $W'$, which may be virtual or real. The $W'$ production cross section per unit rapidity is given in the parton model by

$$\frac{d\sigma}{dy} = \frac{4\pi^2 x_1 x_2}{3M_{W'}^3} \sum_{i,j} f_i^{(a)}(x_1) f_j^{(b)}(x_2) \Gamma_{ij}.$$

Here $f_i^{(a)}(x)$ is a structure function that represents the probability for finding a quark of type $i$ in hadron $a$, carrying a momentum fraction between $x$ and $x + dx$, and $\Gamma_{ij}$ is the partial width of the $W'$ into the quark-antiquark pair $i, j$. The rapidity $y$ of the $W'$ is related to the momentum fractions $x_1$ and $x_2$ by

$$x_1, x_2 = \frac{M_{W'}}{\sqrt{s}} e^{\pm y},$$

where $\sqrt{s}$ is the center-of-mass energy of the colliding hadrons.

The $W'$ production cross section as a function of $M_{W'}$ is shown in Figure 2, assuming standard-strength couplings. These cross sections were calculated using the structure functions of Harriman, Martin, Roberts, and Stirling, set B[16], which is the default structure function set for this analysis and will henceforth be referred

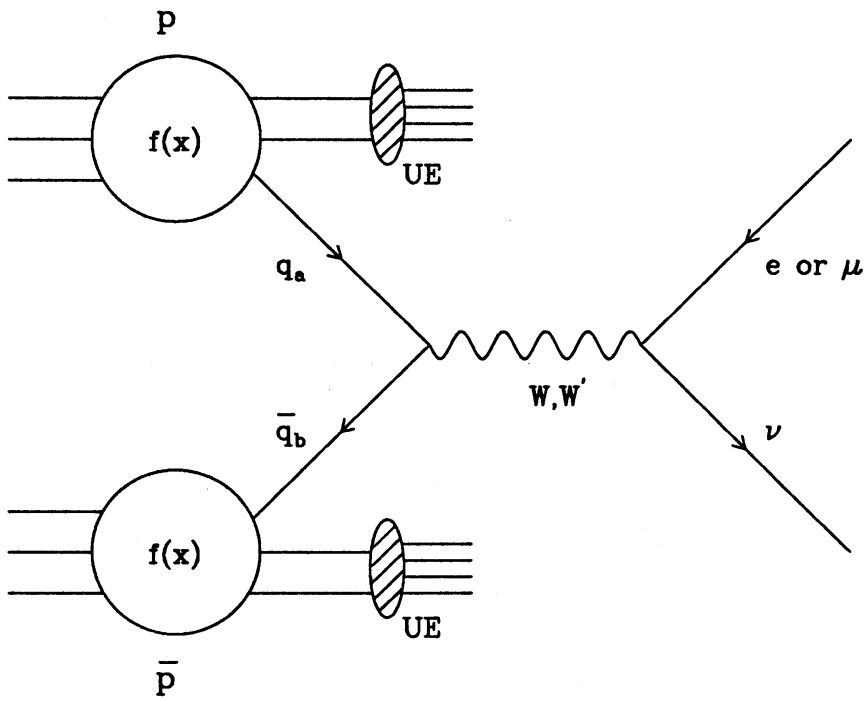


Figure 1. The Drell-Yan process of quark-antiquark annihilation. A quark and an antiquark from the incident hadrons undergo hard scattering and produce a $W$ or $W'$, shown here undergoing leptonic decay. The remnants of the incident hadrons fragment to form the underlying event (UE).

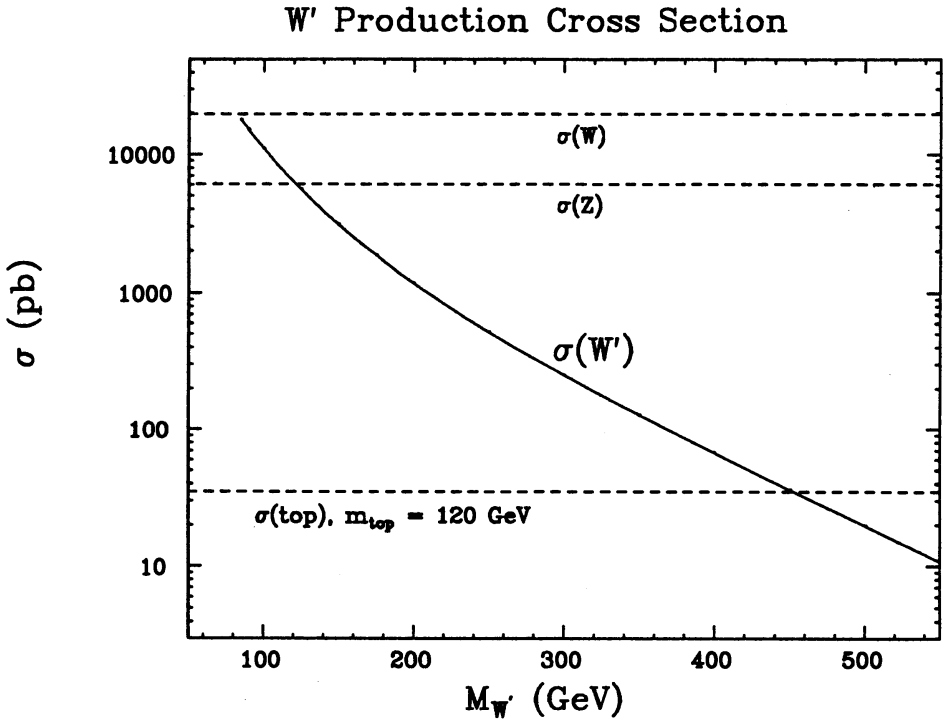


Figure 2. The $W'$ production cross section as a function of mass, in $\bar{p}p$ collisions at $\sqrt{s} = 1.8$ TeV, for standard-strength couplings. Also shown are the production cross sections for standard-model $W$, $Z$, and top quark production.

to as HMRS(B). The calculation was performed using the Monte Carlo program described in Chapter 7. Also shown in Figure 2, for comparison, are some standard model benchmarks: the $W$ and $Z$ production cross sections, and the top quark production cross section for $m_{top} = 120$ GeV.

### *1.3.5 Leptonic Branching Ratios*

The main result of this thesis is a limit on the production cross section times leptonic branching ratio for $W'$'s. The leptonic branching ratio is therefore not an input to this measurement. We are, however, interested in establishing the nominal leptonic branching ratio for two reasons. First, the fact that it is sizable indicates that this search channel is a profitable one. Second, it will allow us to convert our

limit on the cross section times branching ratio into a limit on the $W'$ mass itself. This will be discussed further in Chapter 8.

To convert the partial widths given above into branching ratios, it is necessary to know how many of these channels are actually available. The $W'$, even if it is scarcely more massive than the $W$ boson, is sufficiently heavy that all leptons and quarks, with the exception of the top quark, may be considered massless. The top quark, however, is known to be quite heavy, and it is possible that for certain values of the top quark and $W'$ masses the phase space available for the decay $W' \rightarrow t\bar{b}$ may be reduced or even eliminated, resulting in a correspondingly higher branching ratio to the light quarks and leptons. CDF has established a lower limit on the top quark mass of 91 GeV[17], and general theoretical arguments[18] constrain the top mass to be less than approximately 200 GeV.

For decays to a heavy fermion such as top, the expression for the partial width is multiplied by a phase space factor[19]

$$f(x) = (1-x)(1-\frac{1}{2}x-\frac{1}{2}x^2)$$

where $x = m_{top}^2/M_{W'}^2$. As we shall see, this analysis is sensitive to $W'$'s with masses in excess of 400–500 GeV. On these mass scales, the top quark, even if it is as massive as theory allows, may still be considered a light fermion, since the variable $x$ is much less than one. In this limit, where the top quark mass is negligible, we expect the branching ratio of the $W'$ to each leptonic channel to be 1/12. If the top quark channel is completely closed, the leptonic branching ratio is 1/9. In obtaining these numbers, we have assumed that the $W'$ does not have a significant branching ratio to either exotic final states or to pairs of ordinary gauge bosons. Typically the latter process is suppressed by a mixing angle of order $(M_W/M_{W'})^4$, as well as by phase space factors, so its contribution to the total $W'$ width is in general quite small.

We have therefore taken the total width of the $W'$ to be

$$(2.76 \text{ GeV})\frac{M_{W'}}{M_W}.$$

Here 2.76 GeV is the lowest-order width of the $W$ with 12 decay channels open. That the width should grow linearly is evident from dimensional analysis—with all fermions considered light, $M_{W'}$ is the only scale in the problem. Our analysis, however, is insensitive to the precise form of the intrinsic width of the $W'$, which is washed out by detector resolution effects.

## 1.4 Some Important Variables

The $W'$ search described in this thesis is based on an analysis of $\bar{p}$-$p$ collision data collected by the Collider Detector at Fermilab (CDF). We now introduce some important variables used in the description of hadron collisions. The so-called "transverse variables" $E_T$, $P_T$, $\not{E}_T$, and $M_T$ will be referred to constantly throughout the text.

The coordinate system we will use is defined with the $z$-axis pointing along the proton beam direction, the polar angle $\theta$ measured with respect to the $z$-axis, and the azimuthal angle $\phi$ starting from a horizontal line normal to the colliding beams. This coordinate system is shown in Figure 3. Frequently, the pseudorapidity

$$\eta = -\ln\tan(\theta/2)$$

is used rather than the polar angle. This quantity has the property that it transforms additively under a Lorentz boost along the $z$-axis, so that differences in pseudorapidity, and in particular the quantity $d\eta$, are Lorentz invariant.[1] This fact is useful since the collisions observed at CDF are between constituent partons whose center of mass varies on an event-by-event basis.

[1] Strictly speaking, this property holds true only in the limit where a particle's mass is small compared to its energy, as is the case for most particles observed at CDF.

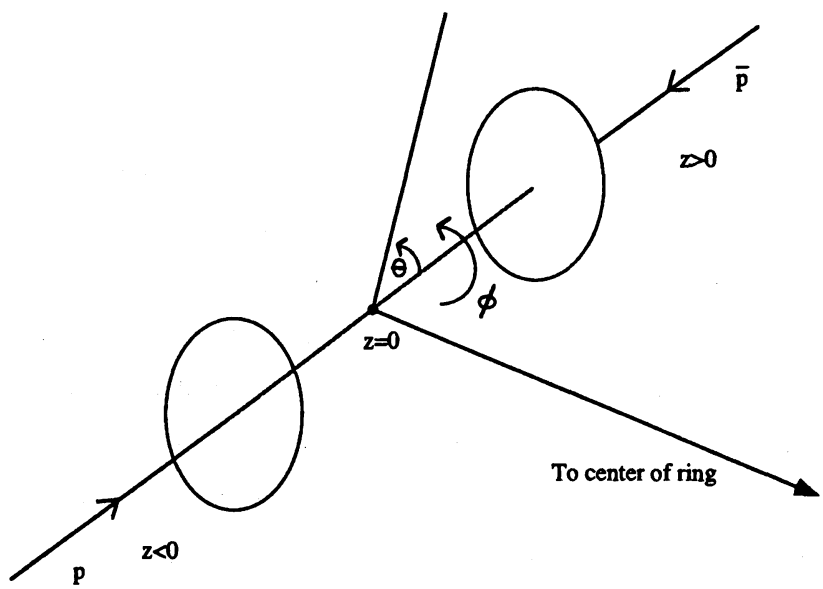


Figure 3. Polar coordinate system used in the description of hadron collisions.

In addition, one often uses the so-called transverse energy $E_T$ in place of the scalar energy $E$, and the transverse momentum $P_T$ in place of the scalar momentum $P$. (In CDF jargon, energy always refers to a measurement made in the calorimeters, and momentum to a measurement in the tracking chamber.) These quantities are defined as

$$E_T = E \sin\theta$$

and

$$P_T = P \sin\theta$$

These quantities can be thought of as the "projection" of the energy and momentum onto the plane transverse to the beam direction. For example, if an electron deposits 50 GeV of energy into a calorimeter tower located at 60° from the beam axis, we say that the electron has an $E_T$ of 50 GeV $\times \sin 60° = 43.3$ GeV. The phase space element $E_T dE_T\, d\eta\, d\phi$ is Lorentz invariant (again in the limit of massless particles), and is the "natural" choice for describing hadron collisions. Rare and interesting processes, such as electroweak boson and top quark production, are characterized by particles with high transverse momenta, and are sometimes referred to as "high-$P_T$" physics, in contrast to the low-$P_T$ phenomena that make up the great majority of garden-variety $\bar{p}$-$p$ collisions.

One also defines the transverse energy vector $\boldsymbol{E}_T$ as

$$\boldsymbol{E}_T = \sum_i E_{T_i} \hat{\mathbf{n}}_i,$$

where the sum is over all cells of the calorimeter[2] and the $\hat{\mathbf{n}}_i$ are two-dimensional unit vectors pointing from the event vertex to the cell centers. It may seem odd to define energy as a vector, but in fact this quantity is a good approximation to the vector sum of the transverse momenta of all the particles produced in an event. (The latter quantity cannot be directly measured with high precision because tracking

[2] In CDF analyses, the sum is over all cells with $|\eta| < 3.6$. To be included in the sum, individual cell energies (not transverse energies) must exceed detector-dependent thresholds of order several hundred MeV. See Chapter 3 for a discussion of the CDF detector.

chambers typically cover a smaller angular region than calorimeters do, and are not sensitive to neutral particles.) Because the transverse momentum of the proton-antiproton system was zero before the collision, one expects the magnitude of $\boldsymbol{E}_T$ to be zero (to within the resolution of the detector). There are two cases where this is not true. Muons act as minimum-ionizing particles, so that even a very energetic muon will deposit only a few GeV of energy in a typical calorimeter. If a muon has been well-identified by other means, the $\boldsymbol{E}_T$ can be easily corrected to reflect the "true" energy of the muon. The other, more interesting case, is when the event contains an energetic neutrino (or possibly some other stable, noninteracting, as yet undiscovered particle). In this case, one speaks of an imbalance in the transverse energy, and defines the missing-$E_T$ vector

$$\not{\boldsymbol{E}}_T = -\boldsymbol{E}_T.$$

This quantity defines the transverse momentum of the neutrino. The magnitude of the $\not{\boldsymbol{E}}_T$ is used even more often and is usually referred to simply as the missing-$E_T$, or $\not{E}_T$.

The remaining transverse variable, the transverse mass $M_T$, is related to those described above, and is of central importance in this analysis. Suppose that one observes two particles $a$ and $b$, assumed to come from a two-body decay. What is the mass $M$ of the parent particle? Of course, it is just

$$\begin{aligned} M &= \sqrt{(p_a + p_b)^2} \\ &\simeq \sqrt{2(E_a E_b - \mathbf{p_a} \cdot \mathbf{p_b})} \\ &\simeq \sqrt{2E_a E_b(1 - \cos\Delta\phi^{a\text{-}b})}, \end{aligned}$$

where $\Delta\phi^{a\text{-}b}$ is the angle between the 3-vectors $\mathbf{p_a}$ and $\mathbf{p_b}$. When we contemplate using this definition to measure the $W$ boson mass from the process $W \to e\nu$, however, we realize its limitations in the real-world environment of a hadron collider. Because the neutrino in this process is unobserved, its momentum vector $\mathbf{p}_\nu$ must be inferred from a sum of energy deposited everywhere in the detector, as described

above. But a complete knowledge of $\mathbf{p}_\nu$ would require a knowledge not only of the transverse components of this energy, but also of the $z$-components. Because most of the 1.8 TeV of energy in the collisions we are considering flows down the beampipe at very small angles, it is impossible to measure $p_{\nu,z}$ accurately. However, because $\sin\theta$ is so small for this energy, it makes a very small contribution to the *transverse* energy. We therefore define the transverse mass, $M_T$ to be

$$\begin{aligned} M_T &= \sqrt{2(E_T^e E_T^\nu - \boldsymbol{P}_T^e \cdot \boldsymbol{P}_T^\nu)} \\ &\simeq \sqrt{2E_T^e \not{E}_T(1 - \cos\Delta\phi^{e\text{-}\nu})} \end{aligned}$$

where $\Delta\phi^{e\text{-}\nu}$ is now the angle between the 2-vectors $\boldsymbol{P}_T^e$ and $\not{\boldsymbol{E}}_T$. The transverse mass is the analog, in the transverse momentum subspace, of the invariant product of 4-vectors that gives the mass. It is manifestly invariant under boosts along the $z$-axis. One can also show that it is invariant with respect to transverse boosts of the $W$, to first order in the transverse velocity $\beta$ of the $W$[20]. The transverse mass distribution for the process $W \to e\nu$ is shown in Figure 4. It is the sharply falling upper edge of this distribution that gives information about the mass of the particle. This process has been used as an example, but of course this discussion also applies to the process $W \to \mu\nu$, or to $W'$ decays.

## 1.5 Previous Limits

Direct searches for $W'$'s have been carried out at the CERN $\bar{p}p$ collider by the UA1 and UA2 collaborations[21, 22]. The UA2 analysis was based on a sample of 251 $W \to e\nu$ candidate events with electron transverse momentum ($P_T$) greater than 20 GeV and with an electron-neutrino transverse mass greater than 50 GeV. They then performed a likelihood fit of the observed electron $P_T$ distribution to Monte Carlo predictions for $W$ and $W'$. The data were consistent with $W$ production and decay, and led to a limit of $M_{W'} > 209$ GeV at the 90% confidence level, assuming standard couplings. The UA1 limit was obtained using a sample of 149 events with

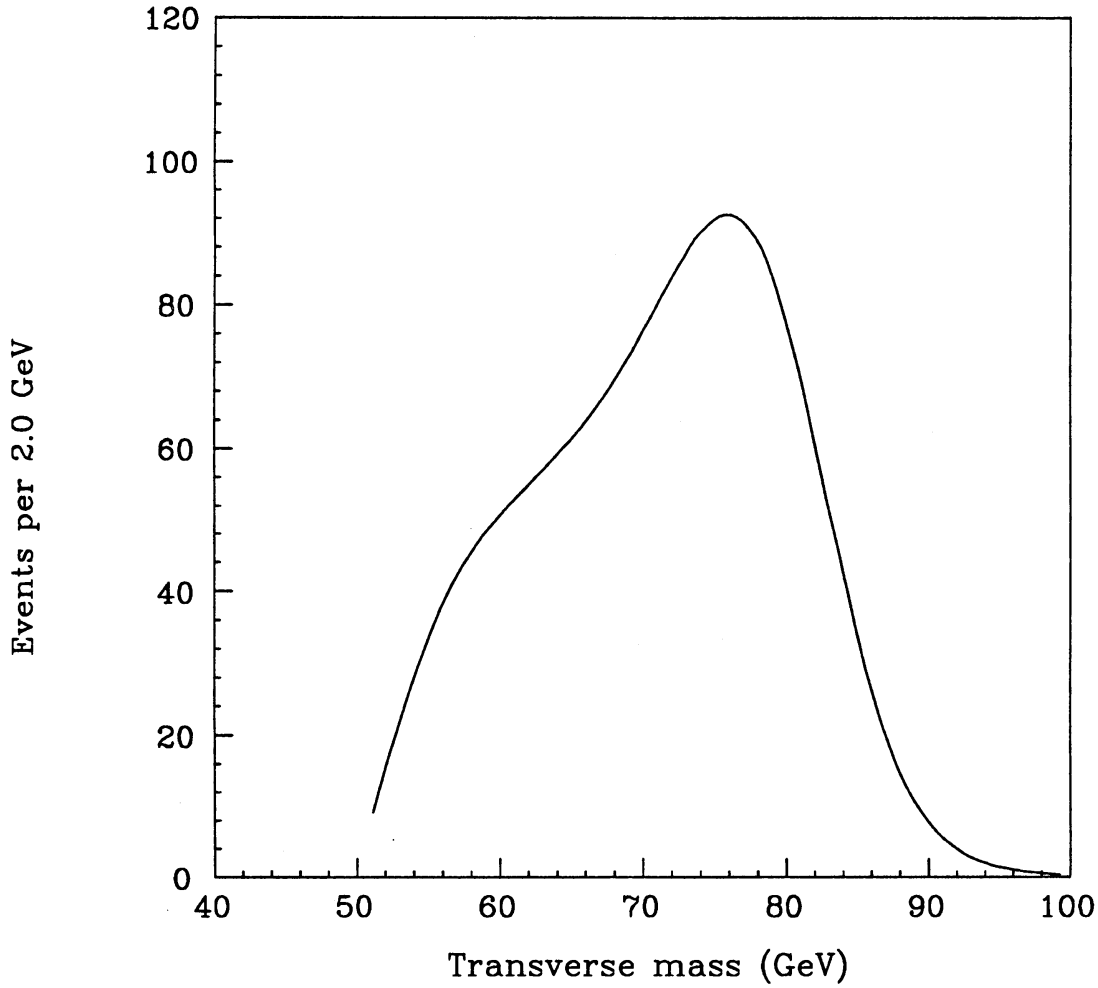


Figure 4. Transverse mass distribution for the process $W \rightarrow e\nu$.

electron transverse energy $E_T$ greater than 30 GeV and with missing-$E_T$ greater than 30 GeV. Based on the lack of observed events with a transverse mass above that expected from the process $W \rightarrow e\nu$, they established a limit of $M_{W'} > 220$ GeV at the 90% confidence level, again assuming standard couplings. No previous direct searches have been reported in the muon channel. The UA1 and UA2 upper limits in the electron channel are substantially weaker than the results reported in this thesis.

In addition to these direct searches, indirect limits on right-handed $W$'s have been inferred from the absence of a $V+A$ component in the decay of highly polarized muons. Precise measurements at TRIUMF of the endpoint of the $e^+$ spectrum in polarized $\mu^+$ decay lead to a limit[23] of 423 GeV at the 90% confidence level, assuming that the right-handed neutrino is massless. For massive right-handed neutrinos, a limit is obtained from the parity-violating decay asymmetry parameter $\delta$ in muon decay[24]. The 90% confidence-level limit is shown in Figure 5. These are very precise and beautiful experiments, but for right-handed neutrino masses greater than about 40 MeV the limits are lower than those obtained by the direct searches at CERN. Recently, an experiment at KEK[25] has obtained a $W_R$ limit from an analysis of the positron asymmetry in the decay chain $K^+ \rightarrow \mu^+\nu$ followed by $\mu^+ \rightarrow e^+\nu\bar{\nu}$. The limit depends on the magnitude of the right-handed Cabibbo angle, varying from 303 GeV for $|\sin\theta_{c,R}| = 0$, to 653 GeV for $|\sin\theta_{c,R}| = 1$. These limits are at the 90% confidence level. Again, a light right-handed neutrino is required.

Finally, theorists have attempted to set very high limits on the $W'$ mass based on the observed $K_L$–$K_S$ mass difference. The mixing of the strong interaction eigenstates $K^0$ and $\bar{K}^0$ into $K_L$ and $K_S$ is dominated by the box diagram shown in Figure 6. Any new charged bosons that couple to quarks will give additional contributions to this process. In the case of the canonical left-right symmetric model, such contributions would come from both the $W'$ and from charged Higgs

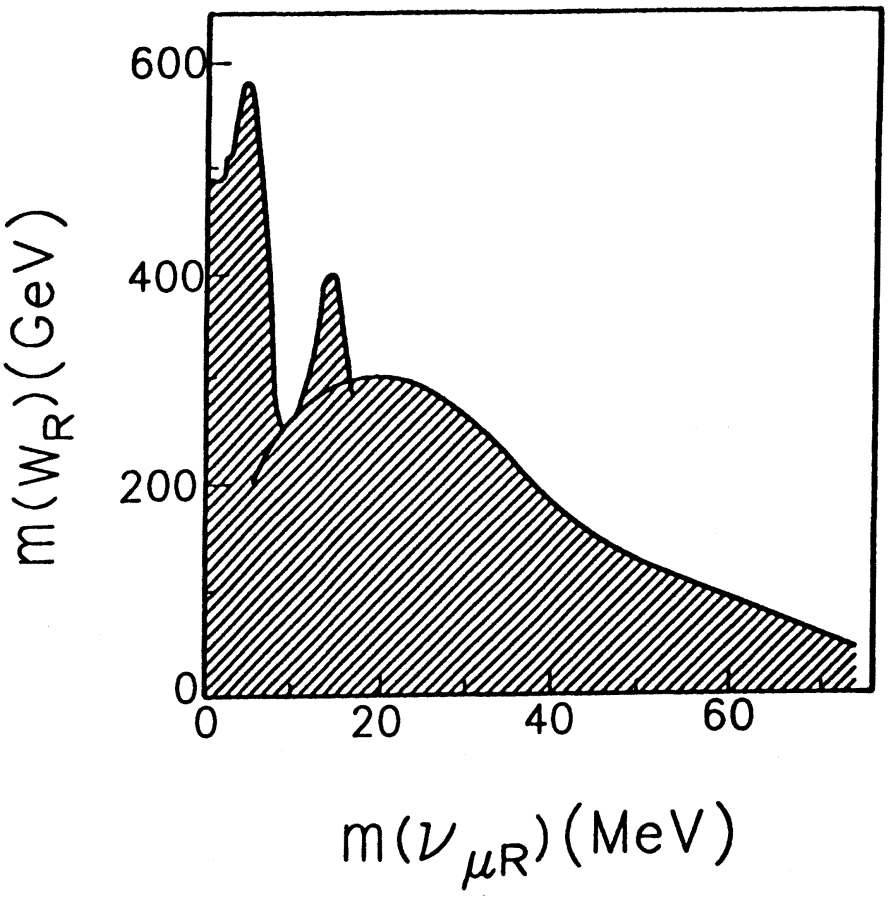


Figure 5. $W_R$ mass limits (from ref. [24]). 90% C.L. limits on the mass of a $W_R$ vs. the right-handed muon neutrino mass $M(\nu_{\mu R})$ in left-right-symmetric extensions of the standard model of weak interactions. The area below the curves is excluded.

scalars. The magnitude of these contributions is model-dependent (in particular, it depends on the size of off-diagonal elements of the right-handed CKM matrix), and the evaluation of their effect on the mass difference is further complicated by the nonperturbative aspects of long-distance hadronic physics (one must evaluate the matrix element of a 4-quark operator between two hadronic states). Nonetheless, by means of these kinds of arguments limits of 1-2 TeV have been suggested[26].

## 1.6 Outline of this Paper

This paper describes a search[27] for heavy $W$ bosons, denoted generically by $W'$, through the process $\bar{p}p \rightarrow W'$ followed by either $W' \rightarrow e\nu$ or $W' \rightarrow \mu\nu$. (Reference [27], an article in *Physical Review Letters* that summarizes this analysis, is reproduced in Appendix B.) The data for this measurement were collected by the Collider Detector at Fermilab (CDF) during the 1988–89 Tevatron collider run. The CDF detector is particularly well suited for the identification of high-momentum electrons and muons, objects characteristic of $W$ or $W'$ events. In addition, its nearly complete angular coverage permits high-quality measurements of the magnitude and direction of the energy from other particles in the event, which in turn enables one to reconstruct the transverse momentum of the neutrino. By forming the transverse mass of the $e$-$\nu$ or $\mu$-$\nu$ combination, we can search for the peak that would indicate a $W'$.

The basic equation that drives this analysis is

$$\sigma \cdot B(W' \rightarrow l\nu) = \frac{N_{W'}}{\mathcal{L}A\epsilon},$$

where the measured cross section times leptonic branching ratio, $\sigma \cdot B$, is given in terms of the observed number of $W'$ events $N_{W'}$, the integrated luminosity $\mathcal{L}$, the kinematic acceptance $A$, and the lepton identification efficiency $\epsilon$. Of course, these numbers all have uncertainties that are reflected in the final result. In the case of no observed $W'$ events, $N_{W'}$ is replaced by the appropriate upper limit.

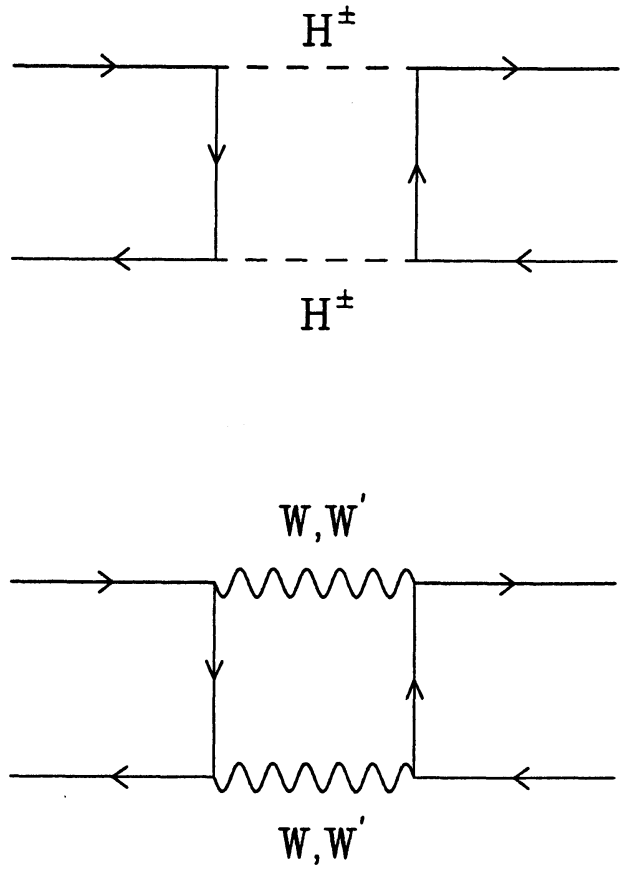


Figure 6. Two of the box diagrams responsible for the $K_L$–$K_S$ mass difference. In the standard model, only the $W$ contributes to the loop. In extended models, the $W'$ and charged Higgs may also contribute.

Chapter 2 gives an overview of the Fermilab Tevatron collider, and describes the techniques that allow the world's highest-energy proton and antiproton beams to be delivered to CDF. In Chapter 3 we describe the CDF detector itself, with an emphasis on the components used in electron and muon identification. In Chapter 4 we discuss the hardware and software triggers used to select electron and muon candidates in real time amid the very busy environment of a hadron collider. In Chapter 5 we describe the selection of the events used in this analysis, and in Chapter 6 we evaluate the efficiencies of the cuts used in this selection. Chapter 7 gives a discussion of the Monte Carlo used to generate and simulate $W'$ and $W$ events. Finally, in Chapter 8 we fit the data to a superposition of $W'$ and $W$ Monte Carlo transverse mass distributions, fold in the systematic uncertainties, and extract a limit on the cross section times branching ratio for $W'$ production and decay. We conclude with some remarks on the interpretation of these results.

# CHAPTER 2

# THE TEVATRON

The CDF detector is situated at the B0 collision point of the Fermilab Tevatron collider. The Tevatron, located on the grounds of the Fermi National Accelerator Laboratory some forty miles west of Chicago, provides the world's highest-energy proton-antiproton collisions. Without the many remarkable technical triumphs of this machine and the dedicated staff that has achieved them, physics with CDF would not be possible. This chapter provides an overview of colliding beam operations at Fermilab. For additional details, see ref. [28] and the references cited therein.

## 2.1 Luminosity

The physics addressed by this thesis, along with much of the electroweak and heavy-flavor physics of interest to CDF, has an extremely small cross section—of order a few hundred picobarns or less. (For comparison, the visible inelastic $p$-$\bar{p}$ cross section at Tevatron energies is approximately 46.8 mb.) To make such rare processes accessible, high-intensity colliding beams are a necessity. The intensity of the beams is characterized by a single number, the instantaneous luminosity $\mathcal{L}$, which has units of $\mathrm{cm}^{-2}\mathrm{s}^{-1}$. The performance of the accelerator over time is characterized by the

integrated luminosity, $\int \mathcal{L}\, dt$. (The integrated luminosity is often written also as $\mathcal{L}$; the distinction between this and the instantaneous luminosity is usually clear from the context.) Integrated luminosity has units of $\mathrm{cm}^{-2}$, which is the inverse of the dimensions of a cross section. So it is convenient to define the odd-sounding unit "inverse picobarn" to be

$$1\ \mathrm{pb}^{-1} = 10^{36}\ \mathrm{cm}^{-2}.$$

When $\mathcal{L}$ is expressed in inverse pb, the number of events $N$ that one expects to produce of a given type is $N = \mathcal{L}\sigma$, where $\sigma$ is the cross section in picobarns for the process.

At Fermilab, six bunches of protons and six bunches of antiprotons circulate at a revolution frequency of 47.7 KHz. Hence the time between bunch crossings in the CDF detector is 3.5 $\mu$sec. The instantaneous luminosity is given by

$$\mathcal{L} = \frac{N_p N_{\bar{p}} B f_0}{4\pi\sigma^2},$$

where $N_p$ ($N_{\bar{p}}$) is the number of protons (antiprotons) per bunch, $B$ is the number of bunches of each type, $f_0$ is the revolution frequency, and $\sigma$ is the transverse cross-sectional size of the bunches. During the 1988–89 run in which the data for this thesis were collected, $N_p$ was typically $7 \times 10^{10}$, and $N_{\bar{p}}$ was approximately $3 \times 10^{10}$. The cross sectional size of the bunches, $\sigma$, is determined by the phase-space properties of the beams and by the magnetic focusing properties of the accelerator. The area of the beams is not constant as they circulate in the ring; rather, the beams are squeezed by "low-beta" quadrupole magnets located near the CDF interaction region so that maximum luminosity is achieved in the center of the CDF detector. Strictly speaking, the quadrupoles perform a phase space rotation of the beam that decreases the bunch's transverse size while increasing its transverse momentum distribution. Outside of the collision region, one prefers the opposite: a larger-sized beam (to reduce destabilizing interactions of the beam with itself through long-range Coulomb forces) with a narrow transverse momentum distribution (to reduce

losses). During 1988–89 operation, the effective radius of the colliding beams in CDF was approximately 60 microns.

## 2.2 Antiproton Collection

The collection, storage, and injection of large numbers of antiprotons were made possible by a series of technical breakthroughs at the CERN $S\bar{p}pS$ collider in the late 1970's and early 1980's[29]. The central problem is to trap antiprotons, produced with a wide range of energies and angles, and convert them into a collimated bunch with nearly constant momentum, in numbers large enough to yield useful luminosity. Because this process involves a significant decrease in the entropy of the antiproton ensemble, it is frequently referred to as "cooling." The collection of antiprotons begins with fixed-target proton-nucleon collisions, so we consider proton acceleration first.

A sketch of the Fermilab accelerator complex is shown in Figure 7. Protons are stripped from a hydrogen source in a Cockroft-Walton preaccelerator, and are accelerated to 200 MeV in the Linac. Next they are transferred to the Booster ring and accelerated to 8 GeV. The protons are then injected into the Main Ring, and are accelerated to 120 GeV. From there they are extracted and strike a tungsten target, producing antiprotons in the reaction $pN \rightarrow \bar{p} + X$. Because the antiproton is the only stable, heavy, negatively-charged particle, it is a relatively simple matter to select magnetically those with momentum near 8 GeV.

These antiprotons pass through a lithium lens, where they are collimated, and enter the Debuncher ring. Antiprotons enter the Debuncher in bunches approximately 30 cm long, separated by roughly 5.4 m. The Debuncher lengthens each bunch in the $z$-direction (the direction of the beam) while narrowing its longitudinal momentum distribution. The Debuncher thus performs a longitudinal phase-space rotation similar to that performed in the transverse direction by the Tevatron's low-

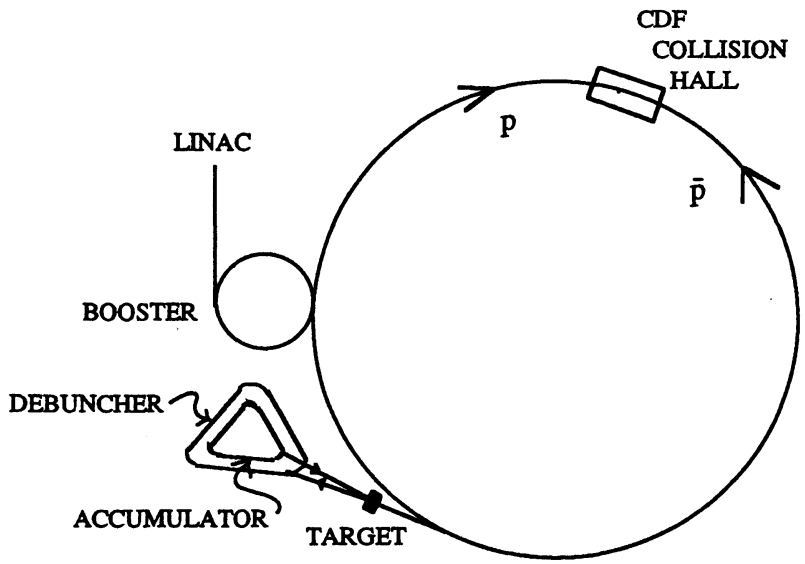


Figure 7. The Fermilab accelerator complex.

beta quadrupoles. The effect is to reduce the beam's momentum spread from 3.5% to 0.2%.

The beam is next transferred to the Antiproton Accumulator, where over a period of up to 24 hours it is stored and "cooled" in all three momentum-space directions so that the stack of antiprotons can eventually be injected into the Main Ring. The antiprotons are cooled using the technique of Stochastic Cooling, which was first developed in the early 1970's to cool proton beams at CERN's ISR[30] and subsequently applied to antiproton beams at the S$\bar{p}$pS in the 1980's. The Stochastic Cooling system is shown schematically in Figure 8. As antiprotons circulate in the Accumulator ring, pickups detect the position of antiprotons that are not in the central orbit of the ring. The signal is amplified and sent across the ring to the kickers, where it arrives before the antiprotons in question do. The kickers apply an electric field that brings the errant antiprotons back into the central orbit. In

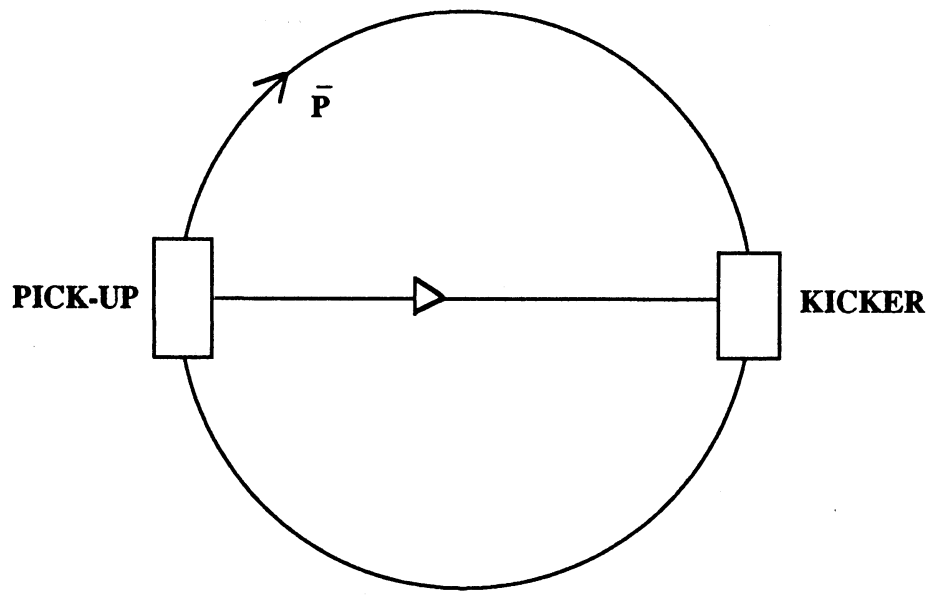


Figure 8. Highly schematic view of the Stochastic Cooling system.

the process, however, the field also perturbs other particles, resulting in the introduction of noise. The process therefore proceeds slowly. The energy distribution of antiprotons in the Accumulator is shown in Figure 9. After several hours, the width of the stack is only a few MeV.

Typical stack sizes are of order $3.5 \times 10^{11}$ antiprotons. For stack sizes larger than about $6 \times 10^{11}$, intrabeam scattering raises the beam's emittance (a quantity related to its transverse size) to the point where it exceeds the admittance of the Main Ring aperture. As it is, the efficiency for delivering antiprotons from the Accumulator to the Main Ring is approximately 40%[31].

During the 1988–89 run, an antiproton production rate of $2 \times 10^{10}$/hour was achieved. This rate is driven by two factors. The first is the Main Ring cycle time of 2.5 seconds, which determines the frequency at which proton pulses can be delivered to the target. The second is the density of protons in the Main Ring,

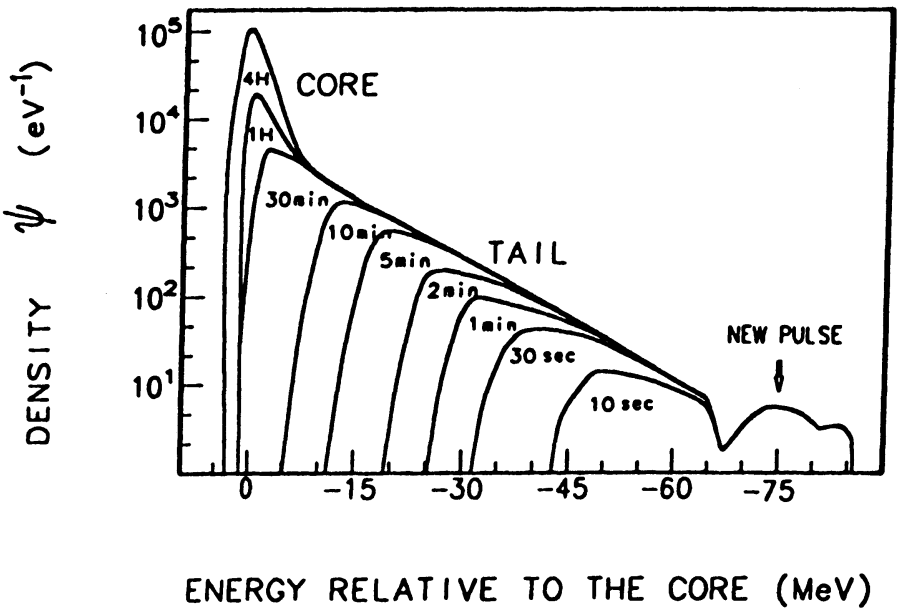


Figure 9. Energy distribution of antiprotons in the Accumulator ring as a function of time, showing the effect of stochastic cooling.

which in turn is limited by space-charge effects at injection into the Booster. In the future, the Lab plans to address these two bottlenecks with a series of upgrades. The Main Injector, scheduled for construction in the mid-1990's, will have a cycle time of 1.5 seconds. And the Linac upgrade planned for 1993 will raise the energy at injection into the Booster from 200 MeV to 400 MeV, thus reducing the magnitude of space-charge effects.

## 2.3 Collider Operation

When the antiproton stack is sufficiently large and sufficiently cold, the process of injection into the Tevatron collider begins. The Tevatron is a superconducting ring located directly below the Main Ring. First, six bunches of protons are injected at an energy of 150 GeV. Then, antiprotons are transferred from the Accumulator to the Main Ring, which is ramped to 150 GeV. They are injected (with approximately 60–

70% efficiency) into the Tevatron, where the counter-rotating beams of protons and antiprotons are accelerated to 900 GeV. When the Tevatron has reached "flattop", the current in the low-beta quadrupole magnets is raised to the full level to achieve maximum luminosity. Finally, the beams are scraped to reduce the number of outlying particles that form a "halo" around the center of the beam. At this point, data collection can begin.

# CHAPTER 3

# THE CDF DETECTOR

The CDF detector is a 5000 ton device designed to study a wide range of physics in $\bar{p}$-$p$ collisions. Conceived in the late 1970's and built in the early- and mid-1980's, the detector consists of a magnetic spectrometer to measure the momenta of charged particles, fine-grained electromagnetic and hadronic calorimeters to measure particle energies, and drift chambers for muon identification. At the time this analysis was performed, the CDF collaboration consisted of 257 physicists from 23 institutions in the United States, Italy, and Japan; a full list is given in Appendix B. The CDF detector is forward-backward symmetric; a side view of one half of the detector is shown in Figure 10, and an perspective view of the whole detector is shown in Figure 11. The detector has been described in a series of detailed papers[32]. In this chapter we discuss the components most relevant to this analysis, namely the tracking chambers, the central calorimeter, the central muon system, and the luminosity monitors.

## 3.1 Tracking Chambers

CDF uses two complementary tracking chambers. The inner tracking chamber, known as the Vertex Time Projection Chamber or VTPC[33], is the first detector

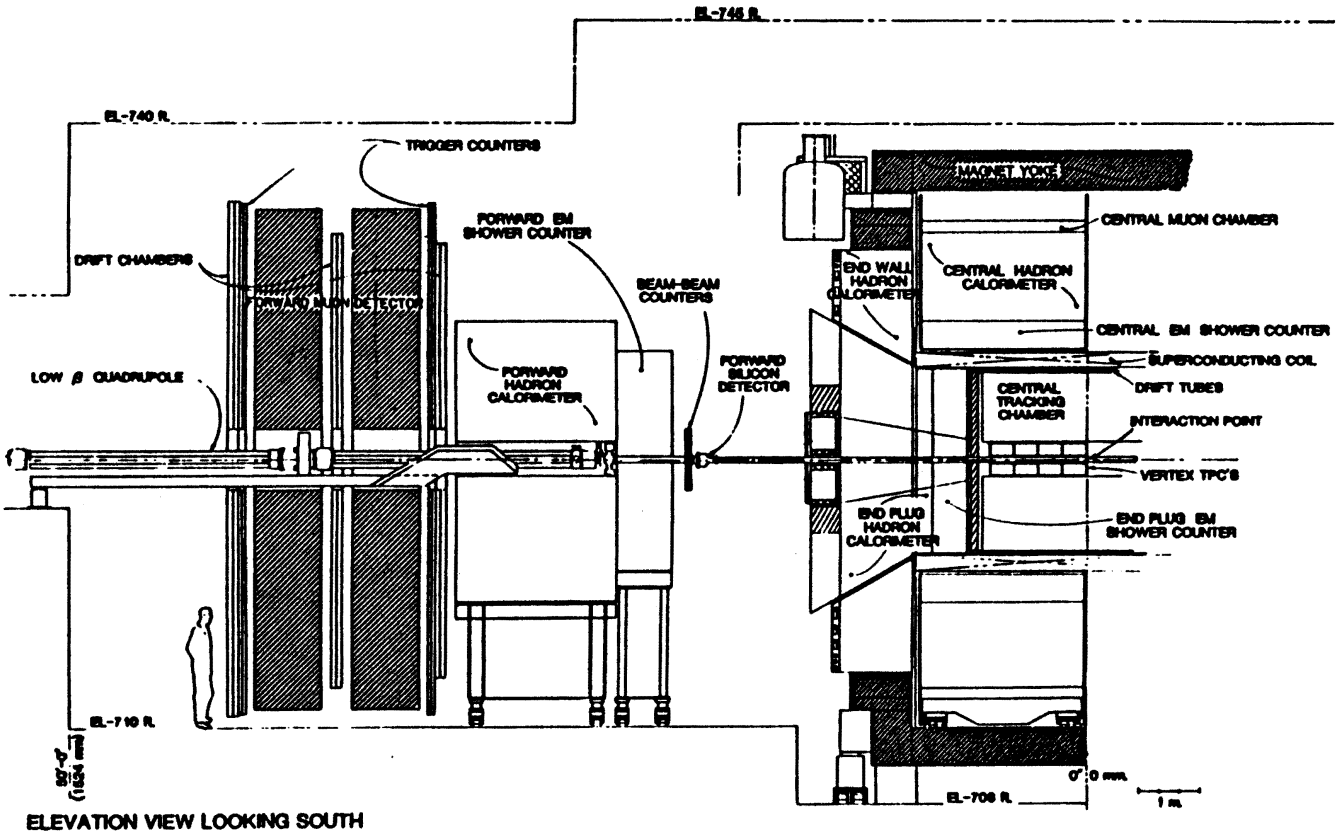


Figure 10. Cutaway view of one half of the CDF detector.

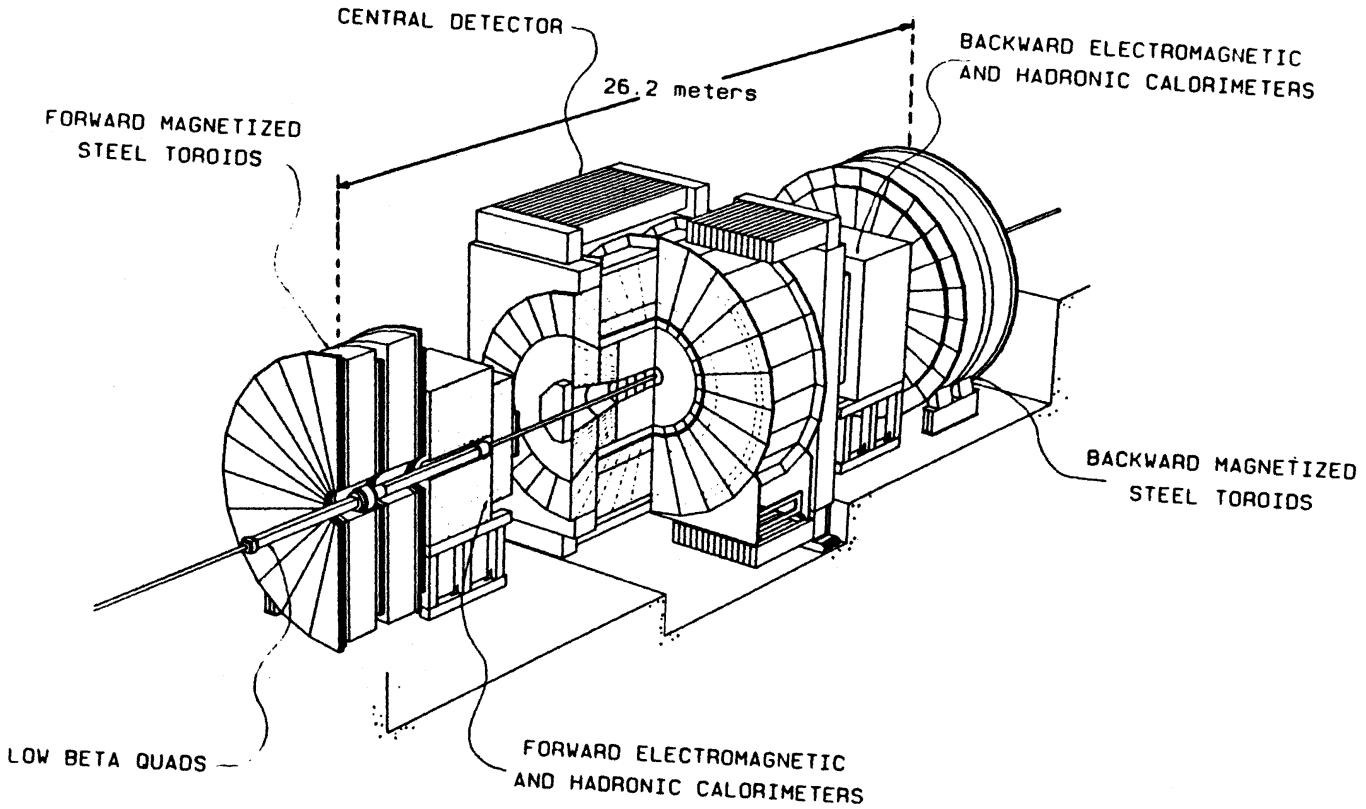


Figure 11. Perspective view of the CDF detector.

encountered by particles after they pass through the beam pipe. It consists of eight octagonal drift chamber modules that measure charged particle positions over the angular range $8° < \theta < 172°$. The VTPC does not measure momentum, but allows the event vertex to be located in $z$ to within 1 mm. (Because of the length of the proton and antiproton bunches, the $z$-vertex varies from event to event; the distribution is a gaussian with a width of about 30 cm.)

Outside the VTPC, at larger radii from the beam, the Central Tracking Chamber (CTC)[34] provides for precise momentum determination. The CTC is a cylindrical drift chamber, 1.3 m in radius and 3.2 m in length, immersed in a 1.412 Tesla solenoidal magnetic field. The CTC consists of 84 layers of sense wires organized into nine superlayers, as shown in Figure 12. Five of these are axial superlayers, each containing 12 layers of wires running parallel to the beam. The axial superlayers are interleaved with 4 stereo superlayers, which consist of six sense wire layers in which the angle with respect to the beam alternates between $\pm 3°$. The combination of axial and stereo layers permits accurate 3-dimensional track reconstruction. The superlayers are tilted at 45° with respect to the radial direction to account for the Lorentz angle of the electron drift in the magnetic field. The maximum drift distance in the argon-ethane-alcohol medium is less than 40 mm, corresponding to roughly 800 ns of drift-time.

The CTC has a momentum resolution of $\delta P_T/P_T = 0.002 \times P_T$ for isolated tracks that pass through all nine superlayers. When one constrains the track to pass through the measured event vertex, a process known as beam-constraint, the resolution improves to $\delta P_T/P_T = 0.0011 \times P_T$. The device was calibrated and aligned using a precision magnetic survey, cosmic ray data, and energy/momentum distributions for positively- and negatively-charged tracks[35].

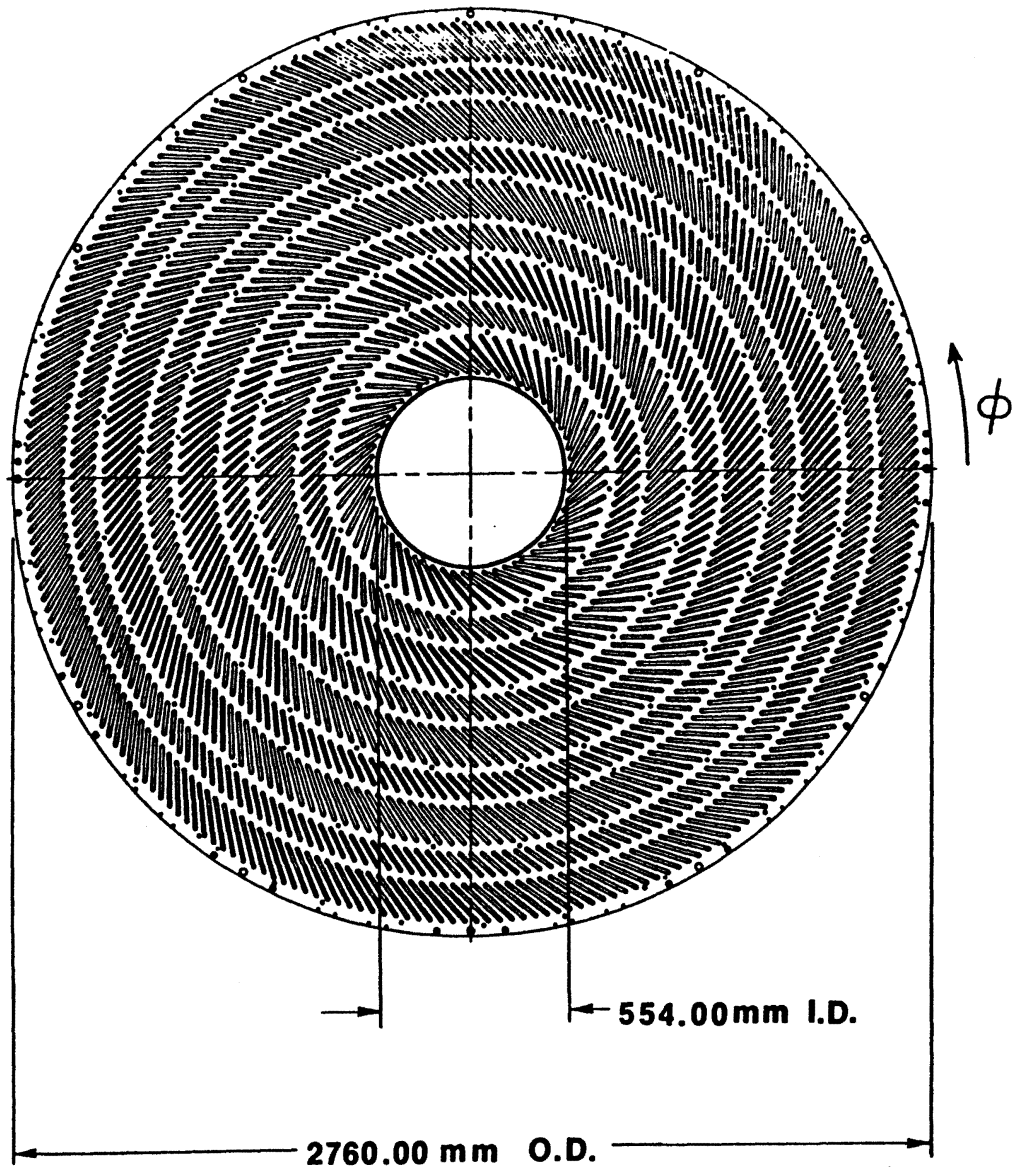


Figure 12. End view of the Central Tracking Chamber (CTC), showing the structure of the nine superlayers.

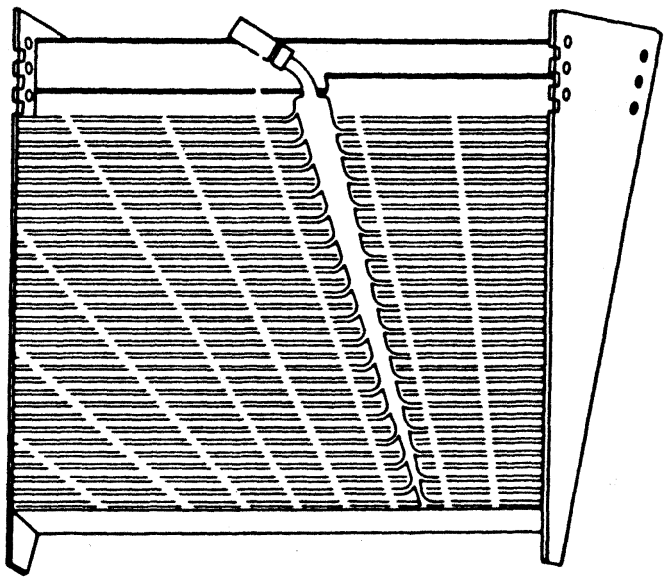

Figure 13. A central calorimeter wedge.

## 3.2 Calorimeters

The $W' \rightarrow e\nu$ search makes extensive use of the central electromagnetic calorimeter[36]. This device covers the region $|\eta| < 1.1$, and is segmented into towers of size 0.1 in $\eta$ by 15° degrees in $\phi$ that point back to the nominal interaction point $z = 0$. The towers are organized into 48 wedges; a schematic view of a wedge is shown in Figure 13. Each tower consists of between 21 and 31 layers of 5 mm thick SCSN-38 polystyrene scintillator interleaved with 6 mm thick sheets of aluminum-clad lead. The scintillator is read out through acrylic waveshifters glued to lightguides that pass through the hadronic calorimeter to Hamamatsu R580 photomultiplier tubes. There are two phototubes per tower. The CEM has a depth of 18 radiation lengths and one hadronic absorption length. The energy resolution $\delta E_T/E_T = 13.5\%/\sqrt{E_T} \oplus 2.0\%$, where $E_T$ is in GeV and $\oplus$ indicates that the two terms are to be added in quadrature. The device is calibrated *in situ* using LED's,

xenon flashers, and radioactive sources of known energy and intensity[37]. In addition, the response map of the wedge was determined with testbeam electrons[38].

Inside the CEM, at a depth of 6 radiation lengths corresponding to electromagnetic shower maximum, the Central Strip Chambers (CES)[36] measure the shower profile in both the $r$-$\phi$ and $z$-directions. The strip chambers identify the location of the shower maximum to within about 2 mm in each view. The matching of the extrapolated track position to a cluster in the strip chambers is a powerful tool in electron analyses. In addition, observed shower profiles can be compared using a $\chi^2$ test to that of testbeam electrons, for additional background rejection.

Behind the CEM, the Central Hadronic Calorimeter (CHA)[39] consists of steel plates sandwiched between layers of acrylic scintillator. As in the CEM, the tower size is 0.1 in $\eta$ by 15° in $\phi$. The CHA is 4.5 absorption lengths thick, and has an energy resolution $\delta E_T/E_T$ of $80\%/E_T \oplus 3\%$ for isolated pions[40].

The electromagnetic and hadronic calorimeters in the plug ($1.1 < |\eta| < 2.4$) and forward ($2.2 < |\eta| < 4.2$) regions use gas proportional chambers with cathode pad readout. These calorimeters have been described elsewhere[41, 42]. They are used in this analysis to measure the energy in the event coming from particles other than the primary electron or muon; an imbalance in this energy is used to infer the presence of a neutrino.

## 3.3 Muon Chambers

CDF uses two systems to identify muons that penetrate the calorimeters. In the central region, $|\eta| < 0.6$, four planes of drift chambers constitute the Central Muon System (CMU)[43]. The CMU is segmented into 12.6° wedges that are mounted outside each 15° central calorimeter wedge at a radial distance of 3.5 m from the beam axis. Thus there is a 2.4° gap in $\phi$ between adjacent wedges. Each CMU wedge is further segmented into three 4.2° modules. And each module consists of

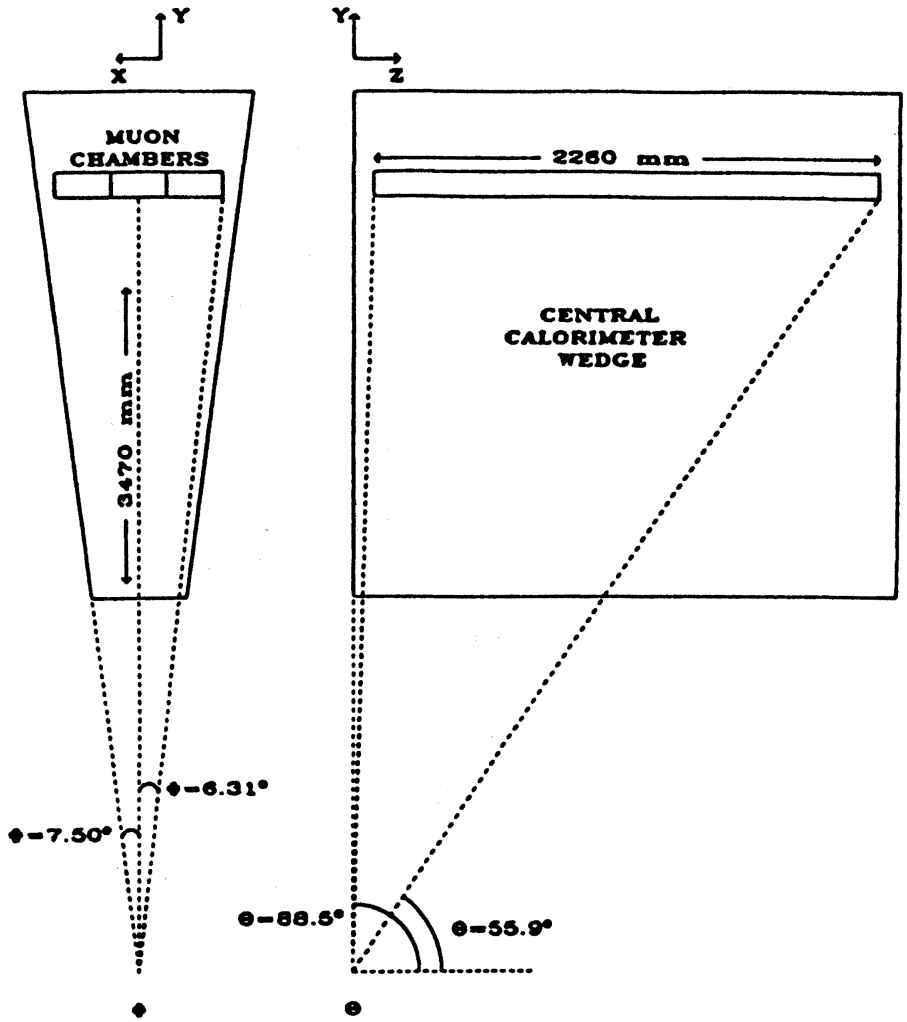


Figure 14. View of a central calorimeter wedge, showing the location of the central muon chambers.

four layers of rectangular drift cells of size 63.5 mm in the $r$-$\phi$ direction $\times$ 26.8 mm high $\times$ 2261 mm long. A 50 $\mu$m sense wire runs down the length of each cell, parallel to the beam axis. The location of the CMU chambers within the central calorimeter is shown in Figure 14. The arrangement of the four planes of drift chambers in a module is shown in Figure 15.

The CMU measures four points along the trajectory with an accuracy of 250 $\mu$m per point in the $\phi$ direction. Charge division is used to measure the $z$-position with

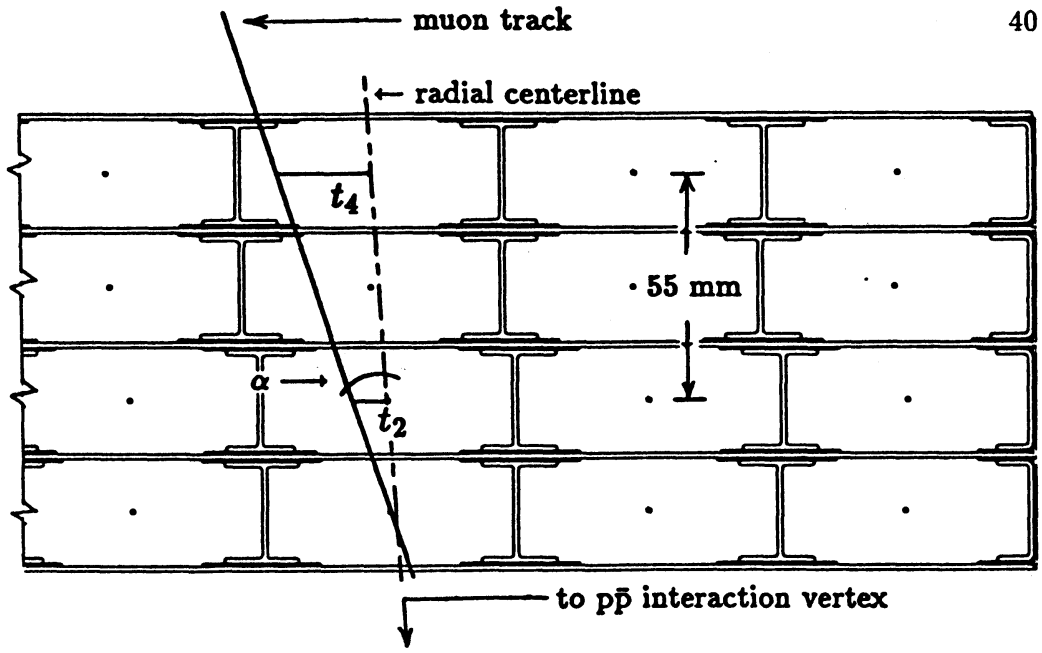


Figure 15. View of the four planes of drift chambers in a 15-degree central muon module. The view is along the beam direction.

a resolution of 1.2 mm per point. The measured track position in the CMU can be compared to the extrapolated position inferred from the CTC measurement for use in muon analysis.

In the forward and backward regions, $2.0 < |\eta| < 3.6$, muons are identified in the Forward Muon Spectrometer (FMU)[44]. In each hemisphere, three layers of drift chambers, interspersed with two 395-ton magnetized steel toroids, measure the muon trajectory with an accuracy of 5° in $\phi$ and 200 $\mu$m in the radial direction. The momentum resolution is roughly 13% for muons with $P_T > 8$ GeV. These chambers are used in this analysis to identify the decay $Z \rightarrow \mu\mu$, where one muon reaches the CMU and the other reaches the FMU. Such decays are a potential source of background in the $W' \rightarrow \mu\nu$ search.

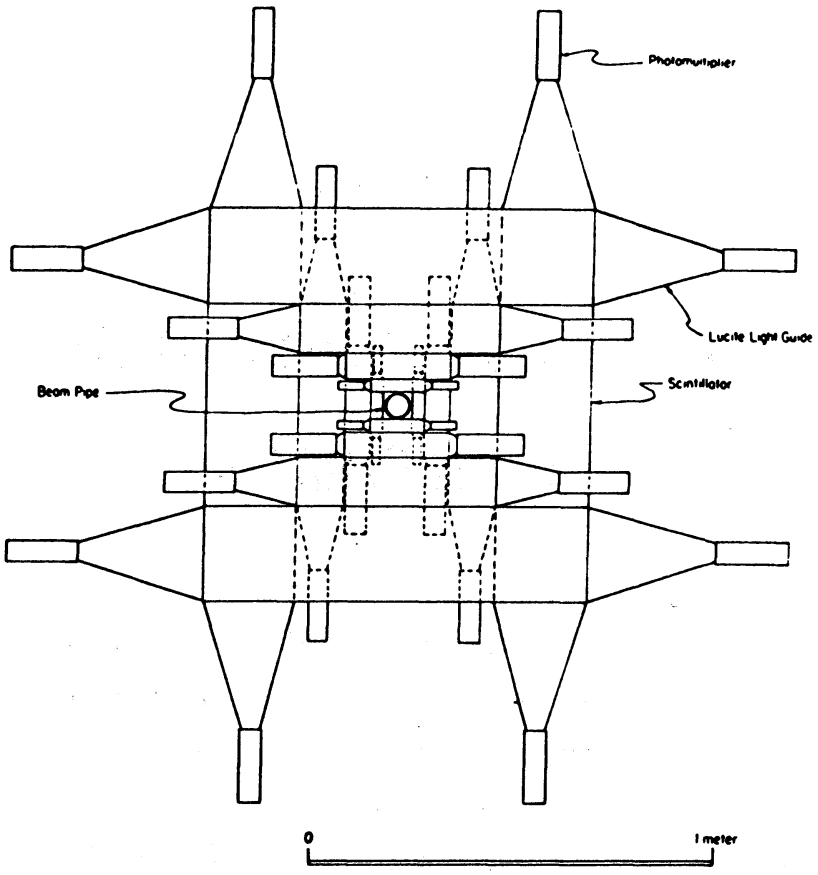


Figure 16. Beam's-eye view of one of the beam-beam counters (BBC's).

## 3.4 Luminosity Monitors

An accurate knowledge of the luminosity is important for any cross section measurement. CDF measures the luminosity using the observed rate of coincidences in the east and west Beam-Beam Counters (BBC's)[45]. These are planes of scintillators located at small angles relative to the beam ($3.24 < |\eta| < 5.90$) and mounted on the face of the forward calorimeters. One of the BBC's is shown in Figure 16.

# CHAPTER 4

# ELECTRON AND MUON TRIGGERS

In this chapter we describe the triggers used to select the electron and muon events that are the starting point for this analysis. The need for a fast, reliable, and selective trigger can be appreciated by considering a few numbers. The typical instantaneous luminosity during the 1988–89 run was approximately $1 \times 10^{30}$ cm$^{-2}$ sec$^{-1}$. The total cross section in the beam-beam counters at $\sqrt{s} = 1.8$ TeV was measured by CDF to be 46.8 mb. These numbers imply that roughly 50,000 inelastic collisions take place each second inside the CDF detector. By contrast, a $W \rightarrow e\nu$ event is produced once every 8-10 minutes, a $Z \rightarrow e^+e^-$ event every 2 hours, and a $t\bar{t} \rightarrow e^{\pm}\mu^{\mp} + X$ event about every 2 weeks, for $m_{top} = 100$ GeV. These production rates must be multiplied by the probability that the leptons hit a fiducial region of the detector, are not buried in a jet, and so forth—the real rate of observable events is even lower. Furthermore, the CDF data acquisition system can write only one or two events per second to tape. Clearly, then, if one is to observe the most rare and interesting events, a sophisticated trigger system is a necessity.

The solution is a 4-level system optimized for high-$P_T$ physics. Each level can accept or reject an event; if the event is rejected the trigger becomes live for the next

beam crossing, and if the event is accepted it is passed on to the next level, where more sophisticated information (and greater time) is available for the decision. If the event is accepted by the final level, the event is logged to tape. The CDF trigger has been described in detail elsewhere[46, 47]; the discussion that follows is an outline intended to illuminate the subsequent analysis.

## 4.1 Hardware Triggers: Levels 0, 1, and 2

The lowest three levels of the trigger have the task of reducing the rate from approximately 50,000 Hz to less than 10 Hz without incurring significant dead-time. The system, which was built primarily by the University of Chicago in the mid-1980's[1] consists of roughly three hundred custom-built Fastbus boards, whose communication and synchronization is governed by a central Timing Control. We now discuss the three levels of this trigger in order of increasing sophistication.

### *4.1.1 Level 0*

The level 0 trigger is motivated by the time requirements of the level 1 trigger, which is described in the next section. The level 1 trigger takes about 7 $\mu$sec to reach a decision. However, the time between beam crossings is 3.5 $\mu$sec, so the trigger system is dead for the next beam crossing after the level 1 algorithm is initiated. It is therefore desirable to activate level 1 only for beam crossings in which an inelastic collision actually takes place, which at the typical luminosity of $10^{30}$ cm$^{-2}$s$^{-1}$ is approximately one in every six crossings. The detection of these inelastic collisions is the purpose of level 0.

The level 0 trigger makes use of the beam-beam counters (BBC's), planes of

[1] The muon trigger subsystem was built by the University of Illinois, and the hardware track-finder used in level 2 by Fermilab.

scintillators located at small angles to the beam pipe in a rectangular region with pseudorapidity $|\eta|$ between 3.2 and 5.9. These scintillators have a time resolution of less than 200 ps. A coincidence of hits in the east and west BBC's, during a 15 nsec gate centered on the time of the beam crossing, signals an inelastic event. Most such events satisfy this trigger, and the narrow gate is useful for rejecting out-of-time backgrounds from cosmic rays, stray single particles from the Main Ring and Tevatron accelerators, and beam–gas collisions. The level 0 trigger reaches a decision in much less than the 3.5 $\mu$sec between beam crossings, and thus operates without deadtime.

### *4.1.2 Level 1*

Following a level 0 accept, the level 1 trigger is initiated. Here we describe the level 1 triggers of most interest to this analysis, namely the electron and muon triggers.

The level 1 muon trigger[48] requires hits in the central muon chambers ($|\eta| < 0.6$) consistent with a particle originating from the collision region. As can be seen from Figure 15, a measurement of the time difference between hits in successive layers of the muon chambers is equivalent to a measurement of the track's slope, and the slope in turn is related to the particle's transverse momentum, because of the bending in the central magnetic field and the multiple Coulomb scattering in the calorimeter. The trigger requires a coincidence between hits in two of the four layers, in a time window determined by the desired $P_T$ threshold:

$$\min(|t_4 - t_2|, |t_3 - t_1|) < t_{max},$$

where $t_1 \ldots t_4$ are the times at which the chambers are hit, and $t_{max}$ is the time difference corresponding to the $P_T$ threshold we wish to trigger on. During the first part of the 1988–89 run, a 5 GeV $P_T$ threshold was used, corresponding to a $t_{max}$ of 30 nsec. During the latter part of the run, when most of the data for this thesis was

collected, the threshold was lowered to 3 GeV, corresponding to a $t_{max}$ of 70 nsec. The cross section for this trigger is 280 $\mu$b, which at a luminosity of $10^{30}$ cm$^{-2}$s$^{-1}$ gives a rate into level 2 of 280 Hz.

Muons from $W$'s, $Z$'s, and other high-$P_T$ electroweak processes are a very small component of this rate. The level 1 muon trigger is dominated by hadrons whose hadronic cascade in the calorimeters and steel shielding reaches the muon chambers, and by low-$P_T$ muons from the decay-in-flight of pions and kaons. Fortunately, this trigger is very efficient for the high-$P_T$ muons of interest for this analysis. The efficiency of the level 1 central muon trigger was measured[49] to be $92.3 \pm 0.5\%$, for muons with $P_T > 15$ GeV, using muons identified in events that passed other triggers, and in cosmic ray events. However, this number is pulled down slightly by greater inefficiencies near the edges of the muon chambers. If we restrict the muons to the fiducial region of the chambers, away from the edges, the efficiency is $93.4 \pm 0.5\%$[50]. The reason that this number is not closer to 100% is not fully understood, but the inefficiency is believed[49] to originate from $\delta$-rays generated by the muons, which may confuse the timing and cause the muon's momentum to be mismeasured.

The level 1 electron trigger uses sums of energy from the calorimeters to make its decision. Analog signals from the electromagnetic and hadronic calorimeters are available separately, and are segmented into "trigger towers" of size 0.2 in $\eta$ by 15° in phi. There are a total of 2112 such inputs: $44 \times 24$ to cover the range $-4.4 < \eta < 4.4$ in pseudorapidity and $0° < \phi < 360°$ in azimuthal angle, for both electromagnetic and hadronic calorimeters. Each tower is compared to a preset threshold, which may vary depending on the calorimeter, and those towers above threshold participate in analog sums in which the total transverse energy $E_T$ is calculated.

The level 1 electron trigger path uses a single-tower threshold of 6 GeV in the central electromagnetic calorimeter. The thresholds in other calorimeters are set to full-scale, so effectively only the CEM participates in the sum. The trigger requires

that the total $E_T$ in CEM towers above the 6 GeV threshold be greater than 6 GeV—that is, the trigger requires at least one tower in the CEM to be above 6 GeV. No tracking information is available at this stage, so this trigger also serves to pick up central photons. Of course, most events accepted by this trigger are neither electrons nor photons but hadronic showers with a significant EM content. At this level of the trigger, however, the aim is not to obtain an exceptionally pure sample of the objects of greatest interest, but rather to remain highly efficient for real electrons and photons while reducing the rate to a point where events can be examined more carefully in level 2. The cross section for the level 1 electron trigger is approximately 19 $\mu$b, which at a luminosity of $10^{30}$ cm$^{-2}$s$^{-1}$ gives a rate into level 2 of approximately 19 Hz. This trigger is essentially 100% efficient for electrons with $E_T > 15$ GeV.

### *4.1.3 Level 2*

If an event is accepted by level 1, it is passed to level 2. At the beginning of the level 2 cycle, "clusters" are identified, where a cluster for our purposes is the association of a two-dimensional track ($\phi$ and $P_T$ information, but no $z$ information) either with hits in the muon chambers (a muon cluster) or with a localized region of energy deposition in the CEM (an electron cluster). (Other clusters identified in level 2 include photon, jet, and "stiff track" clusters.) Two-dimensional tracks are found by a hardware track processor[51] that examines the hits in the axial layers of the CTC. It has a momentum resolution $\delta P_T/P_T = 3.5\% \times P_T$. The list of clusters is made available to a special processor, which examines it to determine if trigger conditions were satisfied. It is not possible to reconstruct three-dimensional tracks in the short time available for the level 2 decision—such a task requires 1-2 seconds of VAX cpu and is not performed online. However, the presence of 2D-tracks in level 2 is itself an extremely powerful tool for reducing the background while keeping the signal.

The heart of the level 2 trigger is a single Fastbus crate (the processor crate) with a custom ECL backplane that permits high-speed communication between the modules in the crate. The list of clusters is stored in cluster memory modules (CLM's), and is examined by several so-called Mercury boards. These boards contain simple logic that, for example, counts the number of electron and muon clusters above various preset energy thresholds, and calculates the ratio of total energy to electromagnetic energy in electron-type clusters. This information is used by the level 2 processor to reach a trigger decision. The level 2 processor executes a program that is downloaded at the beginning of a run. One can think of each of the level 2 trigger paths as a subroutine; the event is accepted by level 2 if at least one of the paths is satisfied.

The level 2 muon trigger used in this analysis requires a track with $P_T > 9.2$ GeV, whose extrapolated position at the radius of the muon chambers is within $\pm 7.5°$ in azimuth of muon chamber hits that satisfied the level 1 trigger condition. The efficiency of this trigger is $97.2^{+1.5}_{-2.7}\%$ for muons with $P_T > 15$ GeV[52]. However, since this trigger requires a level 1 muon trigger as a prerequisite, the combined efficiency of the level 1 and level 2 muon trigger is $90 \pm 2\%$. The cross section for this trigger is 1.1 $\mu$b, which gives a rate of approximately 1 Hz at $\mathcal{L} = 10^{30}$.

The level 2 electron trigger used in this analysis requires an EM cluster with $E_T > 12$ GeV and a ratio of hadronic to electromagnetic energy of less than 12.5%. In addition, a track with $P_T > 6$ GeV was required to point at the cluster. The efficiency of this trigger was measured using $W \rightarrow e\nu$ events that were selected with a missing energy trigger. Another unbiased electron sample is provided by the "other" electron in $Z \rightarrow ee$ events where the first electron satisfies the trigger condition. Both methods give consistent results, though the latter has less statistical power due to the relatively small number of $Z$'s that decay to two central electrons. The measured efficiency of this trigger is $97.3 \pm 0.5\%$[53]. The electron trigger cross section is 0.47 $\mu$b, corresponding to 0.5 Hz at $\mathcal{L} = 10^{30}$.

## 4.2 Software Trigger: Level 3

Following an accept by the level 2 trigger, the full detector is read out, and the information from all detector channels is made available to level 3. The level 3 trigger consists of a "farm" of 60 Motorola 68020 processors, which execute a streamlined version of the Fortran-based offline reconstruction code. In particular, the offline clustering and energy-calculation algorithms are applied, although full three-dimensional track reconstruction is not. The level 3 electron and muon decision criteria are in essence those used in level 2—namely, a track pointing at an EM cluster or muon chamber hits—but because the full detector data are available and the rate is a relatively manageable 4-5 Hz, there is time to perform a more accurate calculation of the energy and track momentum. A fast two-dimensional track-finding algorithm (known as "DF tracking" for "Damn Fast") is executed; this algorithm finds tracks with high efficiency with a resolution of $\delta P_T/P_T = 0.77\% \times P_T$. The offline energy clustering makes use of the fine segmentation of the calorimeter ($0.1 \times 15°$ in $\eta$–$\phi$ space, in contrast to the $0.2 \times 15°$ towers used in levels 1 and 2) and employs the most recent calibration constants. In addition, certain types of noise can be recognized and removed.

The level 3 muon trigger requires a DF track with $P_T > 11$ GeV that extrapolates to a segment of hits in the muon chambers. It does not require the level 2 muon trigger as a prerequisite. The cross section is 130 nb, giving a rate of 0.1 Hz at $\mathcal{L} = 10^{30}$. The level 3 electron trigger requires a central EM cluster with $E_T > 12$ GeV as reconstructed by the offline clustering algorithm, together with at least one DF track with $P_T > 6$ GeV. The ratio of hadronic to electromagnetic energy in the cluster is required to be less than 0.125. For electrons with EM $E_T$ between 12 and 20 GeV, a very loose cut is applied on the amount of energy in calorimeter towers adjacent to the electron. This trigger requires the level 2 electron trigger as a prerequisite, and has a cross section of 250 nb, which is 0.25 Hz at $\mathcal{L} = 10^{30}$.

Events that pass the level 3 trigger are logged to 9-track tapes. Eventually these

events are fully reconstructed—a process known as Production—and become grist for the analysis mill.

# CHAPTER 5

# EVENT SELECTION

The data used in this analysis were collected during the Tevatron collider run that took place between June 1988 and June 1989. During this period, the Tevatron delivered an integrated luminosity of 8.5 $pb^{-1}$, of which 4.1 $pb^{-1}$ were recorded on tape by CDF. (The difference between the delivered and recorded luminosities is due in roughly equal parts to CDF down time and to trigger and data acquisition dead time.) CDF recorded approximately six million events on five thousand 9-track tapes. In this chapter we describe how we select from this large sample the few thousand events used in our analysis.

## 5.1 Production

After events have been recorded on tape, they are passed through the sequence of offline reconstruction algorithms known as Production. Production converts the raw data—pulse heights in phototubes and on wires, TDC counts, and so forth—into higher-level physics objects: pulse heights are turned into energies, TDC counts are turned into drift distances, and these in turn are used to form energy clusters and tracks. At still a higher level, the clusters and tracks can be "linked" to form electron, muon, and jet candidates. In addition, global quantities such as the missing

energy are calculated. The resulting event record is stored in a large array about 150 kilobytes in size. The array is subdivided into smaller sections—known as banks—that contain information associated with a particular detector component or physics object. One bank, for example, contains a list of the energy deposited in every calorimeter tower, another contains a list of tracks, and others contain a collection of information from many detectors that is relevant to the identification of electron and muon candidates. The point is that at the end of the Production process, the information needed to perform an analysis has been assembled into an easily[54] accessible form. The next step is up to the individual physicist.

The event samples for the $W' \rightarrow e\nu$ and $W' \rightarrow \mu\nu$ search are selected with cuts designed to remain efficient for real electrons and muons while rejecting most sources of background. That it is possible to find such a set of cuts is a statement not only about the relatively clean nature of the physics we are investigating, but also about the quality of the CDF detector itself. In addition, because this search is concerned principally with high-$P_T$ electrons and muons coming from the decay of a very heavy object, it is important to use cuts whose efficiency remains high even for the most energetic leptons.

## 5.2 Electron Sample

The selection of the electron sample proceeds in two steps. First, we apply very loose cuts to obtain a central electron sample that is small enough to work with conveniently, while at the same time being large enough to permit a determination of backgrounds. We then apply our analysis cuts to this sample.

The loose central electron sample is selected from events that pass the level 2 electron trigger. Events are required to have at least one energy cluster in the central electromagnetic calorimeter (CEM) with $E_T > 30$ GeV and a ratio of hadronic to electromagnetic energy, HAD/EM, less than 10%. In addition, a track in the central

tracking chamber (CTC) with $P_T > 8$ GeV is required to point to the cluster using loose matching criteria. There are approximately 42,000 events in this sample, which has in integrated luminosity of 4.36 $\text{pb}^{-1}$. We emphasize that, although this sample is called an "electron sample," only a small portion of these events contain "real" electrons. The majority of these events contain QCD jets that deposited most of their energy in the electromagnetic portion of the calorimeter. This process can come about from the overlap of a $\pi^0$ (which decays to two photons and leaves a large amount of electromagnetic energy) with a charged pion or kaon (which produces a track), or simply from a charged pion that showers primarily in the electromagnetic calorimeter. Our remaining cuts remove these events with high efficiency[55].

A series of cuts are now applied to select $W$ and $W'$ candidates from the large central electron sample. These cuts include:

1. **Fiducial cuts.** The electron candidate is required to lie in a region of the CEM where the energy response is both linear and well-understood. We eliminate in this way electrons that landed in cracks between calorimeter cells, in towers with large calibration corrections, and in other problematic areas of the detector.

2. **Bad run cuts.** Some runs contain peculiarities that could bias electron analysis: a large number of dead channels, for example, or anomalies in minimum bias data. Events from these runs are excluded, reducing the total exposure to 4.15 $\text{pb}^{-1}$. The bad run and fiducial cuts are described in more detail in ref. [56].

3. **Event vertex.** The event vertex (the location in $z$ of the primary interaction) is required to lie within $2\sigma$ (60 cm) of the center of the detector at $z = 0$.

4. **Electron quality cuts.** These cuts are designed to eliminate mismeasured jets and other sources of "fake" electrons. We require:

- Ratio of hadronic to electromagnetic energy in the cluster (HAD/EM) less than 10%.
- Good position matching between the extrapolated CTC track and the cluster position measured in the strip chambers. Specifically, we require the track and cluster positions to match within 3.0 cm in the $z$-direction and 1.5 cm in the $r$-$\phi$ view.
- Ratio of cluster energy to track momentum ($E/P$) less than 2.
- Less than 5 GeV of energy in calorimeter towers bordering the electron candidate cluster. This cut is particularly powerful for the rejection of QCD backgrounds.

5. **Missing energy.** We require the missing transverse energy, $\not{E}_T$ to be greater than 30 GeV.

6. **Other cuts.** Finally, $Z$'s are rejected by throwing out events containing a second electromagnetic cluster whose invariant mass with the first cluster lies within 20 GeV of the $Z$ mass (91 GeV). In addition, conversions are rejected by vetoing those events containing a second track near the primary track whose charge is opposite and whose invariant mass with the first track is near zero. Very high-$P_T$ conversions may have overlapping, indistinguishable tracks, so we also reject events in which the track left only a small number of hits in the vertex chamber (VTPC).

Histograms of the variables we cut on are shown in Figure 17. In each histogram, cuts have been applied to all variables except the one being plotted. (Note, however, that the HAD/EM cut was applied earlier in the event selection process, so that there are no events with HAD/EM $> 0.1$ in the plot.) The final histogram, showing the missing energy, is not an electron identification variable *per se*, but this plot indicates the very clean nature of our sample after the other cuts have been imposed. Clearly visible is the peak around 40 GeV associated with $W$ boson decay. The background

at low values of the missing energy comes from the semileptonic decays of heavy quarks, and from QCD processes that can mimic the appearance of an electron in the detector. With all cuts applied, the final electron sample contains 1796 events. The transverse mass for events in this sample is shown if Figure 18, together with the distribution for the process $W \rightarrow e\nu$ as predicted by Monte Carlo. The highest transverse-mass event is at 185 GeV, with 6 events possessing a transverse mass greater than 120 GeV. Visually, there is no indication of a second peak that would indicate the presence of a $W'$.

## 5.3 Muon Sample

Selection of the muon sample proceeds in much the same way as for the electron sample. We begin by selecting a large, general-purpose muon sample with loose cuts, and continue by applying tighter, analysis-quality cuts to this restricted sample.

The Production process produces a very large sample of high-$P_T$ muon candidates, selected from events passing the muon triggers. Events are required to have a track with $P_T$ greater than 10 GeV, whose extrapolated position at the radius of the central muon chambers is within 10 cm (in the $r$-$\phi$ view) of a segment of hits in the muon chambers. From this sample (which occupies several hundred tapes), a preliminary event selection is made[57] to produce the sample that is the starting point for our analysis, the counterpart to the large high-$E_T$ central electron sample described above. The preliminary central muon sample keeps events containing a track with $P_T$ greater than 18 GeV, matched to a track segment in the muon chambers to within 10 cm in the $r$-$\phi$ view. In addition, the calorimeter tower to which the track points is required to have less than 2 GeV of electromagnetic energy and 6 GeV of hadronic energy. Because muons are minimum-ionizing particles, this cut enhances the muon content of the sample, which nonetheless consists largely of purely hadronic events where a pion or kaon penetrated through the calorimeters

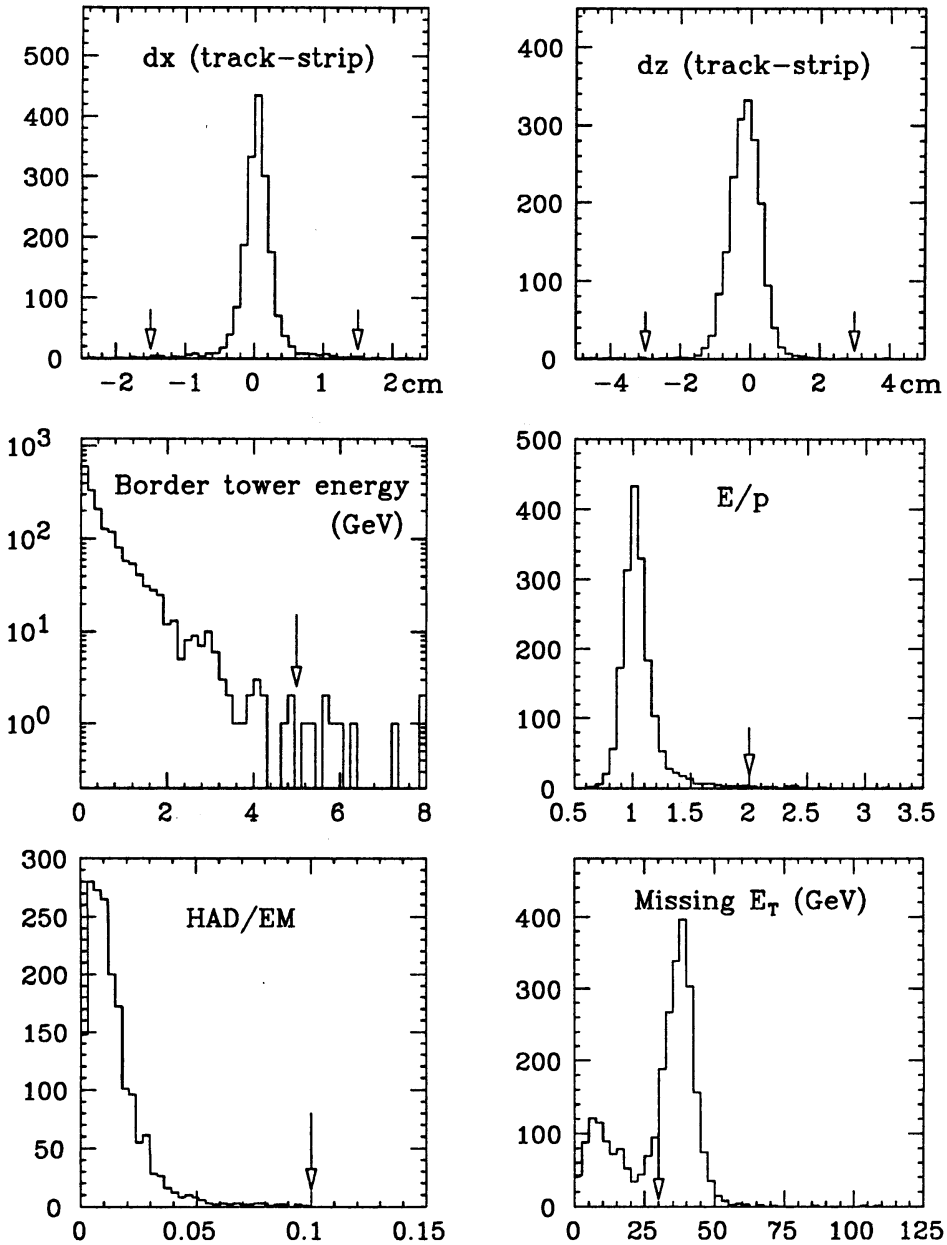


Figure 17. Electron identification variables. The arrows indicate the location of the cuts. In each of these plots, cuts have been applied to all variables except the one being plotted.

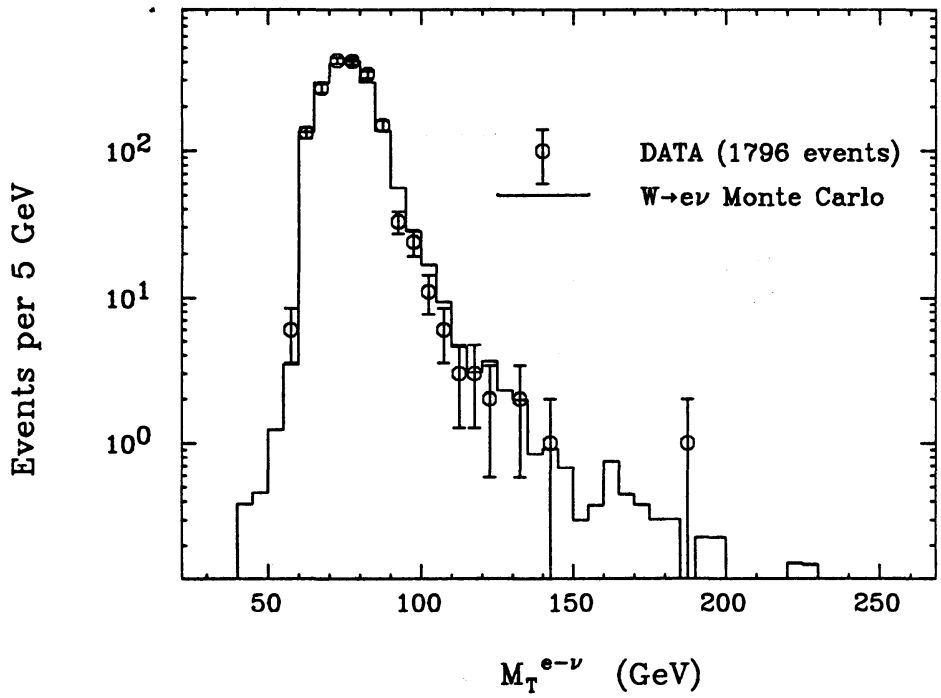


Figure 18. Observed transverse mass distribution for the electron sample. Error bars are statistical. Superimposed is the Monte Carlo prediction for $W$ boson decay.

and reached the muon chambers. This sample contains 11,487 events. We throw out events from early runs in which the muon trigger was malfunctioning, as well as events from bad runs, and a handful of events that did not pass the level 0 BBC trigger. (The latter were recorded during a special test run; ordinarily such events cannot make it to tape, since the BBC trigger is a prerequisite for level 1 and level 2.) The resulting sample of 9777 events has an integrated luminosity of 3.54 $pb^{-1}$.

Before the final analysis-quality cuts are imposed, the track pattern recognition and fitting code is rerun on this sample. This "retracking" is performed for two reasons. The first is that, by the time this analysis was performed, the tracking code had been improved considerably over the version used in Production. In particular, a better knowledge of the CTC alignment parameters resulted in improved momentum accuracy in the fitted tracks. With the Production alignment parameters, the systematic error in measuring a 100 GeV track is estimated[58] to be of order 10 GeV, and is non-negligible even for the 30-50 GeV tracks typical of $W$ and $Z$ decays. This fact alone is sufficient reason to retrack. In addition, however, the pattern recognition and fitting algorithm used by the newer tracking is better suited for this analysis than the version used in Production. Although Production tracking is somewhat more efficient (we estimate that the new tracking finds 98.7% of the tracks found by Production tracking), it is also prone to misidentify a low-$P_T$ secondary track segment, such as a muon from the decay-in-flight of a pion or kaon, or a backscattered particle from the face of the calorimeter, as a high-$P_T$ primary track. Sometimes these secondary tracks are reconstructed with very high $P_T$, making them a potential source of background to a $W'$ signal. We estimate that our sample would contain a 2% background from such secondaries if we did not retrack[50]. The newer tracking will reconstruct secondary tracks, but usually gives them a large impact parameter relative to the primary interaction vertex, which makes them easier to recognize as secondaries, and easy to remove with an impact parameter cut.

Beginning with this retracked sample, we first require that the event passed the primary level 2 central muon trigger. We then ask for a central muon candidate that satisfies the following cuts:

1. **Not a cosmic ray.** A cosmic ray filter[59] rejects back-to-back tracks with $P_T > 10$ GeV, as well as tracks whose timing information indicates that they were travelling "backwards" through the tracking chamber. Real tracks from $\bar{p}p$ collisions begin at the center of the detector and move outward, but cosmic rays penetrate the outer layers of the tracking chamber first and move inward. This filter was applied to all tracks in the event with $P_T > 10$ GeV.

2. **Beam constraint.** The muon candidate track must pass the beam constraint algorithm. Recall that this procedure, which constrains the track to originate from the primary event vertex, improves the momentum resolution by a factor of two. Essentially all good tracks pass this algorithm.

3. **Track quality cuts.** The muon candidate track must pass a very loose set of track quality cuts. Bad tracks include those with a much smaller than expected number of hits in either the axial or stereo layers or large mean residuals.

4. **Momentum cut.** Track $P_T$ (after beam constraint) greater than 30 GeV.

5. **Event vertex.** The event vertex is required to lie within $2\sigma$ (60 cm) of the center of the detector at $z = 0$.

6. **Fiducial cuts.** The CTC track (after beam constraint) is required to extrapolate to a region of the central muon chambers where the response is well-understood. In general this means that it cannot extrapolate to closer than a few centimeters of the muon chamber boundaries.

7. **Muon quality cuts.** The muon candidate is required to pass the following quality cuts:

- Less than 2 GeV of electromagnetic energy and less than 6 GeV of hadronic energy in the calorimeter tower to which the muon track extrapolates. This cut exploits the fact that muons are minimum-ionizing particles.
- Good matching between the extrapolated CTC track and the position of the hits in the muon chambers. We require that the two positions match to within 2 cm in the $r$-$\phi$ view and 15 cm in the $z$ view.
- Track has an impact parameter of less than 0.15 cm relative to the beam position. This cut rejects a small background from fake high-$P_T$ tracks that do not originate from the primary vertex.

8. **Isolation cut.** The muon candidate must have less than 5 GeV of energy in a cone of radius 0.4 in $\eta$-$\phi$ space, centered on the muon and excluding the energy in the tower traversed by the muon. This cut is effective at reducing QCD backgrounds.

9. **Not a $Z$.** Events from the process $Z \rightarrow \mu\mu$ are rejected by searching for tracks whose invariant mass with the muon candidate track is near the $Z$ mass. Approximately 40 events where the second muon reached the forward muon chambers are also rejected. These muons emerge from the interaction region at too small an angle to leave a track in the CTC. There is a remaining background from so-called central-plug $Z$'s, where the second track falls in the rapidity range $1.5 < \eta < 2.5$ and is not detected in either the CTC or forward muon chambers.

10. **Missing energy.** We require the missing transverse energy, $\not{E}_T$, to be greater than 30 GeV. Before imposing this cut, we correct the $\not{E}_T$ (which initially is determined solely from the energy deposited in the calorimeters) for the presence of the minimum-ionizing muon.

Histograms of the variables we cut on are shown in Figure 19.

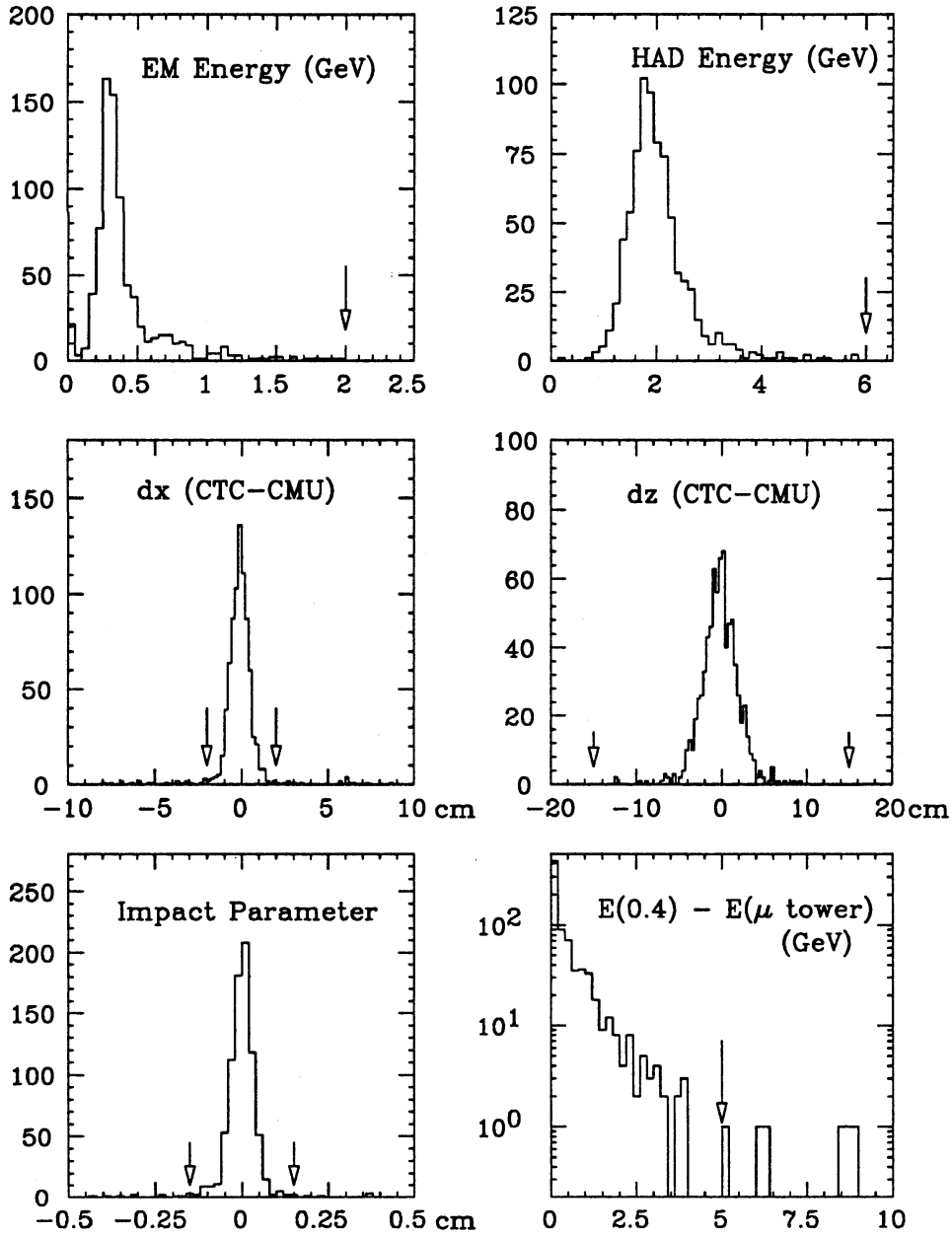


Figure 19. Muon identification variables. The arrows indicate the location of the cuts. In each of these plots, cuts have been applied to all variables except the one being plotted.

The final muon sample contains 783 events, 708 of which have a transverse mass above 65 GeV. This spectrum is shown in Figure 20, together with a Monte Carlo prediction for the process $W \rightarrow \mu\nu$. The highest transverse-mass event is at 205 GeV, and there are 12 events with a transverse mass above 120 GeV, which represents something of an excess over the $6 \pm 3$ events expected from $W$ production. We have given these events considerable study.

## 5.4 Events in the Tail

We have examined:

- Beam constrained fit using compressed and uncompressed tracking data.
- Quality of track and event parameters.
- Residual cosmic ray background.
- Comparison with the $W \rightarrow e\nu$ sample.
- Inefficiencies in $Z$ rejection, particularly central-plug $Z$'s.

We visually scanned the events with transverse mass above 110 GeV, and no obvious problems were noticed. Most of the events have jet activity. Because the CDF detector has a large uncertainty on its measurement of jet energies, events containing jets have a larger error on the measured missing energy, and therefore on the transverse mass, than do no-jet events. This is illustrated in Figures 21 and 22. The first figure shows the distribution of total transverse energy contained in jets ($\sum E_T(jet)$), for events in the muon sample. The second pair of figures shows the transverse mass distributions for events in which the $\sum E_T$ in jets is greater than and less than 30 GeV respectively. The transverse mass distribution in the former set of events is broader, and contains a tail extending to higher values of the transverse mass. Thus, there is a greater likelihood that $W$ bosons produced in conjunction

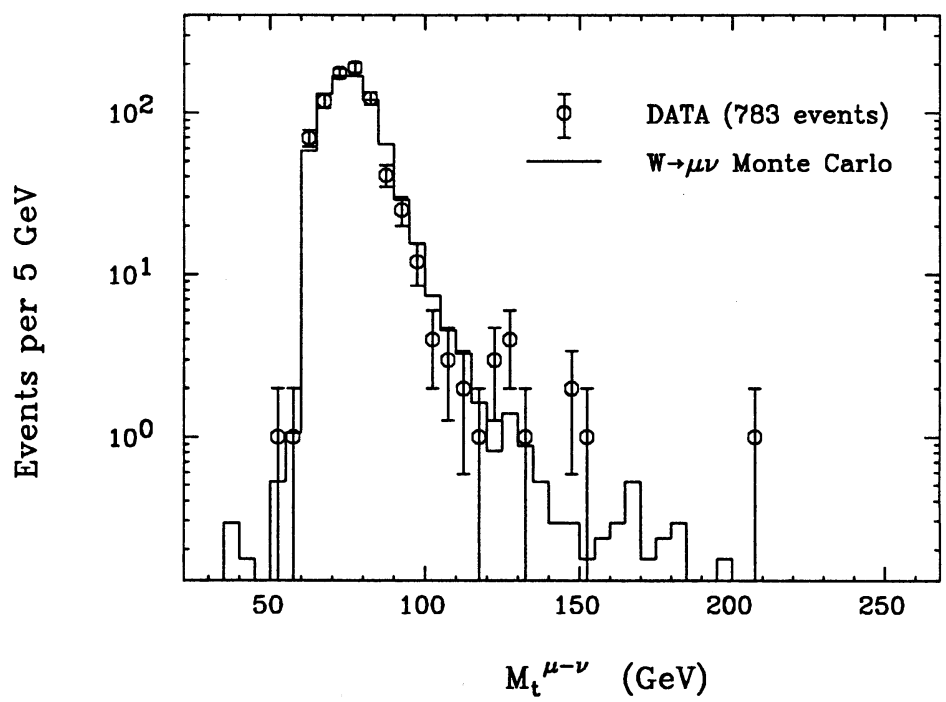


Figure 20. Observed transverse mass distribution for the muon sample. Error bars are statistical. Superimposed is the Monte Carlo prediction for $W$ boson decay.

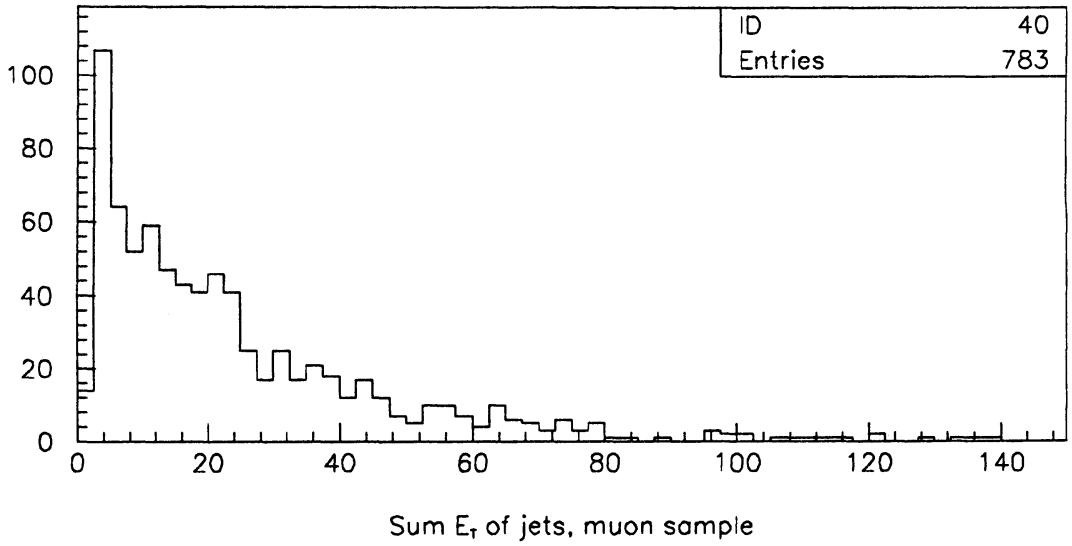


Figure 21. Total transverse energy (in GeV) contained in jets ($\sum E_T(jet)$) for events in the muon sample.

with jets will have a higher observed transverse mass. The observation that these high-transverse-mass events contain jets is therefore consistent with their arising from $W$ production, since a true $W'$ signal would have a peak at high-$M_T$ in both the jet and non-jet samples.

It is possible to improve the jet resolution, on average, by applying a correction that takes account of cracks in the detector, nonlinearities in the response of the calorimeters, and jet fragmentation properties. We have chosen not to use such a correction in this analysis. The effect of jet corrections is discussed in Appendix A.

### *5.4.1 Beam Constrained Fit*

The muon candidates in our sample were beam-constrained using the track parameters taken from a compressed version of the tracking data (the so-called QTRK bank). Some concern arose about a possible loss of resolution due to round-off er-

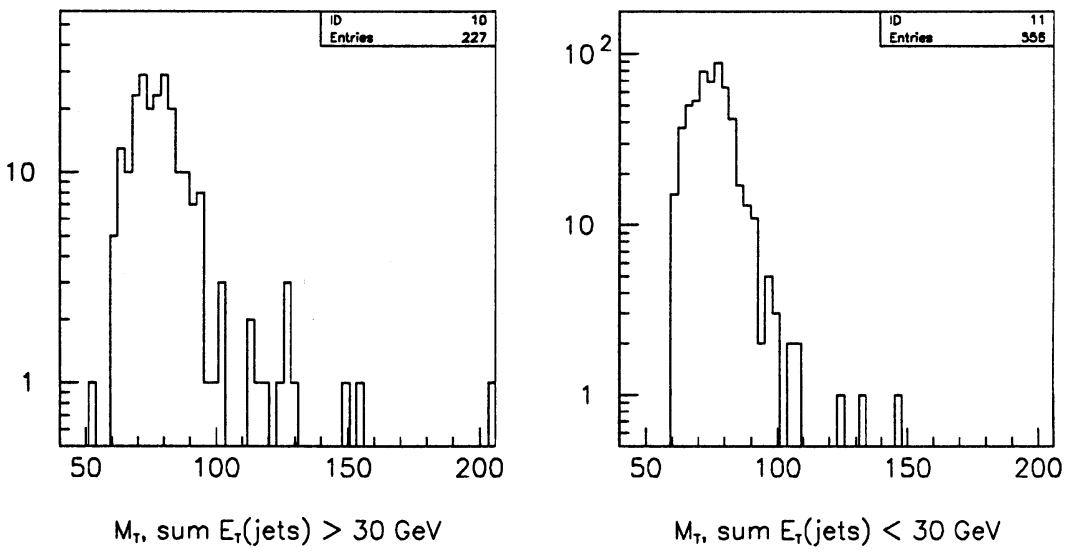


Figure 22. Transverse mass distributions (in GeV) for events in the muon sample with $\sum_T E_T(jet)$ greater than 30 GeV (left) and less than 30 GeV (right). Because of detector imperfections and nonlinearities, jet energy can be mismeasured, leading to a broader transverse mass distribution in events with substantial jet activity.

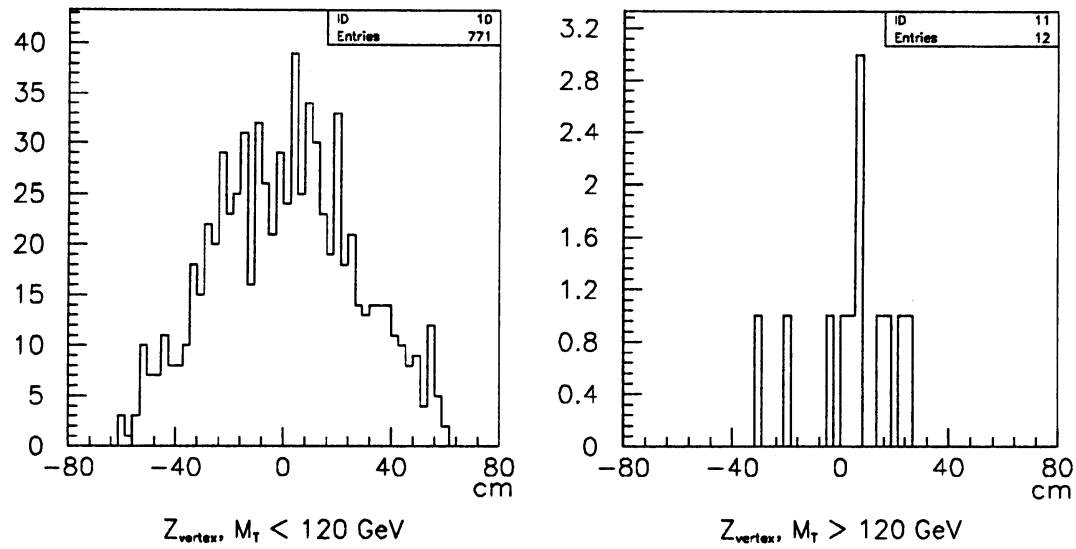


Figure 23. Event vertex distribution for events with $M_T$ less than 120 GeV (left) and greater than 120 GeV (right).

rors in the QTRK bank, especially for very small curvature values. The sample was therefore remade using information from the uncompressed data (the CTCS bank). There is no indication of significant differences. One event (with $M_T$ of 70 GeV) is lost if the $P_T$ and $\not{E}_T$ cuts are applied to the CTCS-derived quantities.

### *5.4.2 Event Parameters*

Characteristics of events in the tail have been compared to events with $M_T < 120$ GeV to look for any indications of problems in track reconstruction or muon identification. Figures 23–32 show relevant variables for the two categories of events. Although two of the high-$M_T$ events come close to failing the impact parameter cut, and one has unusually large tracking residuals, in general the high-$M_T$ events are well within the limits of the distributions, and within the statistics no systematic differences are found.

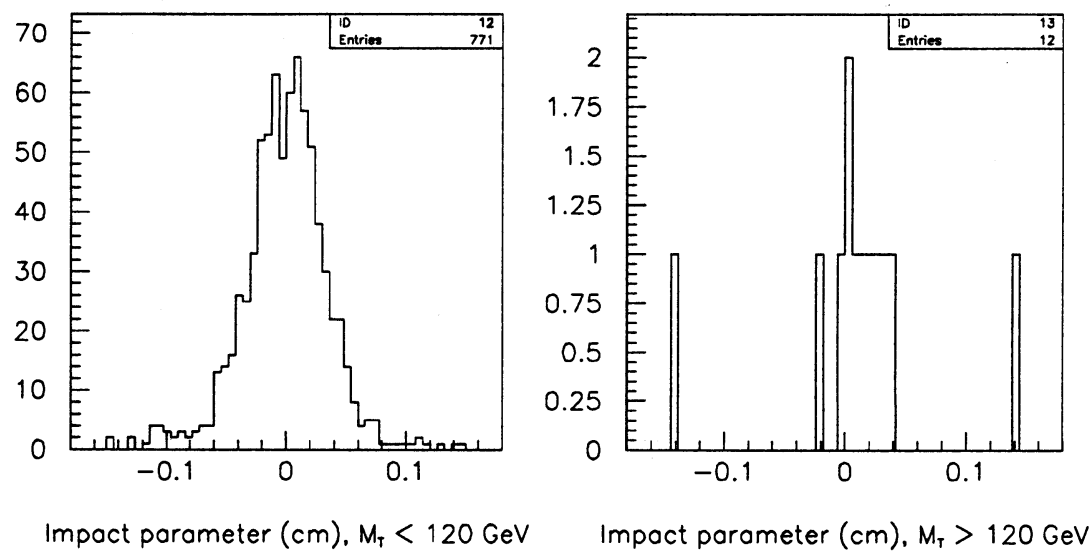


Figure 24. Impact parameter distribution for events with $M_T$ less than 120 GeV (left) and greater than 120 GeV (right).

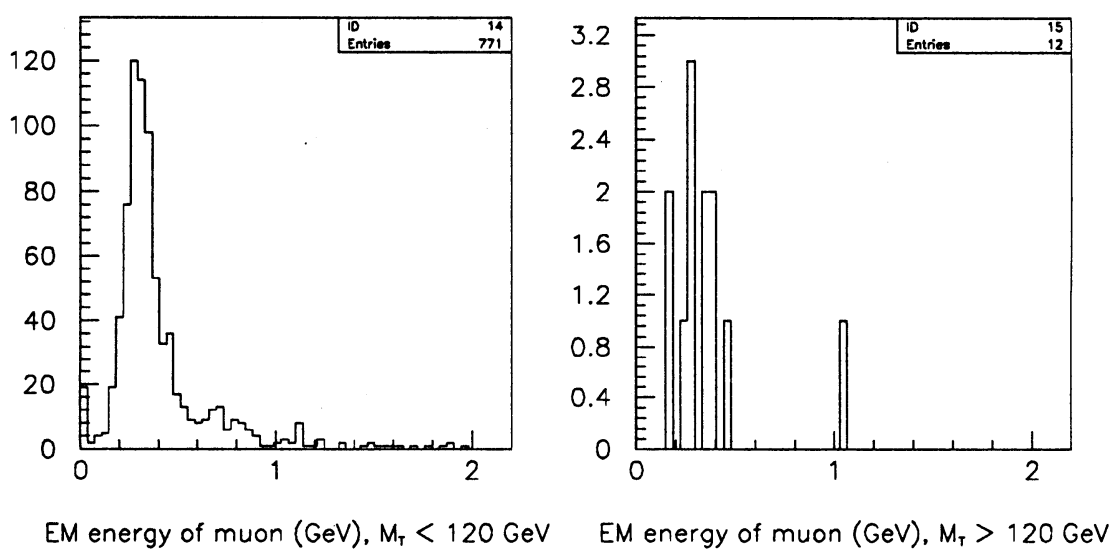


Figure 25. EM energy in the calorimeter tower traversed by the muon candidate, for events with $M_T$ less than 120 GeV (left) and greater than 120 GeV (right).

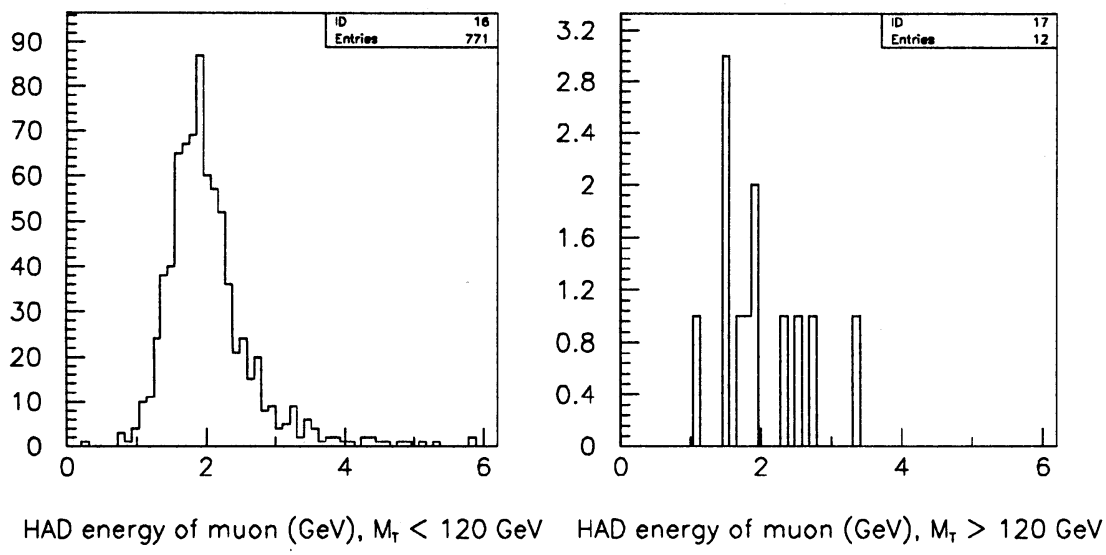


Figure 26. Hadronic energy in the calorimeter tower traversed by the muon candidate, for events with $M_T$ less than 120 GeV (left) and greater than 120 GeV (right).

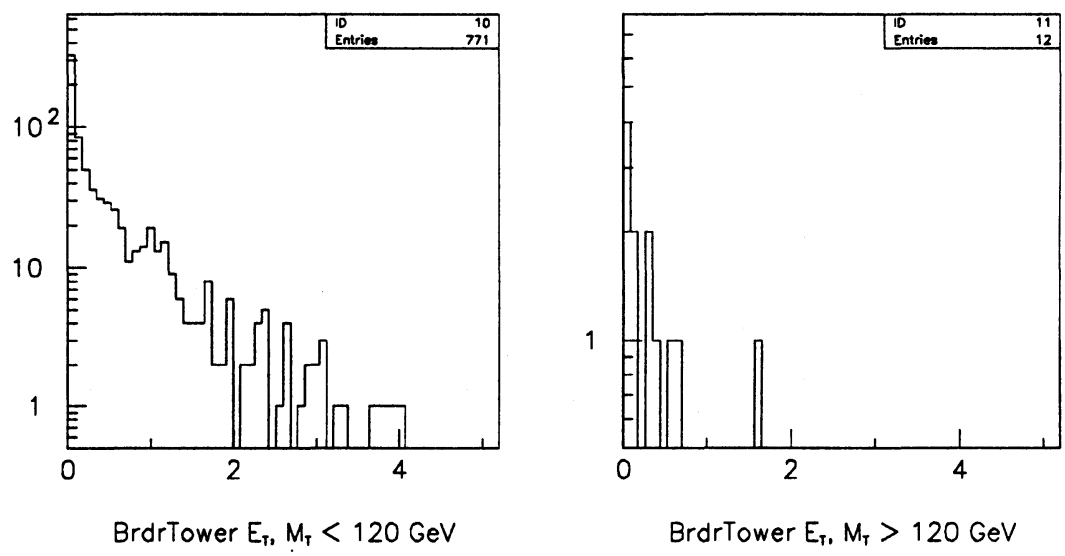


Figure 27. Transverse energy (in GeV) in the calorimeter towers surrounding the tower traversed by the muon candidate, for events with $M_T$ less than 120 GeV (left) and greater than 120 GeV (right).

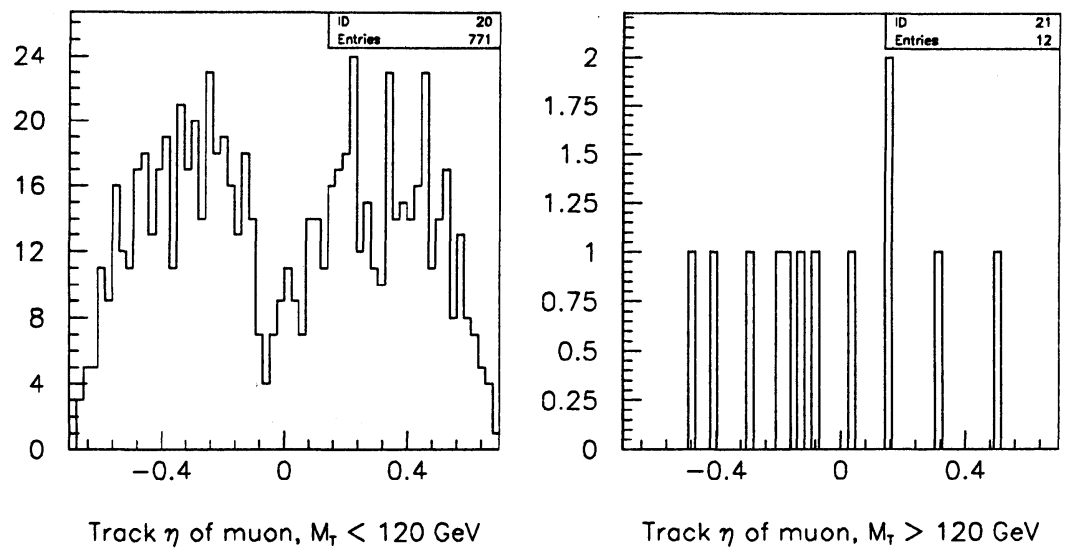


Figure 28. Muon pseudorapidity distribution for events with $M_T$ less than 120 GeV (left) and greater than 120 GeV (right). The dip in the middle is due to the 90° crack in the detector, where there is no muon coverage.

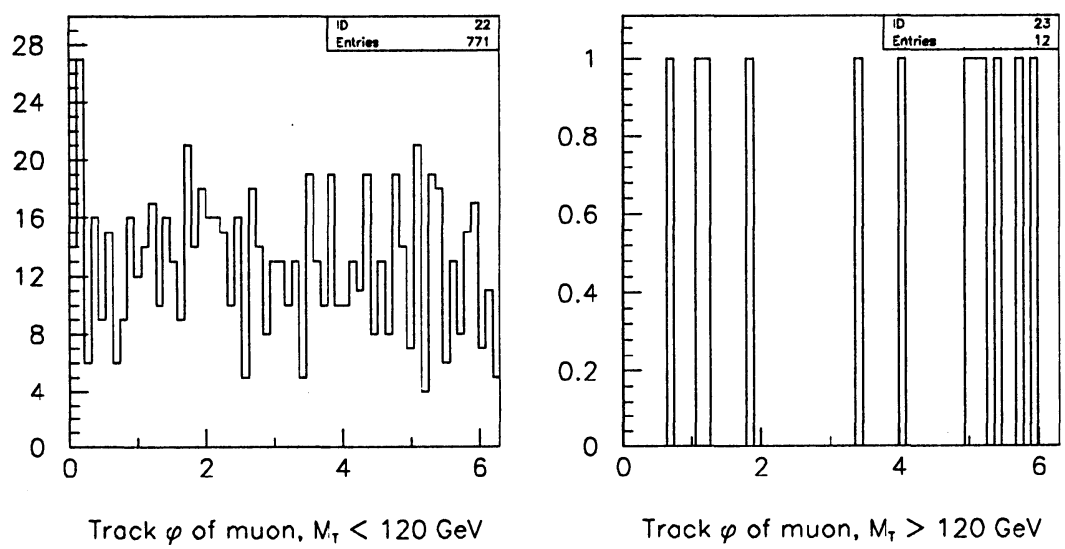


Figure 29. Azimuthal angle $\phi$ distribution for events with $M_T$ less than 120 GeV (left) and greater than 120 GeV (right).

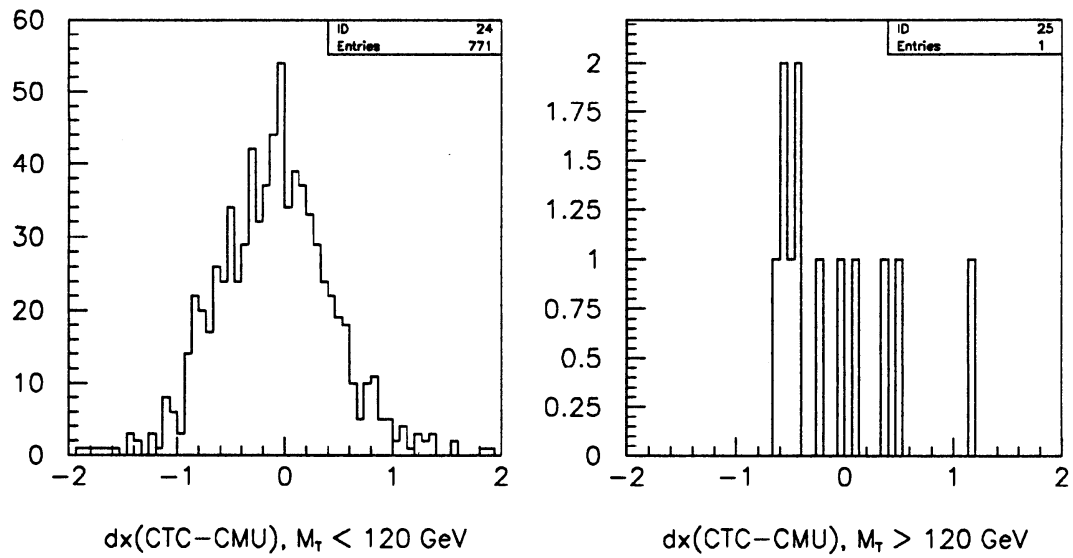


Figure 30. $R$-$\phi$ distance (in cm) between the extrapolated CTC track and the track segment in the muon chambers, for events with $M_T$ less than 120 GeV (left) and greater than 120 GeV (right).

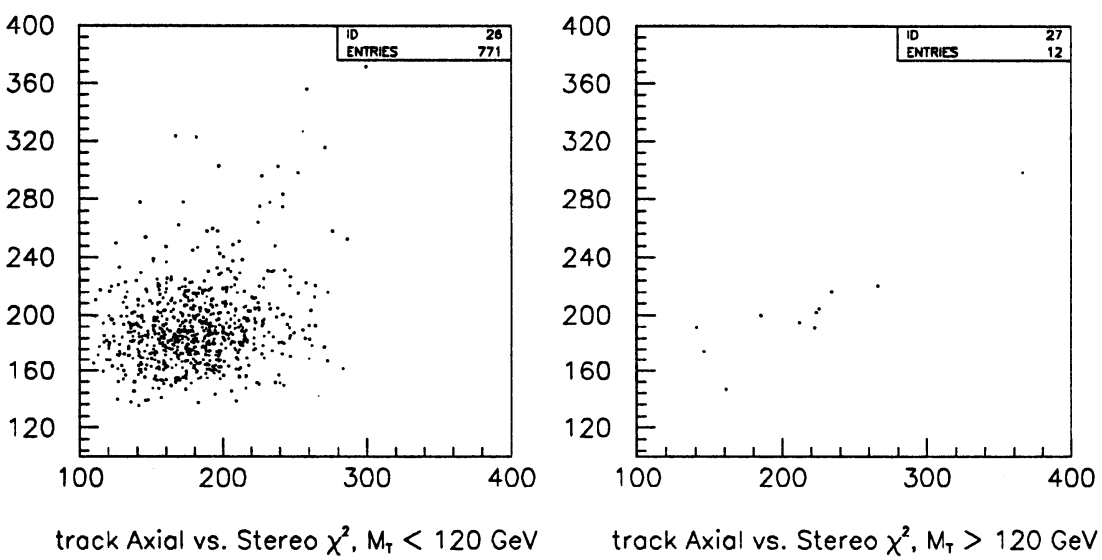


Figure 31. Axial vs. stereo $\chi^2$ for the muon track, for events with $M_T$ less than 120 GeV (left) and greater than 120 GeV (right).

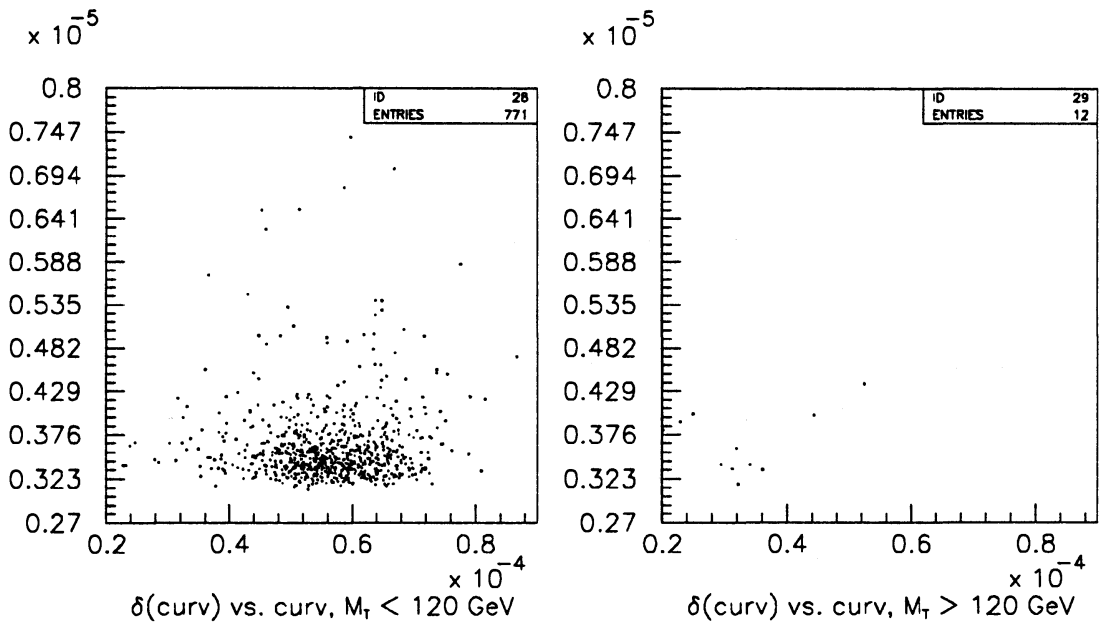


Figure 32. Curvature error (in $cm^{-1}$) calculated from the covariance matrix of the fitted track, vs. track curvature, for events with $M_T$ less than 120 GeV (left) and greater than 120 GeV (right).

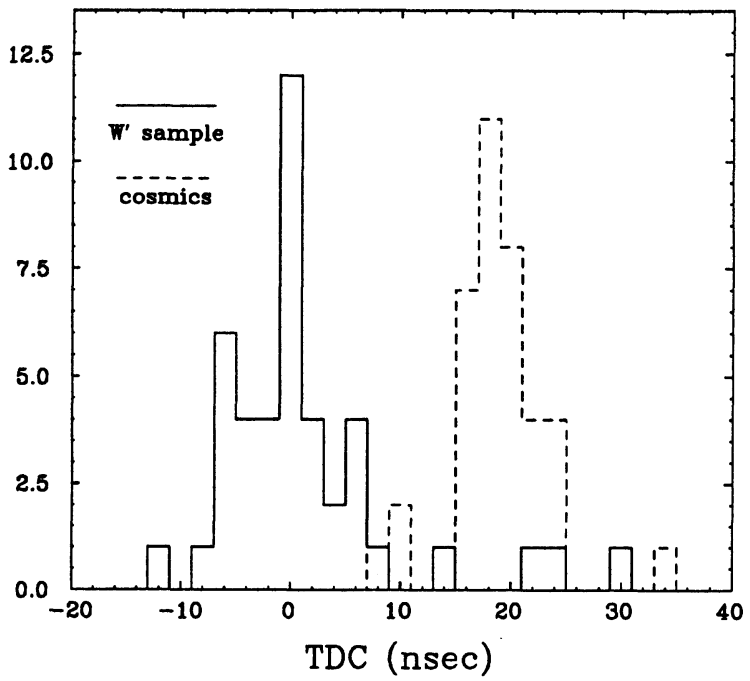


Figure 33. Time-of-flight measurements for muon candidate tracks, as determined from the hadron TDC's. The solid histogram is for muons in the $W' \rightarrow \mu\nu$ sample; the dashed histogram is for a sample of cosmic rays.

### *5.4.3 Cosmic Ray Background*

Cosmic rays were rejected by applying the cosmic ray filter to the muon candidate and to other isolated tracks in the event with $P_T > 10$ GeV. The filter does not use the information from the hadron TDC's. The TDC's can be used to calculate the time-of-flight *(tof)* of a track, which in turn can be used as the basis for an alternate cosmic ray filter. We have checked the time of flight between opposite ends of the muon track. Figure 33 shows the *tof* for all the events in the $W' \rightarrow \mu\nu$ sample (solid line) and for a sample of cosmic rays (dashed line). Two events fall in the *tof* cosmic ray window (17-27 ns): their transverse masses are 76 and 71 GeV. The visual scan for the high-$M_T$ events also rules out the residual cosmic ray hypothesis as improbable.

### 5.4.4 *Comparison with the $W' \rightarrow e\nu$ Sample*

The major difference between the electron and muon analyses is that in the former case the lepton energy is determined from the calorimeter (whose resolution improves with increasing energy) as well as from tracking (which has poorer resolution at high $P_T$), while for muons the energy must be inferred from tracking information alone.

To see if the events in the tail are due to the poorer resolution of tracking as opposed to calorimetry, we reanalyzed the electron sample, treating the electron as a muon: we beam constrained the electron track using the quantities in the QTRK bank, recalculated the $\not{E}_T$ ignoring the electron's calorimeter $E_T$ and correcting for the $P_T$ of the electron, and required the electron to point at the central muon fiducial region. We then formed the transverse mass from these quantities. The electron-neutrino $M_T$ "*à la* muon" is compared to the standard one in Figure 34. There is some indication that the resolution worsens when the transverse mass is derived from tracking information, with two events appearing at $M_T > 160$ GeV, but there is no change in the total number of events above 120 GeV.

The high-$M_T$ events are believed to come predominantly from high-$P_T$ $W$'s and are therefore often accompanied by jets. The distribution of the number of jets per event is comparable in the two samples, although the electron sample has slightly more no-jet events (63%, against 56% for the muons). The number of jets per event is shown in Figure 35. The top two plots show this distribution for the muon and electron samples (where the electron was selected as described above), and the bottom two plots show the number of jets in events with $M_T > 120$ GeV. Effects due to uncertainties in the jet energy measurement have been studied by comparing the lepton $P_T$ and the $P_T$ of the underlying event (the rest of the event, other than the primary lepton) for the muon and electron samples. These distributions are shown in Figures 36 and 37. While the underlying event distributions are in good

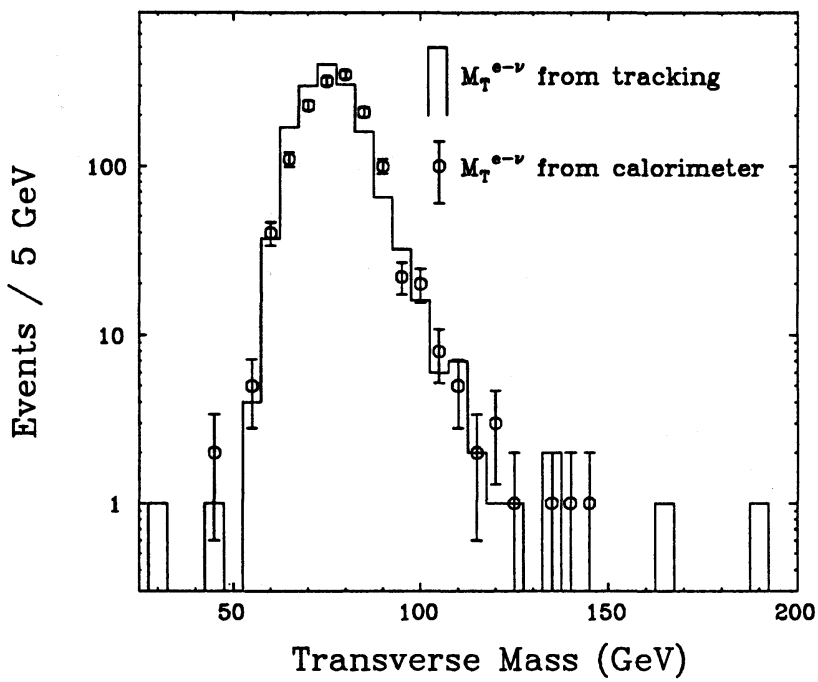


Figure 34. Comparison of electron-neutrino transverse mass derived from calorimeter information (circles) and from tracking information alone (histogram).

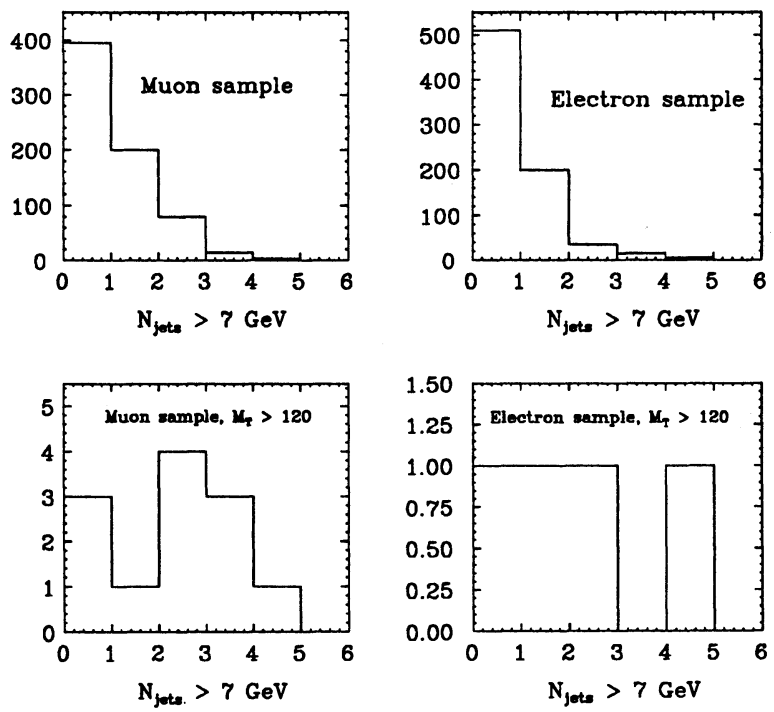


Figure 35. Number of jets per event in the muon and electron samples. The top two plots show the distributions for the whole samples, and the bottom two for events with $M_T > 120$ GeV.

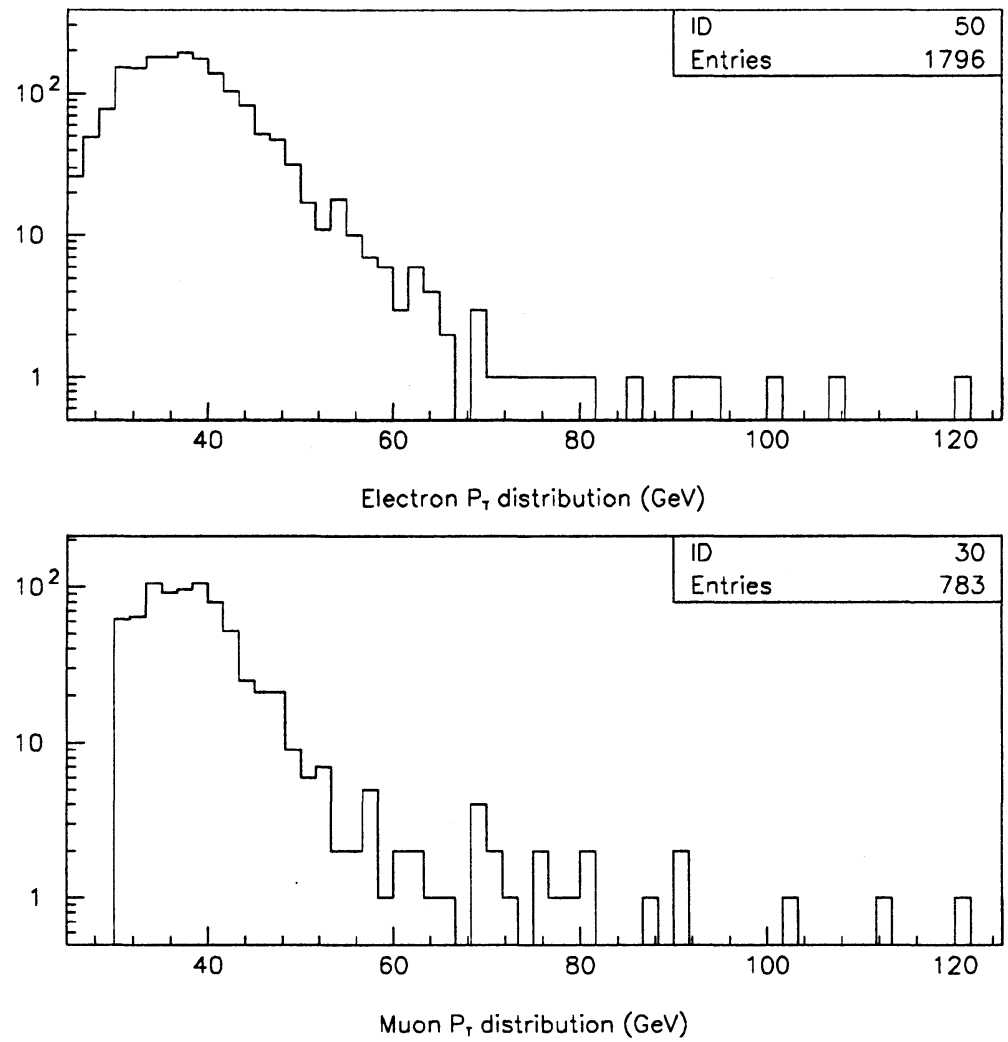


Figure 36. Lepton $P_T$ distributions for the electron sample (top) and muon sample (bottom). The muon sample shows a small excess of events at high $P_T$. Note that the electron sample is selected by requiring 30 GeV of calorimeter $E_T$, which explains why there are some events with $P_T < 30$ GeV in the sample.

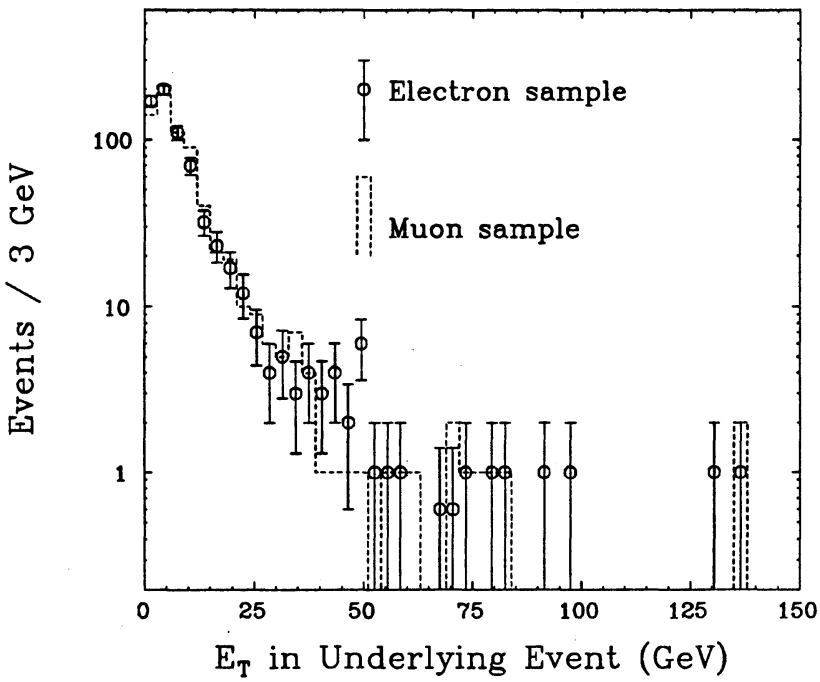


Figure 37. Distribution of $E_T$ in the underlying event, for the electron sample (circles) and muon sample (histogram).

agreement, the muon sample shows some excess of high-$P_T$ leptons, suggesting that if there is any problem it is connected to the muon and not to the global event topology.

One should note that the standard $W' \rightarrow e\nu$ sample has loose cuts on the electron. However, an $E_t$ and $\not{E}_T$ cut of 30 GeV was applied. To check that events in the tail had not been eliminated upstream in the electron analysis, an alternative electron sample, the so-called Electroweak spin sample, was also studied. Events were included in this sample if they satisfied:

- $(P_T^e > 7.5$ GeV) .OR. $(\frac{E}{P} < 2)$
- $(LSHR < .2\ )$ .OR. $(ISO < .1)$ (these are electron isolation cuts)
- $\frac{had}{em} < .055 + .045 \cdot \frac{E}{100}$

In addition a $P_T$ cut of 15 GeV was imposed. We checked that this sample was consistent with the standard $W \rightarrow e\nu$ sample, when the relevant cuts were applied.

These events were then required to satisfy all $W' \rightarrow \mu\nu$-type cuts, with the $E_T > 30$, $\not{E}_T$>30 GeV cuts applied to quantities calculated from track parameters. About 18% of the events fail the new cuts: this is consistent with the fact that electrons can lose some of their energy through bremsstrahlung, and consequently are measured with a momentum less than their "true" energy. However, a high-$M_T$ tail does not appear in this sample.

### *5.4.5 Residual Z Background*

Finally, we have checked that the events in the tail of the muon distribution do not contain a background from central–plug $Z$'s— $Z \rightarrow \mu\mu$ decays where one muon hits the central muon chambers and the other goes into the plug region, where CDF has no muon identification capability. The momentum carried by this muon would not be included in the calculation of the $\not{E}_T$, which consequently might appear to be

quite large. We generated a sample of $Z$'s with the program ZMONTECARLO[60], and simulated their behavior in the CDF detector using the same Monte Carlo described in Chapter 7 below. We required that one leg hit the CMU fiducial region and have $P_T > 30$ GeV; the other leg was required only to have $|\eta| > 1.1$ and was otherwise treated as a neutrino. We then imposed the $\not{E}_T > 30$ GeV cut and computed the resulting transverse mass spectrum, shown in the top portion of Figure 38. This spectrum actually peaks at quite low values of $M_T$, but this is not surprising because, with an energetic muon going so far forward, a good deal of the momentum flow in the event is longitudinal. As a result, very few misidentified central-plug $Z$'s are expected to fake a $W$ event with transverse mass above 120 GeV. Given the luminosity and acceptance, we expect roughly 0.1 such events in our sample.

We have also examined the possible background from central-central $Z$'s where the second leg is missed because it is buried in a jet. Again we simulated $Z$'s as $W$'s, requiring that the second leg fall in the central region but otherwise treating it as a neutrino for purposes of calculating the $\not{E}_T$ and transverse mass. The transverse mass distribution for this type of event is shown in the bottom half of Figure 38. Only 1–2 such events are expected to have a transverse mass above 120 GeV, but when this number is multiplied by the probability that the second leg would be buried in a jet, which we naively take to be 0.02 based on the efficiency of the $E_{cone}$ cut, this background is seen to be insignificant.

In short, we conclude that the events with transverse mass above 120 GeV contain good muons, and are unlikely to be background from non-electroweak sources.

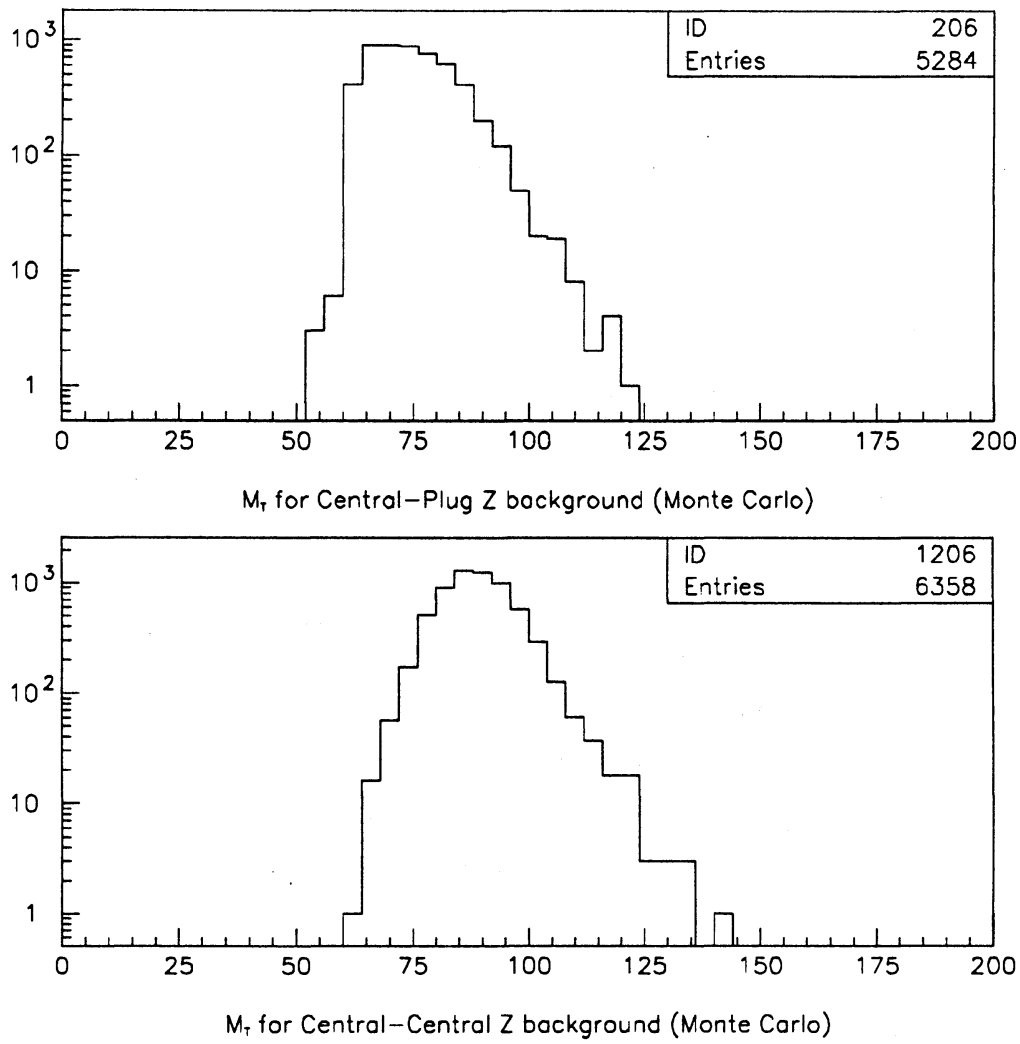


Figure 38. Monte Carlo transverse mass distributions (in GeV) for misidentified $Z \rightarrow \mu\mu$ events. Top: central–plug $Z$'s. Bottom: central–central $Z$'s. The shapes of these distributions indicate that this process does not constitute a significant background at high $M_T$.

# CHAPTER 6

# EFFICIENCIES

Never confuse efficiency with a liver complaint.
*Mary Poppins*

In the preceeding chapter we discussed the selection of the electron and muon samples. The selection was made with a set of cuts determined to be effective at removing background while keeping most of the signal, assumed to consist of high-$P_T$ electrons and muons. In this chapter we will make this statement more quantitative, by determining the efficiency of our electron and muon identification cuts. As indicated in Section 1.6, this number is an ingredient in the measurement of, or limit on, the $W'$ cross section.

That there is some inefficiency in our event selection is clear from the plots in Figures 17 and 19, in which almost every distribution has a tail extending beyond the point where our cut is made. The usual method for determining efficiencies is somehow to obtain an unbiased sample of good muons, say, and apply the same set of cuts to the unbiased sample. Ideally, one tries to to this directly from the data. Such an ideal turns out to be possible for most of the cuts used in this analysis. The kinematic cuts on $E_T$ (or $P_T$) and $\not{E}_T$ are considered part of the acceptance, which will be evaluated by Monte Carlo techniques in the next chapter.

## 6.1 Muon Selection Efficiencies

There are at least three sources of muons at CDF that are unbiased by trigger selection requirements: cosmic rays, and the decays $J/\psi \rightarrow \mu^+\mu^-$ and $Z \rightarrow \mu^+\mu^-$. A large sample of cosmic rays was collected during periods when the accelerator was off. This sample is especially useful for measuring the response of the calorimeters to minimum-ionizing particles. However, because the muons in cosmic rays sometimes move "backwards" through the detector (i.e from the outside in toward the interaction region), and arrive asynchronously (rather than in convenient multiples of 3.5 $\mu$sec), their track parameters may differ from those of the muons in our sample in ways that are hard to characterize. The cosmic ray sample is therefore unsuitable for studying tracking-dependent cuts at the few percent level. Muons from $J/\psi$'s and $Z$'s are much better for this purpose, but we need to explain how they can constitute an unbiased sample. The trick is to impose tight cuts on only one of the muon candidates in the event. We require that this "first muon" be the one to have fired the muon trigger, and ask that it pass a tight set of cuts similar to those described in the preceeding chapter. The "other muon," provided that it passes a very loose set of cuts and forms, together with the first muon, an object with the right invariant mass, can be considered unbiased. Furthermore, if the second muon also happens to pass the tight selection requirements, we can turn the argument around and consider the first muon unbiased. Note that, for this whole technique to work, the backgrounds underneath the $J/\psi$ and $Z$ mass peaks must be small, which in fact they are.

The $J/\psi$ and $Z$ samples are not without their drawbacks. Most of the $J/\psi$'s produced at CDF result from the decays of particles containing a $b$ quark. These particles are produced in pairs. and the other $b$ in the event often decays hadronically. Thus, $J/\psi$'s are often accompanied by jet activity, giving these events a different topology from most of the events in our sample. (As long as the muons themselves are isolated, this fact need not pose problems.) Also, the muons from $J/\psi$ decay

usually have a $P_T$ less than 15 GeV, so that the effects of multiple scattering are more important than for the high-$P_T$ muons of interest in the $W'$ search. Of the three unbiased muon sources we have mentioned, $Z$'s constitute the best since the muons are of the right $P_T$ and the production process is similar to that of $W$'s or $W'$'s. The main problem with $Z$'s is poor statistics. Nonetheless, we have used $Z$'s whenever possible.

A sample of $Z \rightarrow \mu^+\mu^-$ events is selected by requiring at least one muon with $P_T > 20$ GeV to pass the muon quality cuts used in the $W'$ sample. Then, a second track in the event is required to satisfy the following loose set of cuts:

- $P_T > 20$ GeV (beam-constrained $P_T$ if available)
- $E_T < 5$ GeV in a cone of size 0.4 (in $\eta$-$\phi$ space) centered on the muon, and excluding the energy in the tower traversed by the muon. We call this the $E_{cone}$ cut.
- $|\eta|_{track} < 1.1$ at the radius of the muon chambers
- Invariant mass with the first muon between 65 and 115 GeV (compare to the $Z$ mass of 91 GeV).

Essentially all we require here is an isolated, high-$P_T$ track in the $Z$ mass window. Note that we do not require the second track to hit the central muon chambers. This requirement is not necessary for the study of such cuts as HAD, EM, and impact parameter cuts. There are 32 events in which both muons hit the CMU, and an additional 66 events with only one central muon plus a track. Of the 32 "other muons" that hit the muon chambers, some 26 of these also pass the tight selection criteria, giving a total of $66 + 32 + 26 = 124$ unbiased muons with which to study efficiencies. There are no same-sign pairs in this sample. which indicates that it is background-free. (One would expect same-sign and opposite-sign background events in equal numbers.) The dimuon invariant mass distribution for these events is shown in Fig 39.

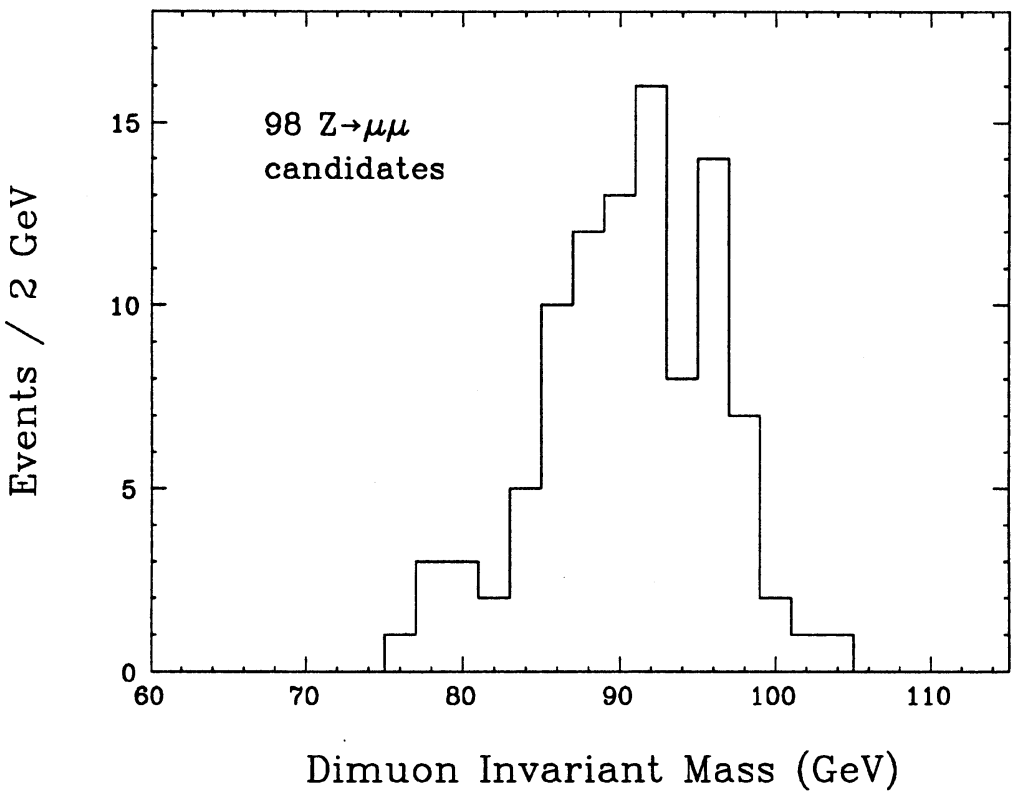


Figure 39. Dimuon invariant mass distribution for the $Z \rightarrow \mu^+\mu^-$ sample used to determine the muon identification efficiencies.

Table 1. Efficiencies of cuts used in the $W' \rightarrow \mu\nu$ sample

| cut | $N_{tot}$ | $N_{pass}$ | $\epsilon$ (%) |
|---|---|---|---|
| EM $< 2$ GeV | 124 | 122 | $98.4^{+1.1}_{-2.1}$ |
| HAD $< 6$ GeV | 124 | 120 | $96.8^{+1.5}_{-2.5}$ |
| $\lvert impact \rvert < 0.15$ cm | 124 | 122 | $98.4^{+1.1}_{-2.1}$ |
| $\lvert \Delta x \rvert < 2$ cm | 58 | 55 | $94.8^{+2.8}_{-4.8}$ |
| $\lvert \Delta z \rvert < 15$ cm | 58 | 58 | $100^{+0}_{-3.1}$ |
| beam constrainable | 124 | 124 | $100^{+0}_{-1.5}$ |
| track quality | 124 | 124 | $100^{+0}_{-1.5}$ |
| $E_{cone} < 5$ GeV | 3550 | 3513 | $99.0 \pm 0.2$ |
| Tracking efficiency | 237 | 234 | $99 \pm 1$ |
| cosmic filter | — | — | $99.7 \pm 0.3$ |
| $\lvert z_{vtx} \rvert < 60$ cm | — | — | $95 \pm 1$ |
| TOTAL | | | $76 \pm 6.0$ |

We determine the efficiencies of the individual cuts by applying the tight cuts to the muons in this sample. The distributions of some of the cut variables for these muons are shown in Figure 40. (Not shown in these plots are the distributions for the first muon in the 26 events where both muons passed all the cuts.) All of the muons in the sample passed the beam constraint requirement and the low-level track quality requirements. The efficiencies are given in Table 1.

The efficiencies obtained in this way are efficiencies for isolated muons, since the second legs were selected using the $E_{cone}$ cut. A different method is required to determine the efficiency of the $E_{cone}$ cut itself. We choose to throw random cones of size 0.4 (in $\eta$-$\phi$ space), with the inner tower removed, onto the events in the $W' \rightarrow \mu\nu$ sample. Five cones per event were thrown in the region $|\eta| < 0.8$, $0 < \phi \leq 2\pi$, but

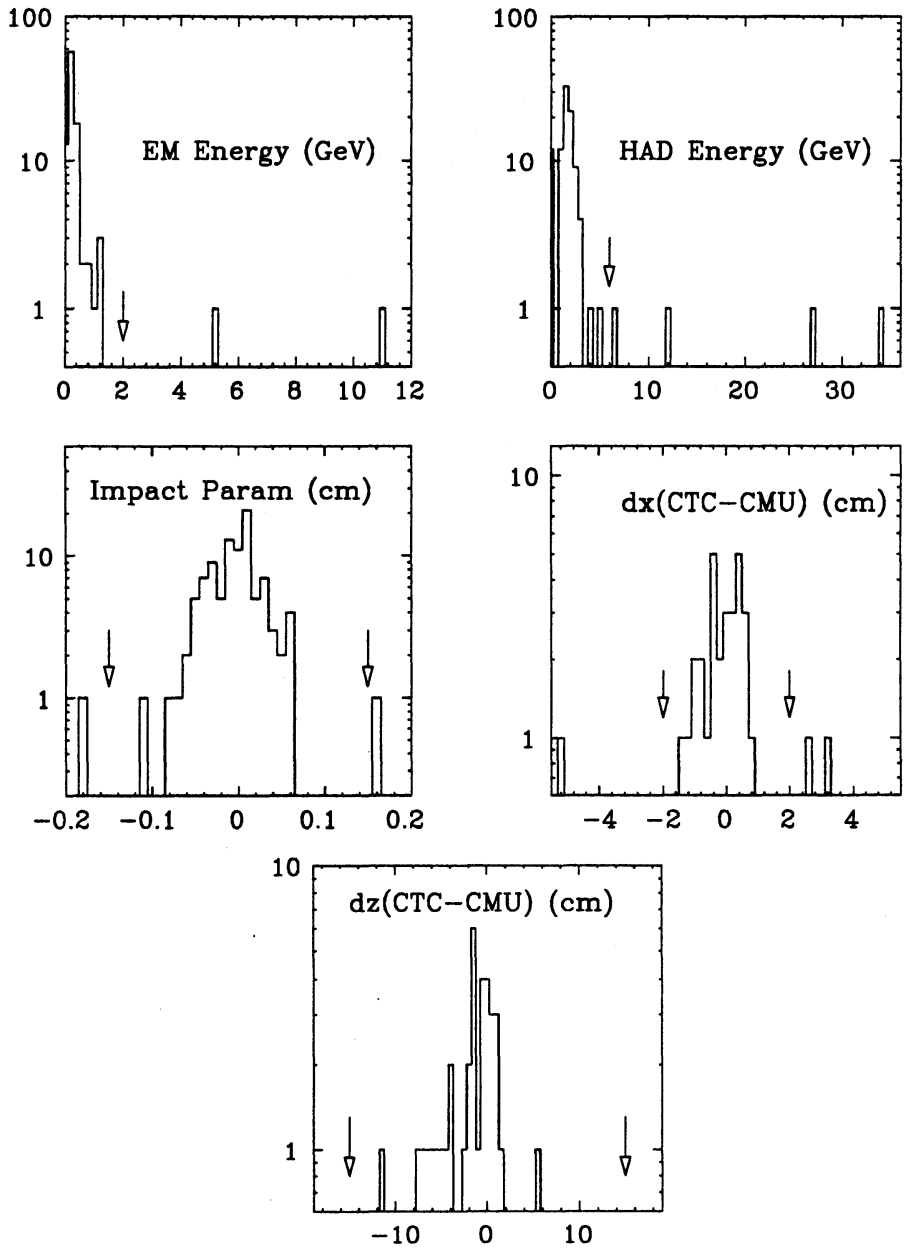


Figure 40. Distributions of the cut variables for muons in the efficiency sample.

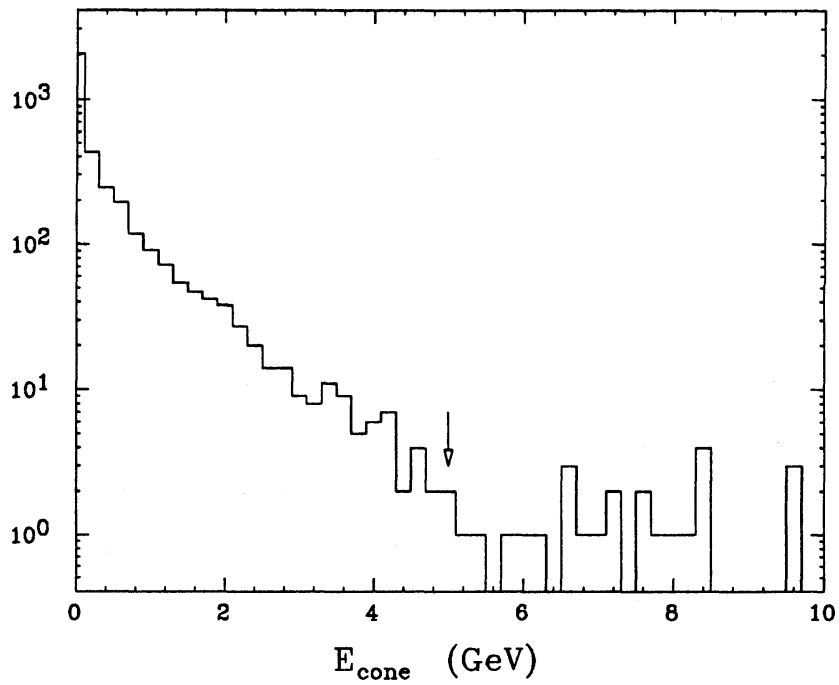


Figure 41. Energy in random cones for events in the $W' \rightarrow \mu\nu$ sample.

not on top of the muon or back-to-back to it. In this way we learn the probability that a good muon would fail the $E_{cone}$ cut because it happened to overlap with an unrelated piece of the underlying event. We find that of 3550 random cones, 37 had more than 5 GeV of $E_T$. The distribution of $E_{cone}$ in these random cones is shown in Figure 41. From this we find

$$\epsilon_{E_{cone}<5} = 99.0 \pm 0.2.$$

The efficiencies of the calorimeter energy cuts HAD < 6 GeV and EM < 2 GeV have also been studied from $J/\psi$ and cosmic ray samples[61]. The combined efficiency measured for these cuts, $98.8 \pm 0.2 \pm 0.2\%$, is consistent with the number obtained from the $Z$'s, although because of the much larger statistics in these samples the error is smaller.

Other efficiencies are known from separate sources. The cosmic filter was determined by eye-scanning[59] to be 99.8% efficient for real $W$ and $Z$ events. As a cross-

check, the filter was applied to a standard $W \rightarrow e\nu$ data sample[62]. Of 1525 events in which the electron was in the central muon fiducial region, had $P_T > 15$ GeV, and passed the muon track quality requirements, three were misidentified as cosmic rays, consistent with the number expected based on the scan.

The cosmic filter contains an event vertex cut $|z_{vtx}| < 60$ cm. The efficiency of the vertex cut is $95 \pm 1\%$, based on the measured width of the vertex distribution, $\sigma_{z_{vtx}} = 30 \pm 2$ cm.

Recall from Chapter 5 that the large sample of central muon candidates was retracked using a new pattern-recognition and fitting algorithm before the final event selection was made. It is possible to lose good tracks due to inefficiencies in this algorithm. We have estimated[50] this inefficiency by retracking a standard sample of $Z \rightarrow e^+e^-$ events. Out of 237 electrons which had tracks in this sample, 3 were lost on retracking, giving a tracking efficiency of $99 \pm 1\%$.

Finally, the level 2 central muon trigger was determined[52] to have an efficiency of $97.2^{+1.5}_{-2.7}\%$. But this trigger requires a level 1 trigger, so it is the combined L1–L2 efficiency that is relevant. This efficiency was determined[49, 50] to be

$$\epsilon_{trigger} = 91 \pm 2\%.$$

The most naive way to determine the overall efficiency is then to multiply all the efficiencies together and add the errors in quadrature. Excluding the vertex and trigger efficiencies, this method yields $\epsilon_{mult} = 87.1 \pm 5.2\%$. With the vertex cut and trigger efficiency included, we find

$$\epsilon_{mult,tot} = 75.5 \pm 5.7\%.$$

We obtain a separate estimate of the efficiency by noting that 26 of 32 second muons in our $Z$ sample pass all the tight cuts, giving a total of 52 out of 58 unbiased central muons that passed all the cuts. We then lower this number by the efficiencies of the $E_{cone}$, cosmic, and trigger cuts on which these events were selected. We find

$$\epsilon_{combined} = 76.6 \pm 5.3\%$$

Happily, these two methods yield consistent results, and the discrepancy occurs with the correct sign. (If some cuts are correlated, as, for example, the calorimeter energy cuts HAD and EM probably are, then multiplying the individual efficiencies leads to an underestimate of the true efficiency.) In view of this essential agreement, we have chosen a compromise and take

$$\epsilon_{overall} = 76 \pm 6\%$$

for the muon selection efficiency in the $W' \rightarrow \mu\nu$ analysis.

This efficiency is expected to remain constant as a function of the muon's $P_T$, for $P_T > 15$ GeV. Muons of the energies we consider here do not undergo significant bremsstrahlung, and all are well into the region where they behave as minimum-ionizing particles. If anything, the efficiency of the track matching cut $dx < 2$ cm and the impact parameter cut may improve slightly with $P_T$, as the effects of multiple scattering become even smaller. It is a safe and conservative assumption, however, to assume that the efficiency simply remains constant.

## 6.2 Electron Selection Efficiencies

We now turn to the evaluation of the electron identification efficiencies. In contrast to the muon case, we must now consider the dependence of certain efficiencies on the electron $E_T$. A dependence on $E_T$ arises because of two effects. The first is that electrons with higher energies will undergo greater bremsstrahlung. This effect in turn can affect the efficiencies of the cuts on $E/P$ and the border tower energy. The $E/P$ efficiency can be lowered because, when the electron radiates an energetic photon, the momentum of the observed charged track is correspondingly reduced. But if the photon goes into the same calorimeter tower as the electron, the measured energy is that of the original electron before it radiated. Consequently a tail can appear in the high end of the $E/P$ distribution and reduce the efficiency of our cut. On the other hand, if the radiated photon does not enter the same calorimeter

tower as the electron but rather one of the adjacent ones, the electron can appear non-isolated and may fail the cut on the border tower energy. The border tower efficiency can also be lowered by the increased lateral size of the electromagnetic shower. Another effect that can lower our efficiency is the increased depth of the electromagnetic shower for high-$E_T$ electrons. The showers of very energetic electrons may not be fully contained in the electromagnetic calorimeter, but can leak through it into the hadronic calorimeter, thereby lowering the efficiency of the cut on the ratio of hadronic to electromagnetic energy, HAD/EM.

### *6.2.1 Efficiencies Independent of $E_T$*

Nonetheless, several of our cuts are not expected to depend significantly on $E_T$. The cut on the location of the primary event vertex, $|z_{vtx}| < 60$ cm, is $95 \pm 1\%$ efficient, based on the measured gaussian width of the event vertex distribution of $30 \pm 2$ cm. Also constant are the efficiencies of the cuts on the extrapolated position of the track at the radius of the strip chambers, relative to the observed position in these chambers of the electromagnetic shower. The efficiencies of these cuts were evaluated in ref. [53] using an unbiased sample of electrons from $Z$'s, as well as electrons from $W$'s that were selected with a missing-$E_T$ trigger. (No such sample is available for the $W' \rightarrow \mu\nu$ analysis, because the missing-$E_T$ trigger is based on an imbalance in calorimeter energy and is not sensitive to the minimum-ionizing muon.) The cuts on the track-to-shower match in the $z$ and $r$-$\phi$ views were determined to be $100^{+0}_{-1}\%$ and $99 \pm 1\%$ efficient, respectively. Finally, the filter we apply to reject conversions can reject primary electrons as well. This filter was measured[63] to be $95 \pm 2\%$ efficient for such electrons.

### *6.2.2 Efficiencies Dependent on $E_T$*

**HAD/EM Efficiency** The efficiency loss of the HAD/EM cut has been studied using data collected at the CDF testbeam facility. Wedges from the central calorimeter were placed in beams of known energy and composition, and their responses evaluated. Electron data from the testbeam is available out to energies of 150 GeV (such as would result from the decay of a 300–400 GeV $W'$). For energies beyond this an extrapolation is necessary. A fit to the data gives[64]

$$\epsilon_{\mathrm{HAD/EM}<0.1} = 1.0 - 1.22e^{-556/E} \pm 0.01,$$

where the electron energy $E$ is measured in GeV. Thus this cut is essentially 100% efficient for the electrons typical of $W$ decay (a number in agreement with the collider data), while for 200 GeV electrons the efficiency drops to 92.4%.

**E/P Efficiency** The efficiency of the $E/P$ cut was studied with a radiative Monte Carlo program that included the effects of initial- and final-state radiation in $W$ and $W'$ production. The events generated by this program were then passed through a full detector simulation that included the effects of bremsstrahlung. That this program accurately reproduces the behavior of real electrons in the detector is shown in Figure 42, taken from ref. [35]. $E/P$ distributions were then generated for electrons from $W'$'s of mass 125, 200, 350, and 500 GeV. These distributions are shown in Figure 43. The broadening of the tail toward the high-$E/P$ end is evident, although the cut $E/P < 2$ remains highly efficient. From a fit to these calculated efficiencies, we obtain the curve shown in Figure 44, showing the efficiency of our $E/P$ cut as a function of $M_{W'}$. We assign a generous 1.5% uncertainty to these numbers.

**Border Tower Efficiency** The efficiency of the cut on the border tower energy was studied using the same radiative Monte Carlo program and detector

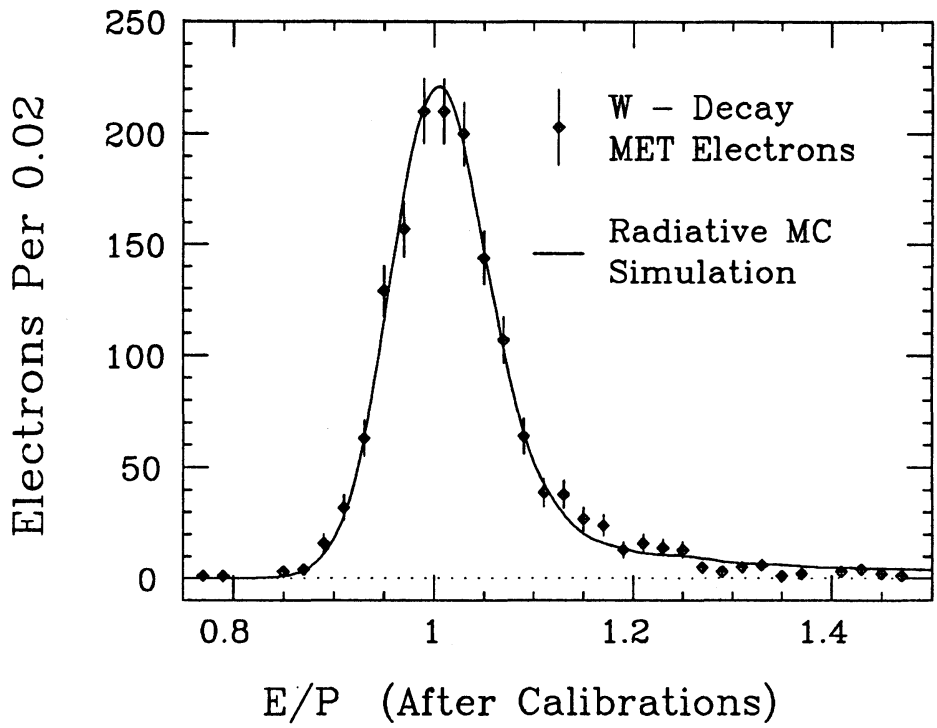


Figure 42. $E/P$ distributions for electrons from $W$ decay, selected using a missing-$E_T$ trigger. Superimposed is a prediction from the radiative Monte Carlo program described in the text.

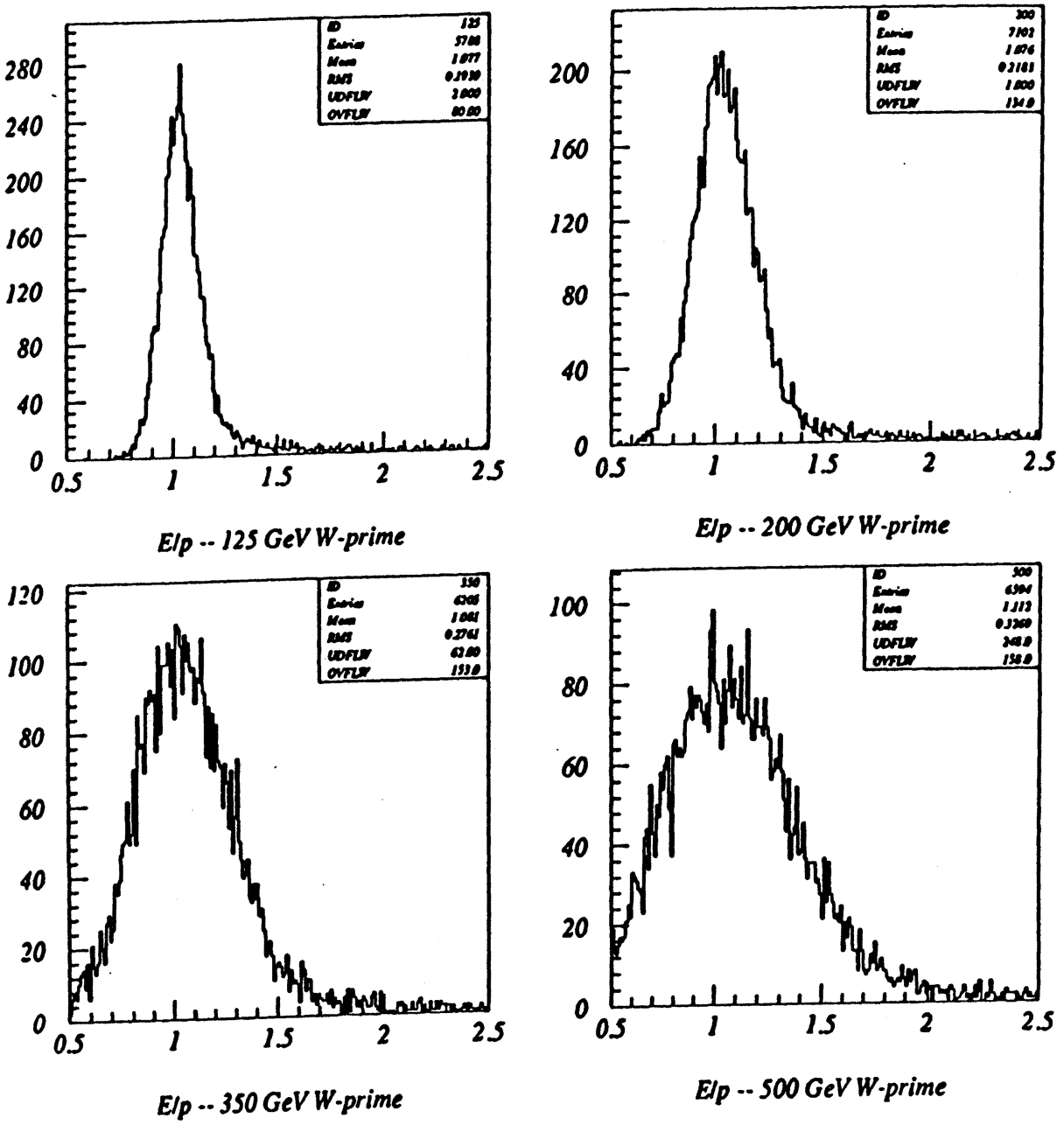


Figure 43. $E/P$ distributions for $W'$'s of mass 125, 200, 350, and 500 GeV, as determined from the radiative Monte Carlo.

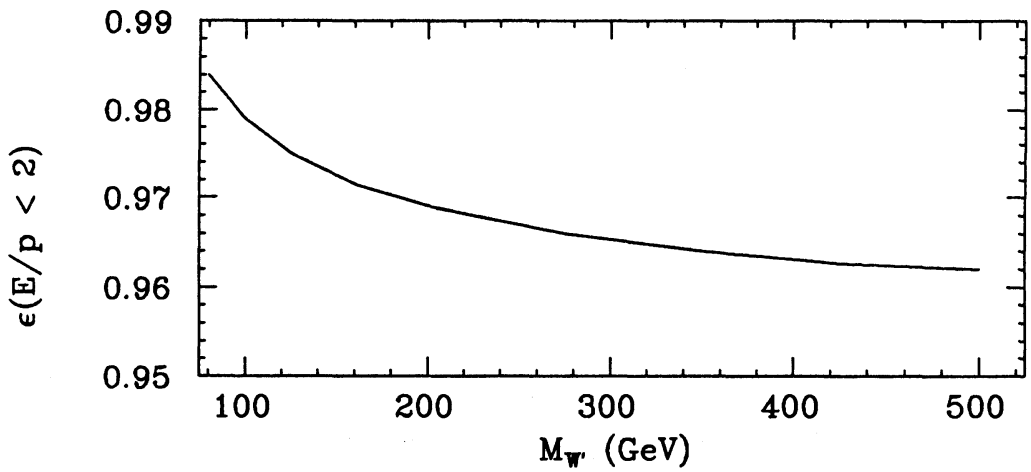


Figure 44. Efficiency of the $E/P$ cut versus $W'$ mass.

simulation described above. Plots of the border tower energy for $W'$'s of mass 125, 200, 350, and 500 GeV are shown in Figure 45. The corresponding efficiency of the cut at 5 GeV is well-described by the line shown in Figure 46. We have included in the inefficiency a 1% contribution from the underlying event, which is not modeled in the Monte Carlo. We again assign a 1.5% uncertainty to the curve in the figure.

The efficiency of the electron identification cuts is summarized in Table 2.

The overall electron identification efficiency is given by multiplying the individual efficiencies together. (The correlations between these cuts are smaller than the error bars we have assigned, and an any case a straightforward multiplication is the most conservative thing to do.) The overall efficiency varies with $M_{W'}$ from $84.5 \pm 3.5\%$ at the $W$ mass to $70.5 \pm 3.5\%$ for a 500 GeV $W'$, where we have included the trigger efficiency of $97.3 \pm 0.5\%$ in the final numbers.

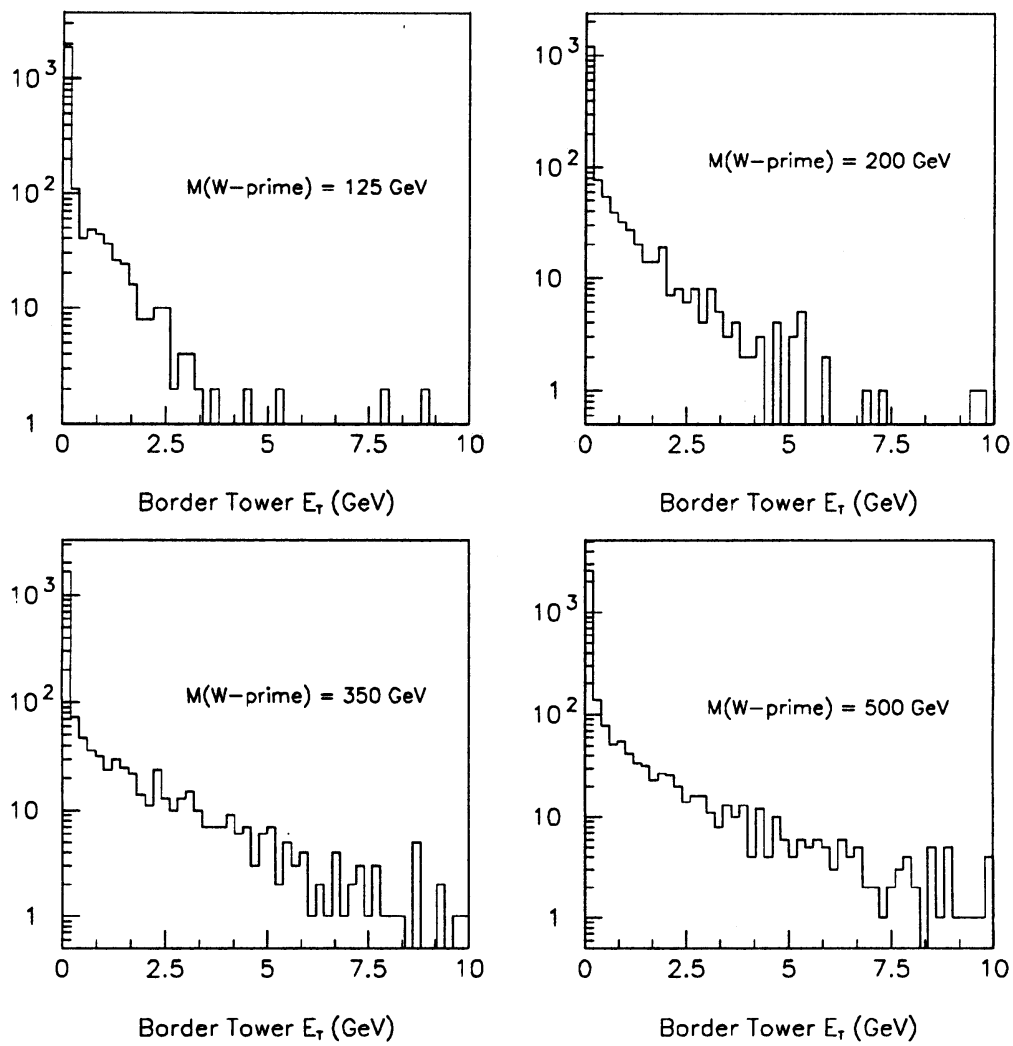


Figure 45. Border tower energy distributions for $W'$'s of mass 125, 200, 350, and 500 GeV, as determined from the radiative Monte Carlo.

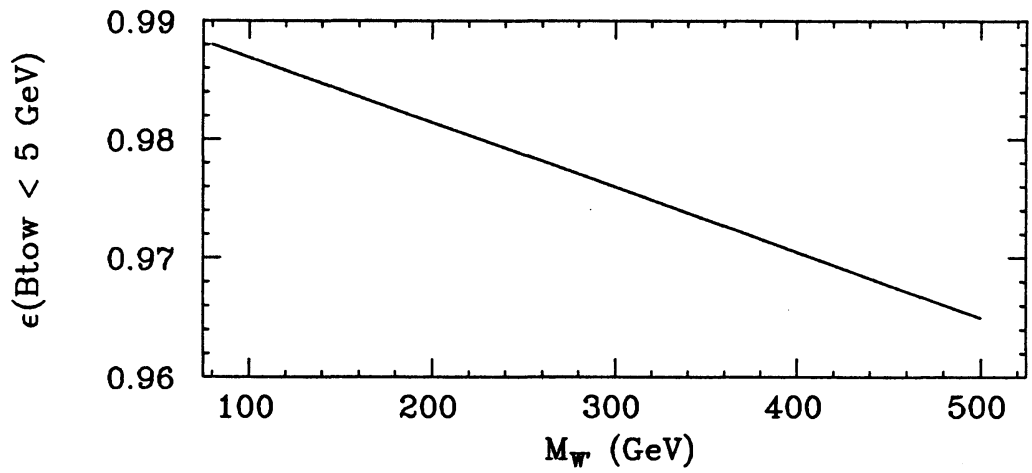


Figure 46. Efficiency of the border tower energy cut versus $W'$ mass.

Table 2. Efficiencies of cuts used in the $W' \to e\nu$ sample

| cut | $\epsilon$ (%) |
|---|---|
| $\lvert\Delta(r-\phi)(\mathrm{CTC}-\mathrm{CES})\rvert < 1.5$ cm | $99^{+1.0}_{-1.0}$ |
| $\lvert\Delta z(\mathrm{CTC}-\mathrm{CES})\rvert < 3$ cm | $100^{+0}_{-1.0}$ |
| HAD/EM $< 0.1$ | $100 - 122e^{-556/E} \pm 1.0$ |
| $E/P < 2$ | $\simeq 97 \pm 1.5$ |
| BrdrTower $E_T < 5$ GeV | $\simeq 98 \pm 1.5$ |
| $\lvert z_{vtx}\rvert < 60$ cm | $95 \pm 1$ |

# CHAPTER 7

# MONTE CARLO

In preceding chapters we have discussed the selection of the electron and muon samples, and have evaluated the efficiency of the lepton quality cuts used in this selection. By knowing the integrated luminosity $\mathcal{L}$ of the two datasets, as well as the efficiencies, we have in hand two of the numbers that we need to measure or set a limit on the $W'$ cross section times leptonic branching ratio. We need additional information to extract the $W'$ cross section, however. In this chapter we describe the Monte Carlo program used to determine the kinematic acceptance $A$ for $W'$'s of various masses, and for $W$ bosons. The Monte Carlo is also used to determine the shape of the transverse mass distributions arising from $W'$'s and $W$'s and is therefore an ingredient in the likelihood fit that allows us to determine how many events in our sample can be attributed to particles of each type.

These are fairly simple questions to ask of a Monte Carlo. It is therefore possible to employ a simple, "home-brew" Monte Carlo[60], rather than one of the more sophisticated, general-purpose event generators commonly used in high-energy physics. In addition, a simple simulation of the CDF detector was used in place of the cpu-intensive simulations that provide a level of detail unnecessary for this analysis. By using a simple Monte Carlo with just a few adjustable parameters, it is possible to

generate tens of thousands of events very quickly. Because the number of adjustable parameters is small, it is easy to estimate the systematic uncertainties.

## 7.1 Event Generation

$W$ and $W'$ events were generated according to the leading-order Drell-Yan process described in Chapter 1. The cross section for this process, in which a quark and an antiquark annihilate to form a charged boson, is

$$\hat{\sigma}(q\bar{q}' \rightarrow W'^{+}) = 2\pi |U_{q\bar{q}'}|^2 \frac{G_F}{\sqrt{2}} \frac{M_W^2}{M_{W'}^2},$$

where we have assumed standard-strength couplings. To account for higher-order QCD effects, we multiply this cross section by a $K$-factor,

$$K = 1 + \frac{8\pi}{9}\alpha_s(Q^2 = M_{W'}^2).$$

The strong coupling constant $\alpha_s$ runs logarithmically with $Q^2$, and the $K$-factor effectively increases the cross section by approximately 30% over its leading-order value.

The cross section for the hard subprocess is then folded into the proton structure functions to obtain the total cross section $\sigma(p\bar{p} \rightarrow W')$. We have chosen the HMRS(B) structure functions[16], as these are up-to-date and give a predicted cross section that falls near the middle of the range predicted by other contemporary structure function sets.

We wish to know the $W'$ cross sections for standard-strength couplings because they allow us to convert a measured limit on the $W'$ cross section into a limit on the $W'$ mass itself. The cross sections, as calculated by this Monte Carlo, were shown in Chapter 1, Figure 2. Besides giving us the cross sections, however, the Monte Carlo also provides us with the angular distributions of the leptons from the decay of the $W'$. The next step is to pass the particles through a simulation of the CDF

detector, to determine the kinematic and geometrical acceptance for the leptons, and to calculate the shape of the transverse mass distributions.

## 7.2 Detector Simulation

After event generation, a second program[60] is used to model the features of the CDF detector relevant to this analysis, as well as some features of $W$ and $W'$ production not accounted for in the event generator. These features include the gaussian distribution in $z$ of the event vertex, the transverse momentum distribution of the bosons, resolution of the energy or momentum measurement of the charged lepton, and the uncertainties on the measurement of the remaining particles in the event, also called the underlying event.

### *7.2.1 $P_T$ Distributions*

The event generator described above contains only the lowest-order diagram (with a $K$-factor) for $W$ and $W'$ production. It does not, therefore, supply the bosons with a $P_T$ distribution. Instead, we put in a distribution by hand. For the $W$'s, one has two choices: one could either use a $P_T$ distribution derived from the data, or use the results of a theoretical calculation. In the former case, the observed $P_T$ distribution must be corrected for the kinematic acceptance before running the Monte Carlo, which is a rather difficult job[65]. Because of this fact, and because one is compelled in any case to use a calculation for the $P_T$ of the $W'$'s, we have chosen to use the $W$ $P_T$ distribution calculated by Arnold and collaborators[66, 67]. They obtained this distribution by merging two calculations, each with its own range of validity: a next-to-leading-order QCD calculation, which is valid for higher-$P_T$ bosons ($P_T > M/4$), and a nonperturbative calculation based on gluon resummation techniques, which handles the low-$P_T$ end of the spectrum. This distribution is in good agreement with data from CDF[65], particularly at the high-$P_T$ end that is of

the most interest in this analysis. (Recall from Chapter 5 that $W$'s with high $P_T$ are the most likely to be measured with a large transverse mass, and thus constitute the greatest source of background to a $W'$ search.) The agreement between the $W$ $P_T$ data and the QCD prediction is shown in Figure 47.

For the $W'$ $P_T$ distributions, we have used the results of a calculation made available to us by Peter Arnold[68]. The calculation was performed with the same program used to calculate the $W$ $P_T$ distribution in ref. [67]. The $W$ mass was varied from 80 to 200 GeV and the gauge couplings were held constant, thus reproducing the case of a $W'$ with standard couplings. In all cases, the HMRS(B) structure functions were used, and $\Lambda^{(4)}_{QCD}$ was taken to be 190 MeV. Arnold estimates the relative error in the calculation to be about 15% for values of $P_T$ down to $M_{W'}/8$, and up to 30% for lower values of $P_T$.

The $P_T$ distributions for $W$ and $W'$ bosons of various masses are shown in Figure 48. As is evident from the figure, the $P_T$ distribution for $W'$'s is only slightly harder than that of $W$'s, and is a very slowly varying function of $M_{W'}$. For this reason, we have simply used the distribution for a 200 GeV $W'$ in our simulation for all values of $M_{W'}$ greater than 200 GeV.

### *7.2.2 Lepton Smearing*

The momentum of charged leptons ($e$ or $\mu$) from $W$ or $W'$ decay is smeared according to the measured resolution of the CDF detector. The electron portion of this analysis makes use of the central electromagnetic calorimeter, which has an energy resolution of

$$\frac{\sigma_{E_T}}{E_T} = \frac{13.5\%}{\sqrt{E_T}} \oplus 2.0\%,$$

where $E_T$ is measured in GeV and the $\oplus$ indicates that the terms are to be added in quadrature. We therefore smear each generated electron by a random amount

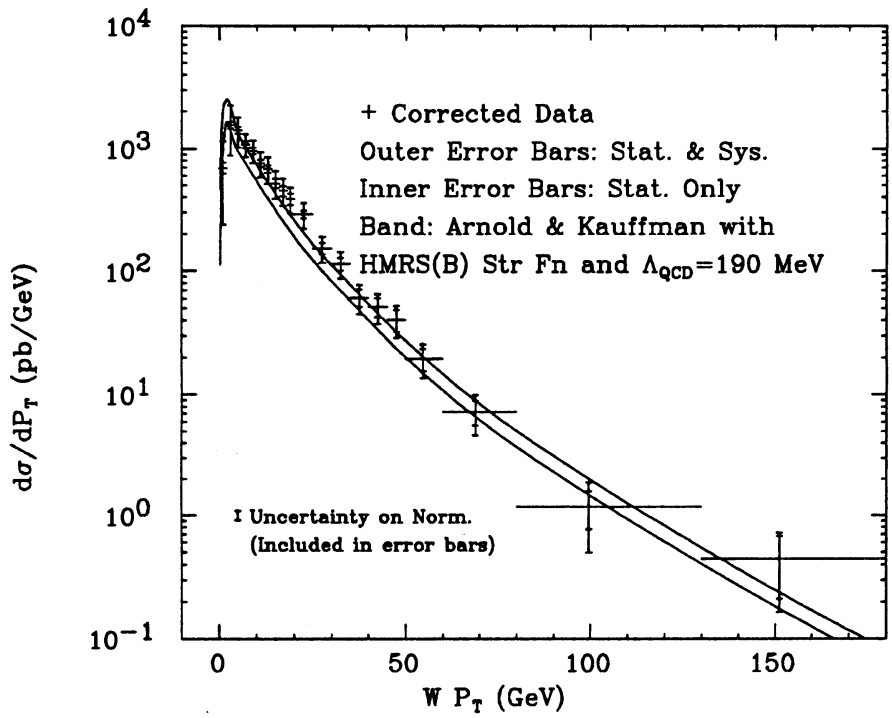


Figure 47. Measured $W$ boson $P_T$ distribution at CDF, together with the QCD prediction from ref. [67].

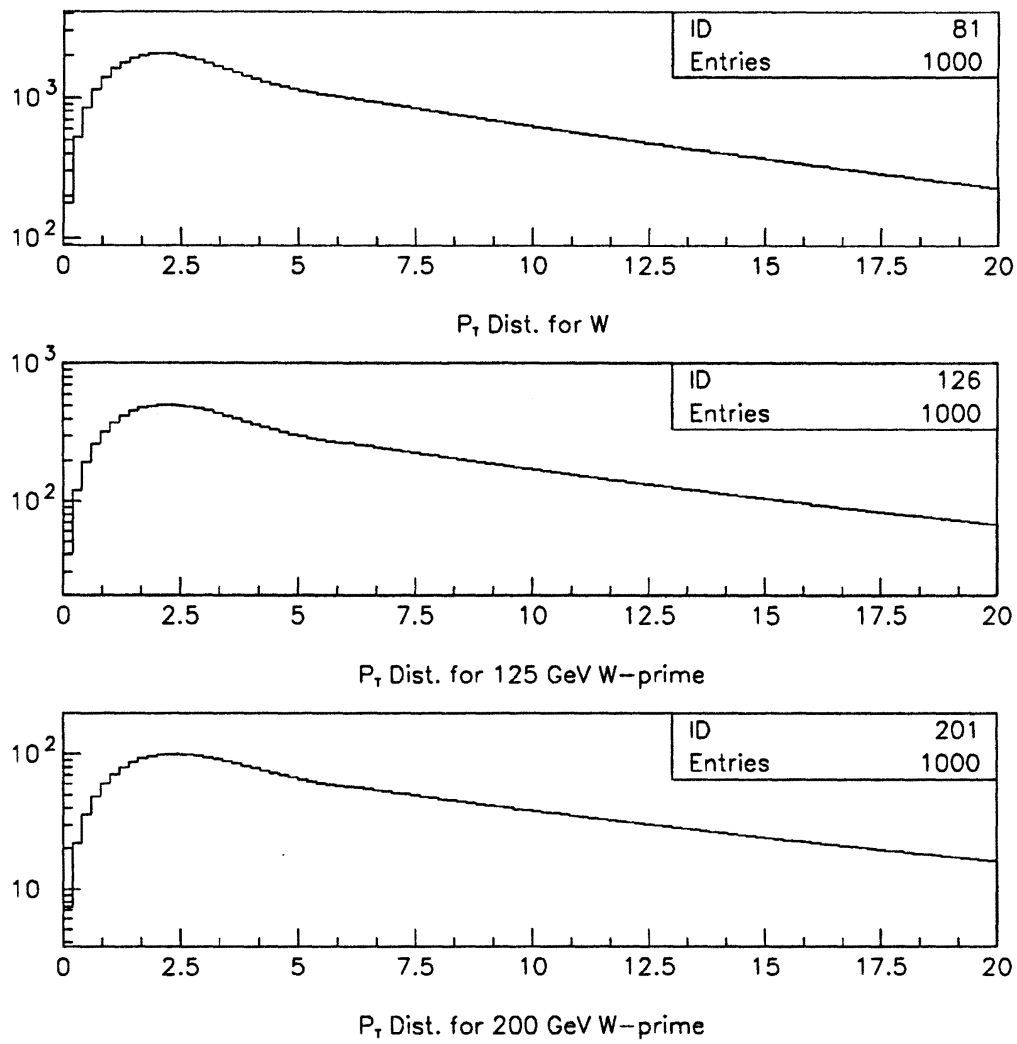


Figure 48. $P_T$ distributions for $W$ (top), 125 GeV $W'$ (middle), and 200 GeV $W'$ bosons (bottom), as calculated by P. Arnold. The $x$-axis is the $P_T$ of the boson in GeV.

taken from this distribution. Note that the relative error decreases with increasing $E_T$.

For muons, we measure the momentum, not the energy. The resolution of the central tracking chamber is

$$\frac{\sigma_{P_T}}{P_T} = 0.11\% P_T.$$

Again, $P_T$ is measured in GeV. This resolution is obtained by using a beam-constraint—that is, the observed position of the event vertex is used as an additional point in the fit. The relative error increases with $P_T$, opposite to the case for electrons. The electron and muon resolutions are comparable for leptons typical of $W$ decays, but the muon resolution worsens rapidly for higher-$P_T$ muons. This is one reason that the electron channel is more powerful for the $W'$ search.

Actually, this formula for the resolution of the central tracking chamber, often given in other CDF publications, is only approximately correct. In fact, the CTC measures the track's curvature, which is proportional to $1/P_T$. It is the curvature that has a gaussian distribution. We therefore smear the curvature of the generated muon tracks with a gaussian of width 0.0011.

### *7.2.3 The Underlying Event*

A $W$ or $W'$ produced in a hadron collision usually possesses some transverse momentum $P_T$. Because the transverse momentum of the system before the collision was zero, the $P_T$ of the boson must be balanced by a collection of recoiling particles, termed the underlying event, which may include fragments of the spectator partons, other miscellaneous hadrons, and possibly jets. These particles go into the detector and contribute to our measurement of the magnitude and direction of the missing $E_T$, which in turn are quantities used to form the transverse mass. Because it is the transverse mass spectrum that we wish to study for indications of a $W'$, we

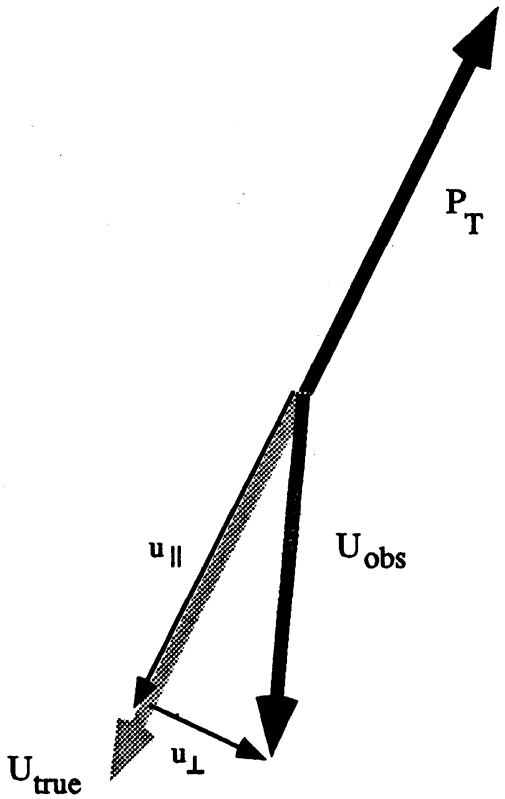


Figure 49. Decomposition of the observed underlying event vector into components $u_{||}$ and $u_{\perp}$ along the direction of the true underlying event vector. The true underlying event vector is equal in magnitude and opposite in direction to the $P_T$ of the boson.

have taken care to include a realistic parametrization of the underlying event in our Monte Carlo.

The parametrization was obtained from the results of a more detailed simulation. We began with 4000 $W$ events made by the Isajet[69] event generator, and simulated using the full detector simulation package CDFSIM. With these events, we could study the "observed" underlying event vector $\mathbf{u}$ as a function of the "true" $P_T$. (In an ideal detector, $\mathbf{u} = -\mathbf{P}_T$.) We break the observed underlying event vector into components parallel and perpendicular to the true underlying event direction. We call these components $u_{||}$ and $u_{\perp}$. The relationship between these vectors is shown in Figure 49.

The parallel and perpendicular components of $\mathbf{u}$, measured with respect to $\mathbf{P}_T$,

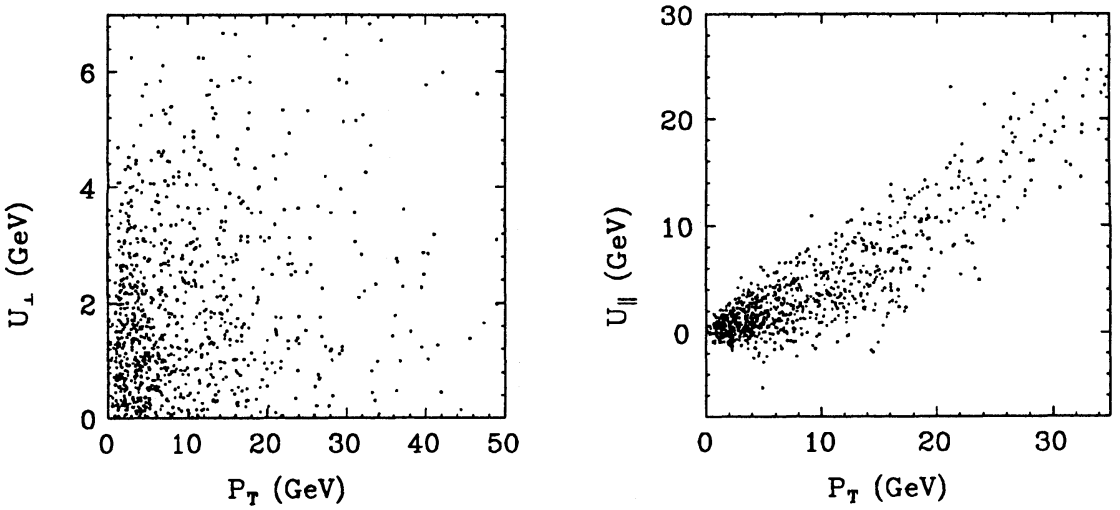


Figure 50. Scatter plots of the reconstructed $u_\perp$ (left) and $u_{||}$ (right) versus the generated $P_T$ of the $W$.

are shown in Figure 50. The smearing of $u_{||}$ and $u_\perp$ can be described by two independent gaussians.

Figure 51 shows the distribution of $u_\perp$ for different intervals of $P_T$. As one would hope, the mean is zero; furthermore, $\sigma_{u_\perp}$ increases with the $P_T$ of the boson. One expects this, since higher-$P_T$ bosons recoil against a more energetic underlying event, in which the effects of detector resolution are likely to be more pronounced. Figure 52 shows a plot of $\sigma_{u_\perp}$ versus $P_T$. A parametrization that suffices for the range of $P_T$ relevant to this analysis is

$$\begin{aligned} \sigma_{u_\perp} &= 1.71 + 0.11 P_T - 0.0013 P_T^2 && (P_T < 40 \text{ GeV}) \\ \sigma_{u_\perp} &= 0.84 + 0.5\sqrt{P_T} && (P_T > 40 \text{ GeV}), \end{aligned}$$

where $P_T$ is expressed in GeV. In our Monte Carlo, we scale up this smearing by an additional 30% to correct for the overoptimism of CDFSIM.

The reconstructed parallel portion of the underlying event, $u_{||}$, is treated sim-

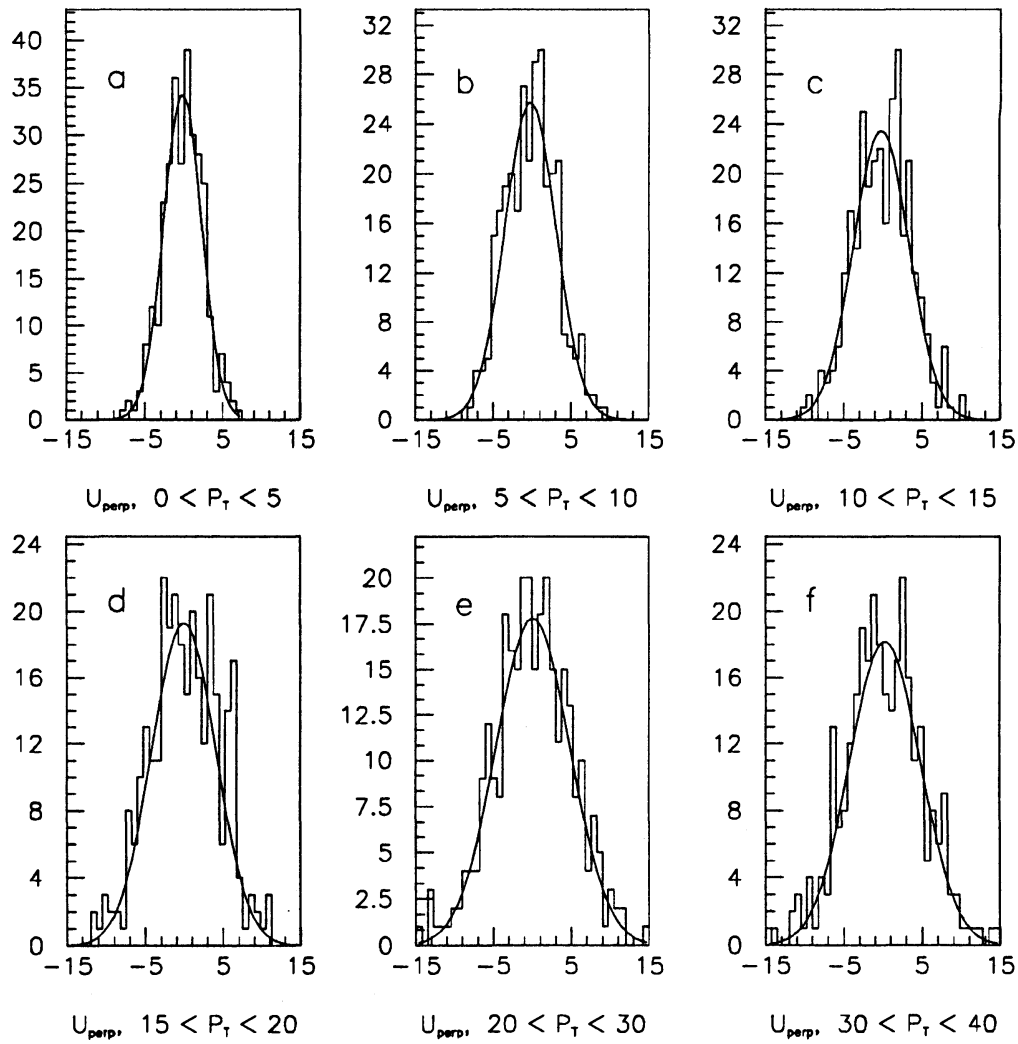


Figure 51. The reconstructed perpendicular component of the underlying event, $u_\perp$, for various intervals of the generated $P_{T,W}$. The $x$-axis is $u_\perp$ in GeV. Ideally $u_\perp$ would be zero; the resolution broadens as the $P_T$ of the boson increases. a) $0 < P_T < 5$; b) $5 < P_T < 10$; c) $10 < P_T < 15$; d) $15 < P_T < 20$; e) $20 < P_T < 30$; f) $30 < P_T < 40$.

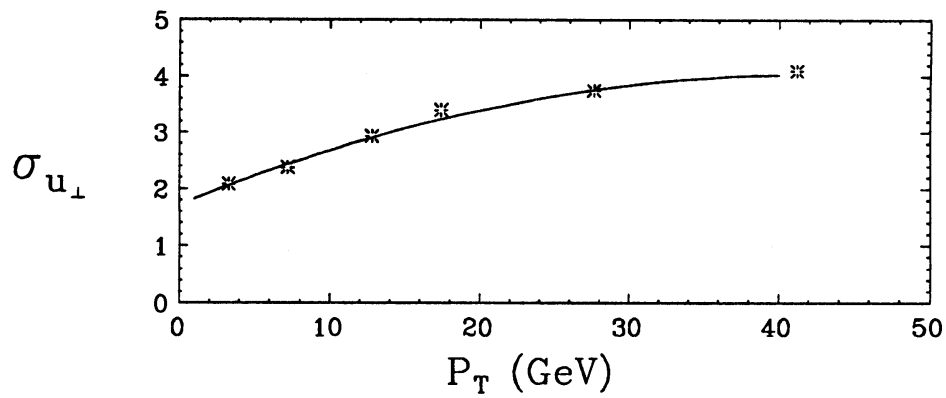


Figure 52. Fit of $\sigma_{u_\perp}$ as a function of $P_T$.

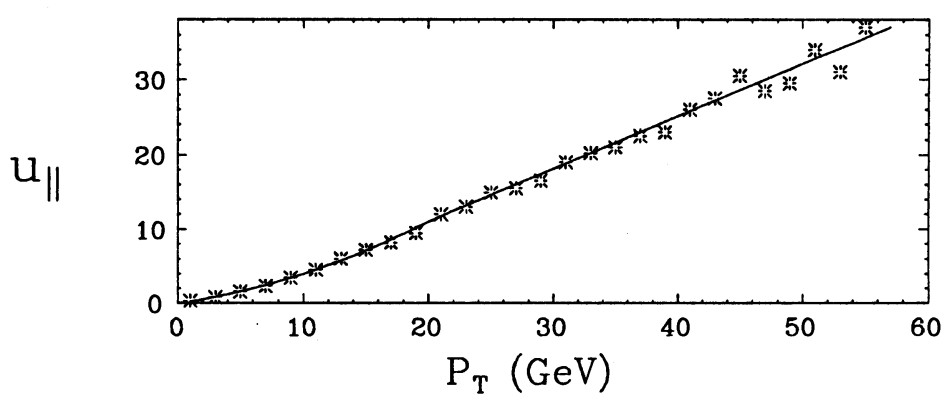


Figure 53. Fit of $u_{||}$ as a function of $P_T$.

ilarly. Because of detector nonlinearities and other effects, the mean of $u_{||}$ is not equal to the $W$ $P_T$. Rather, as shown in Figure 53, $u_{||}$ is well-described by the parametrization

$$\begin{aligned} u_{||} &= 0.234P_T + 0.016P_T^2 \qquad (P_T < 20 \text{ GeV}) \\ u_{||} &= -2.92 + 0.7P_T \qquad (P_T > 20 \text{ GeV}), \end{aligned}$$

with $P_T$ again in GeV.

To determine the smearing of this component, we plot in Figure 54 the difference between the actual and fitted values of $u_{||}$ as a function of $P_T$. We find

$$\sigma_{u_{||}} = 0.75\sqrt{P_T},$$

which works well for the entire range of $P_T$ under consideration.

The parametrizations given above provide a convenient way of incorporating a "realistic" underlying event model into our Monte Carlo without further recourse to time-consuming detector simulations.

## 7.3 Acceptance

The ingredients given above allow us to calculate the geometrical and kinematic acceptance for $W$'s and $W'$'s. The kinematic acceptance is the probability that an event will pass our $E_T$ (or $P_T$) and missing $E_T$ cuts of 30 GeV. We expect this number to rise with the $W'$ mass. The geometrical acceptance is the probability that the charged lepton will land in a fiducial region of the appropriate detector. Again, we expect this probability to increase as a function of $M_{W'}$, although more slowly, since heavier particles tend to be more centrally produced. For purposes of this analysis, we combine these two numbers into a single number, and call it the acceptance.

The acceptance for both electron and muon events is shown as a function of $M_{W'}$ in Figure 55. For muons, the acceptance is 13.5% for $W$'s, rising rapidly to a plateau of about 34% for $W'$'s with masses above 250 GeV. For electrons, the acceptance rises from 23% at the $W$ mass to about 55% for higher-mass $W'$'s. The higher acceptance in the electron channel reflects the greater rapidity coverage of the central electromagnetic calorimeter: its fiducial region extends out to $|\eta| = 1.0$, as against 0.6 for the central muon chambers. We assign a 1% uncertainty to the acceptances, based on its variation when different sets of structure functions are employed.

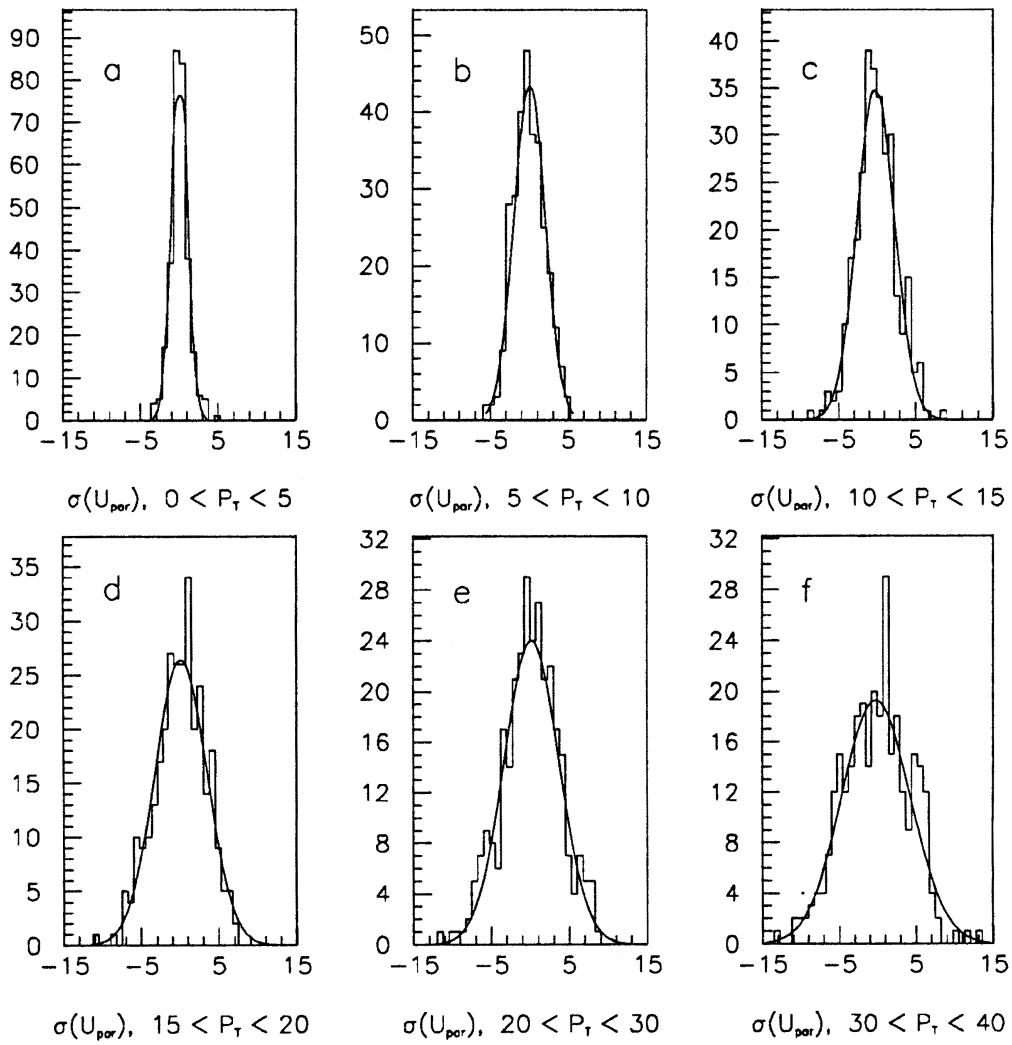


Figure 54. Difference (in GeV) between the actual and fitted values of $u_{||}$ for various intervals of $P_{T_W}$. a) $0 < P_T < 5$; b) $5 < P_T < 10$; c) $10 < P_T < 15$; d) $15 < P_T < 20$; e) $20 < P_T < 30$; f) $30 < P_T < 40$.

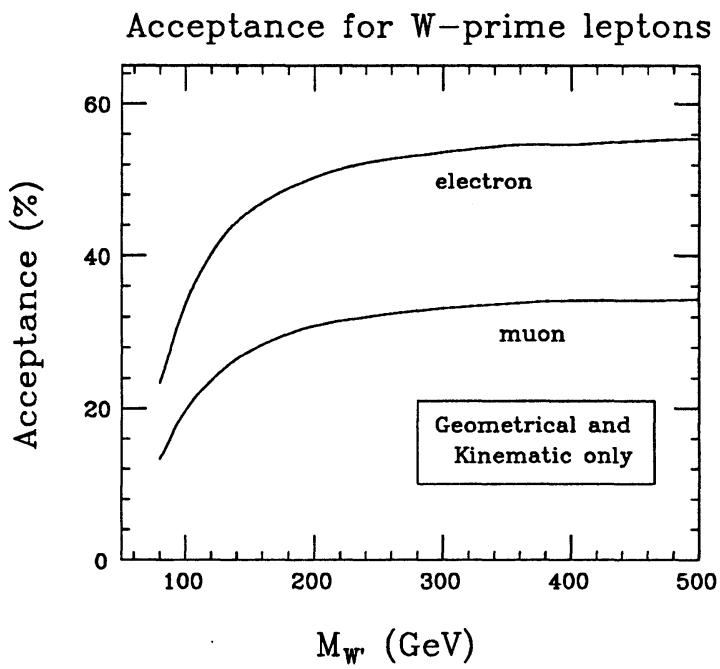


Figure 55. Geometrical and kinematic acceptance for the decays $W' \to e\nu$ and $W' \to \mu\nu$, as a function of $M_{W'}$.

## 7.4 Transverse Mass Distributions

The Monte Carlo transverse mass distributions for $W'$'s of various masses are shown in Figures 56 and 57.

In the electron channel, the characteristic Jacobian peak, with its sharply-falling edge on the high side, is evident at all masses. In the muon channel, this peak is smeared out due to the resolution of the muon momentum, and the peaks for high-mass $W'$'s are quite broad.

In Chapter 5, Figures 18 and 20, the data are shown together with the prediction from this Monte Carlo for $W$ boson decay. The agreement is quite good, considering the simplicity of the Monte Carlo.

An independent check on the reliability of the Monte Carlo is provided by a comparison with a sample of $Z \rightarrow e^+e^-$ events. $Z$ bosons are produced with a $P_T$ distribution and underlying event structure similar to $W$'s; the main difference between the two processes is the presence of a second energetic electron rather than a neutrino. If the second electron is removed, the event looks very much like $W \rightarrow e\nu$. A $Z$ sample therefore provides a convenient and background-free way to check the Monte Carlo. Figure 58 shows the transverse mass distributions for a standard $Z \rightarrow e^+e^-$ sample[62] in which the second electron was removed from the event. Superimposed is a prediction from the Monte Carlo. Although the comparison is limited by the low statistics of the $Z$ data, the agreement is good.

We shall return to the transverse mass distributions for $W \rightarrow l\nu$ and their agreement with the data in the next chapter, when we use them to extract a limit on $W'$ production.

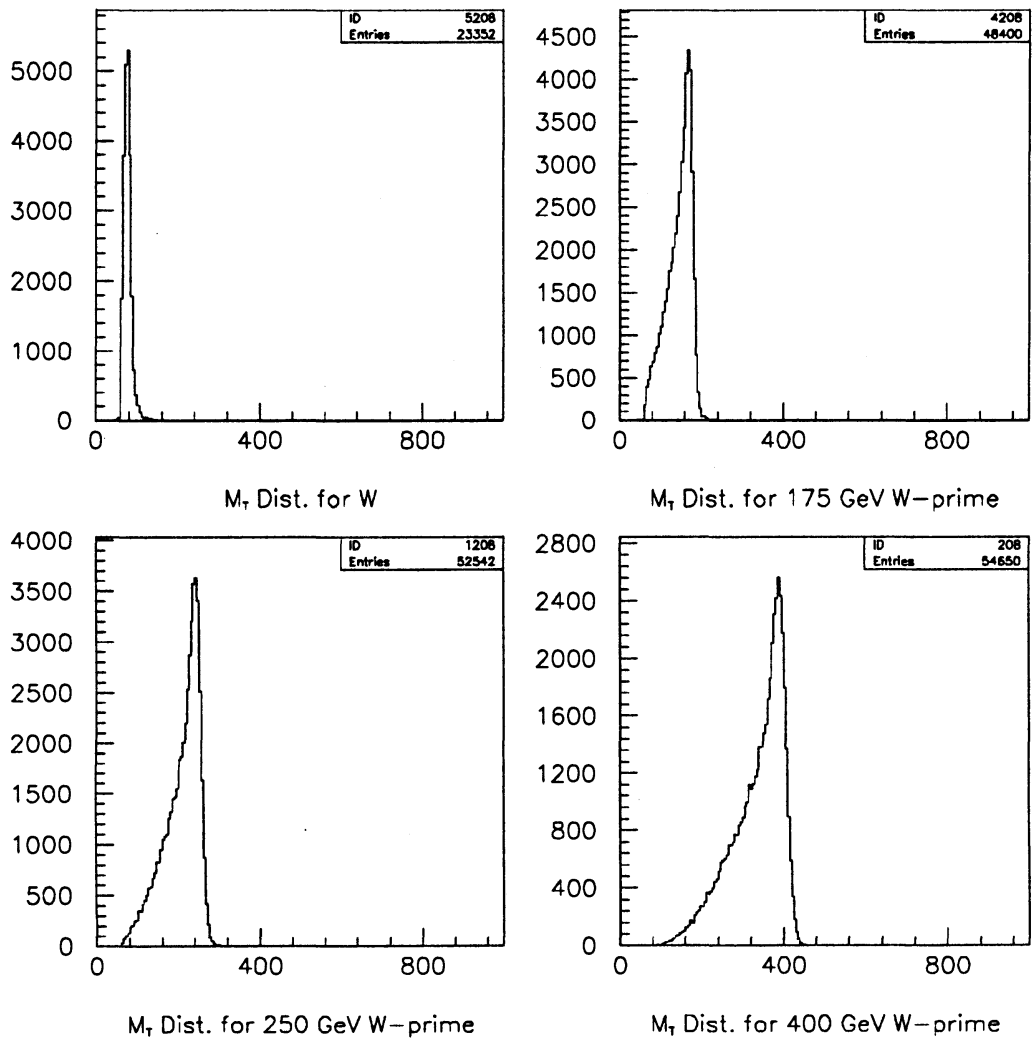


Figure 56. Monte Carlo transverse mass distributions (in GeV) for $W$ and $W'$ decays in the electron channel.

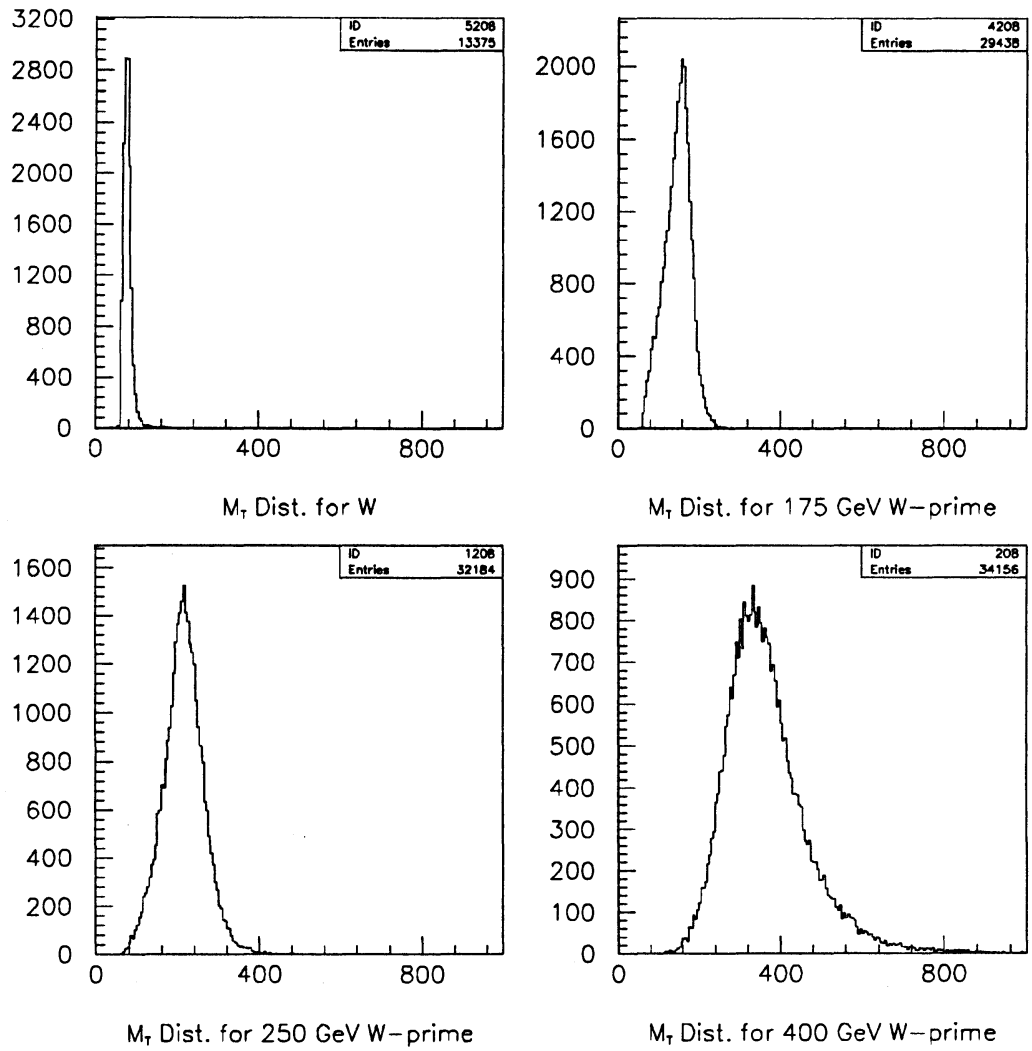


Figure 57. Monte Carlo transverse mass distributions (in GeV) for $W$ and $W'$ decays in the muon channel.

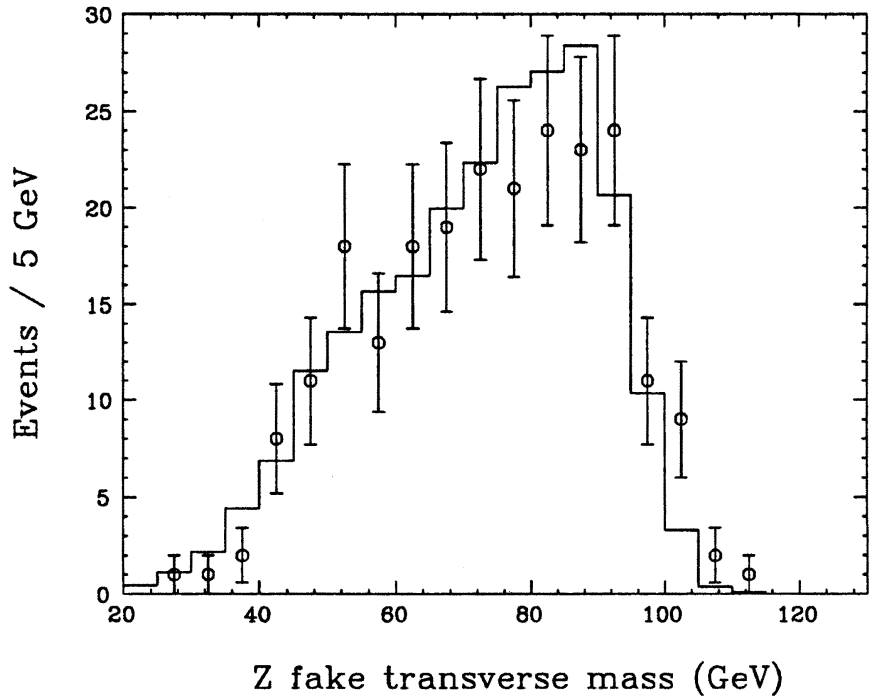


Figure 58. Transverse mass of $Z \rightarrow e^+e^-$ events with one electron removed. The data points are from a standard $Z \rightarrow e^+e^-$ sample, and the histogram is the prediction from the Monte Carlo program discussed in the text.

# CHAPTER 8

# RESULTS

We now have in hand nearly all of the ingredients necessary to extract a limit on $\sigma \cdot B(W' \rightarrow e\nu)$ and $\sigma \cdot B(W' \rightarrow \mu\nu)$. We have selected electron and muon datasets, and have evaluated the efficiencies of the cuts that went into this selection. We have also developed the Monte Carlo techniques that allow us to calculate the $W'$ production cross sections and acceptances, as well as the transverse mass distributions. In this final chapter, we put everything together and calculate how many $W'$'s we would expect to find in our sample, if the $W'$ has standard-strength couplings. We then fit the observed transverse mass distributions to a superposition of $W$ and $W'$ Monte Carlo distributions to determine the actual number of $W'$ events observed, if any. The observed transverse mass distributions were shown in Chapter 5, Figures 18 and 20. We perform this fit for a variety of $W'$ masses, and for each mass we produce a probability distribution describing the number of $W'$'s in the sample. We next incorporate systematic uncertainties into the probability distributions. Finally, the probability distributions are integrated to obtain limits on the $W'$ cross section times leptonic branching ratio, and these limits are converted into a limit on the $W'$ mass.

## 8.1 Number of $W'$ Events Expected

The number of events expected of a given type is

$$N_{exp} = \mathcal{L}(\sigma \cdot B)A\epsilon,$$

where $\mathcal{L}$ is the integrated luminosity, $\sigma \cdot B$ is the cross section times leptonic branching ratio, $A$ is the geometrical and kinematic acceptance, and $\epsilon$ is the overall efficiency, which includes both the trigger and lepton identification efficiencies. We have already calculated each of these individual factors. Tables 3 and 4 summarize the number of $W' \rightarrow e\nu$ and $W' \rightarrow \mu\nu$ events expected, assuming standard-strength couplings and a branching ratio of 1/12 to each lepton family.

A $W'$ with standard-strength couplings would have a stunning experimental signature. Figure 59 shows what a 300 GeV $W'$ would look like if it were present in the electron sample. A $W'$ with this mass is nearly 100 GeV beyond the reach of the previous direct searches at CERN, but in our data it would be easily visible.

## 8.2 Fitting Transverse Mass

To determine the actual number of $W'$ events present in the data, we fit the observed transverse mass distribution to a superposition of $W$ and $W'$ Monte Carlo, using a binned likelihood method with Poisson statistics. Let $n_{i,obs}$ be the number of events observed in the $i^{th}$ 5 GeV transverse mass bin. Let $W_i$ be the number of $W$ events expected in this bin. Now fix the $W'$ mass at some value, and let $W'_i$ be the number of $W'$ events expected in this same bin, assuming standard-strength couplings. Then the total number of events expected in the $i^{th}$ bin is

$$n_{i,exp} = \alpha W'_i + \beta W_i,$$

where $\alpha$ and $\beta$ represent the $W'$ and $W$ fractions present in the data, relative to the amounts predicted by standard strength couplings. The parameter $\alpha$ is therefore

Table 3. Number of $W' \rightarrow e\nu$ events expected in $\mathcal{L} = 4.15$ pb$^{-1}$

| $M_{W'}$ (GeV) | $\sigma \cdot B$ (pb) | A | $\epsilon$ | $N_{exp}$ |
|---|---|---|---|---|
| 80 ($W$) | 2237 | $.233 \pm .01$ | $.845 \pm .035$ | $1909 \pm 174$ |
| 85 | 1487 | $.258 \pm .01$ | $.845 \pm .035$ | $1345 \pm 103$ |
| 90 | 1257 | $.287 \pm .01$ | $.843 \pm .035$ | $1262 \pm 97$ |
| 100 | 918 | $.335 \pm .01$ | $.840 \pm .035$ | $1072 \pm 83$ |
| 125 | 464 | $.414 \pm .01$ | $.834 \pm .035$ | $665 \pm 51$ |
| 150 | 259 | $.458 \pm .01$ | $.829 \pm .035$ | $408 \pm 31$ |
| 175 | 156 | $.484 \pm .01$ | $.826 \pm .035$ | $259 \pm 20$ |
| 200 | 98.1 | $.503 \pm .01$ | $.821 \pm .035$ | $168 \pm 13$ |
| 250 | 43.2 | $.525 \pm .01$ | $.809 \pm .035$ | $76.1 \pm 5.9$ |
| 300 | 20.8 | $.536 \pm .01$ | $.793 \pm .035$ | $36.7 \pm 2.8$ |
| 350 | 10.6 | $.545 \pm .01$ | $.774 \pm .035$ | $18.6 \pm 1.4$ |
| 400 | 5.59 | $.546 \pm .01$ | $.752 \pm .035$ | $9.52 \pm .73$ |
| 450 | 3.02 | $.551 \pm .01$ | $.728 \pm .035$ | $5.03 \pm .39$ |
| 500 | 1.64 | $.554 \pm .01$ | $.705 \pm .035$ | $2.66 \pm .20$ |

Table 4. Number of $W' \rightarrow \mu\nu$ events expected in $\mathcal{L} = 3.54$ pb$^{-1}$

| $M_{W'}$ (GeV) | $\sigma \cdot B$ (pb) | A | $\epsilon$ | $N_{exp}$ |
|---|---|---|---|---|
| 80 ($W$) | 2237 | $.134 \pm .01$ | $.76 \pm .06$ | $837 \pm 100$ |
| 85 | 1487 | $.147 \pm .01$ | $.76 \pm .06$ | $584 \pm 53$ |
| 90 | 1257 | $.167 \pm .01$ | $.76 \pm .06$ | $561 \pm 51$ |
| 100 | 918 | $.197 \pm .01$ | $.76 \pm .06$ | $483 \pm 44$ |
| 125 | 464 | $.244 \pm .01$ | $.76 \pm .06$ | $303 \pm 28$ |
| 150 | 259 | $.275 \pm .01$ | $.76 \pm .06$ | $190 \pm 17$ |
| 175 | 156 | $.294 \pm .01$ | $.76 \pm .06$ | $123 \pm 11$ |
| 200 | 98.1 | $.308 \pm .01$ | $.76 \pm .06$ | $80.8 \pm 7.4$ |
| 250 | 43.2 | $.322 \pm .01$ | $.76 \pm .06$ | $37.2 \pm 3.4$ |
| 300 | 20.8 | $.331 \pm .01$ | $.76 \pm .06$ | $18.4 \pm 1.7$ |
| 350 | 10.6 | $.337 \pm .01$ | $.76 \pm .06$ | $9.55 \pm .91$ |
| 400 | 5.59 | $.342 \pm .01$ | $.76 \pm .06$ | $5.11 \pm .47$ |
| 450 | 3.02 | $.341 \pm .01$ | $.76 \pm .06$ | $2.75 \pm .25$ |
| 500 | 1.64 | $.343 \pm .01$ | $.76 \pm .06$ | $1.50 \pm .14$ |

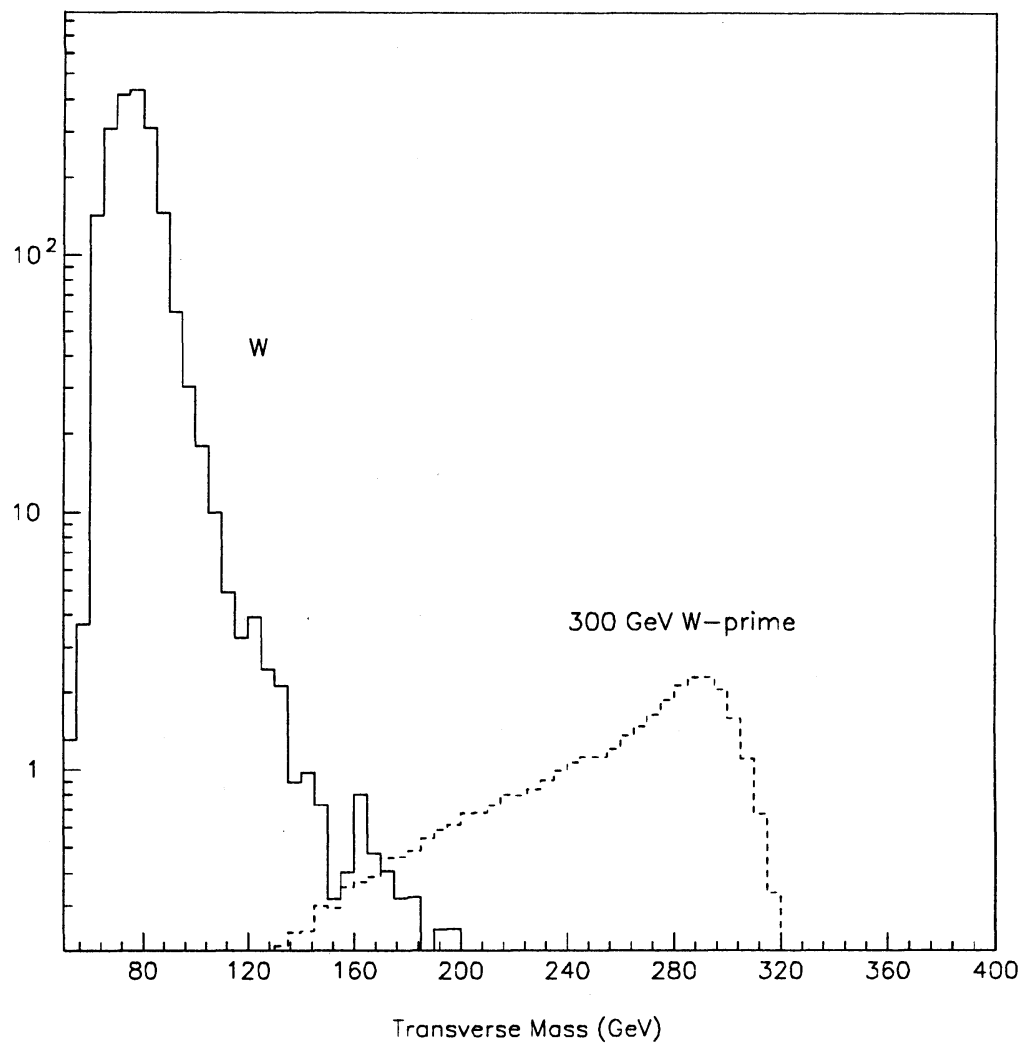


Figure 59. A 300 GeV $W'$ as it would appear in the electron sample if present with standard-strength couplings. Approximately 37 events would be expected.

the same as $\frac{\lambda^2}{\lambda^2_{SM}}\frac{B}{1/12}$. (Recall from Chapter 1 that $\lambda^2$ measures the strength of the quark–$W'$ coupling relative to the standard-model coupling, with $\lambda^2_{SM} = 1$.) Equivalently, $\alpha$ is the ratio of the actual cross section times branching ratio to the standard-strength value. The Poisson probability that $n_{i,obs}$ events would actually be observed in the $i^{th}$ bin is then

$$P_i = (n_{i,exp})^{n_{i,obs}} \frac{e^{-n_{i,exp}}}{n_{i,obs}!},$$

and the full likelihood function is given by the product over all bins of the $P_i$. The negative log-likelihood function to be minimized is

$$\begin{aligned} \mathcal{M}_0 &= \sum_i (n_{i,exp} - n_{i,obs} \ln n_{i,exp}) \\ &= \sum_i (\alpha W'_i + \beta W_i - n_{i,obs} \ln(\alpha W'_i + \beta W_i)), \end{aligned}$$

where we have dropped a term independent of $\alpha$ and $\beta$.

This function is minimized with respect to $\alpha$ and $\beta$, using the CERN Library program MINUIT[70]. Throughout the fit, $\alpha$ and $\beta$ are constrained on physical grounds to be non-negative, as advocated by the Particle Data Group[71].

It is useful, in order to extract a limit, to deal with a one-parameter likelihood function depending on $\alpha$ alone. Such a function is simple to construct. Although the right thing to do might appear to be to fix $\beta$ at its best-fit value and treat the likelihood function as a function only of alpha, in fact this is not quite correct. If $\alpha$ and $\beta$ are correlated, the likelihood function for $\alpha$ obtained in this way would depend on the direction, in $\alpha$-$\beta$ space, in which one moved away from the minimum. Instead, we calculate the likelihood function for $\alpha$ by fixing $\alpha$ at a succession of points and minimizing at each point with respect to $\beta$. In practice, the difference between these two approaches is small since $\alpha$ and $\beta$ are essentially uncorrelated, except for the case $M_{W'} = 85$ GeV, where the correlation coefficient is 0.95 in the electron sample. The likelihood functions (or rather, the associated probability distributions) obtained in this way for a 125 GeV and 300 GeV $W'$ in the muon channel are shown

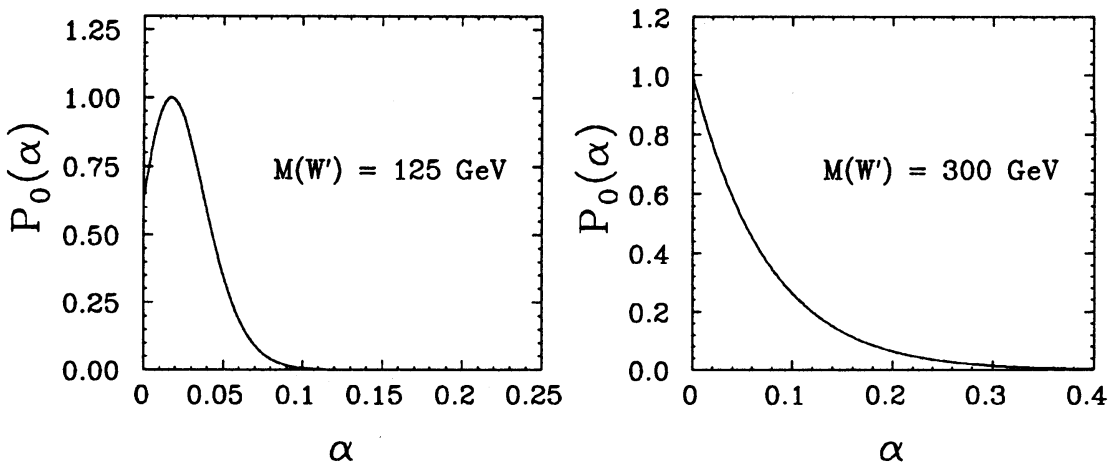


Figure 60. Probability distribution for the $W'$ fraction $\alpha$ in the muon sample, for $M_{W'} = 125$ GeV (left) and 300 GeV (right).

in Figure 60. We call this one-parameter probability distribution $\mathcal{P}_0(\alpha)$. The peak away from zero in the plot on the left indicates that the fitter prefers a nonzero fraction of $W'$ events in the muon data, for $M_{W'} = 125$ GeV. This is the effect of the events in the tail, which were discussed in Chapter 5. For a 300 GeV $W'$, and for nearly all other values of the $W'$ mass, the fitter finds no signal in either sample.

As a cross-check, we note that the best-fit value of the $W$ fraction $\beta$ allows us to extract the $W$ cross section times leptonic branching ratio. It is given by

$$\sigma \cdot B(W \to l\nu) = \frac{N_{exp}\beta}{\mathcal{L}A\epsilon},$$

where $N_{exp}$, $A$, and $\epsilon$ can be read off from Tables 3 and 4. In both samples and for all $W'$ masses, the fitter finds $\beta = 0.92$–$0.94$. (The predicted $W$ cross section, which goes into the determination of $N_{exp}$ and into the normalization of the distributions used in the fit, is uncertain to 10–20%, so the fact that $\beta$ does not come out to be

one is not particularly surprising.) We thus find the central values

$$\begin{aligned}\sigma \cdot B(W \to l\nu) &= 2.27 \text{ nb (electron sample)} \\ &= 2.16 \text{ nb (muon sample)}\end{aligned}$$

In independent analyses[53, 72] based on event selection criteria different from those employed here, CDF has measured $\sigma \cdot B(W \to e\nu) = 2.19 \pm 0.04 \pm 0.21$ nb and $\sigma \cdot B(W \to \mu\nu) = 2.21 \pm 0.22$ nb, for a combined measurement of

$$\sigma \cdot B(W \to l\nu) = 2.20 \pm 0.20 \text{ nb (CDF)}.$$

Our $W$ cross section is thus in good agreement with this independent[1] result. This provides a check of our entire analysis path, including the event selection, efficiency and acceptance calculations, and fitting algorithm.

It is now (almost) simple to derive a limit on the $W'$ cross section times branching ratio. To obtain the 95% confidence-level limit on a 300 GeV $W'$ in the muon channel, say, we integrate the probability distribution in Figure 60 and determine the value of $\alpha$, call it $\alpha_{CL}$, which includes 95% of the area under the curve. The limit on the cross section times branching ratio is then

$$(\sigma \cdot B)_{95\%\ C.L.} = \alpha_{CL}(\sigma \cdot B)_{Std.\ Str.}.$$

However, we have not yet included the effect of systematic uncertainties. These modify the probability distribution, and must be incorporated before we can extract the limits.

[1] Well. sort of. The cross section analyses and this analysis have some event selection cuts in common, and there is significant overlap between the two datasets. The cross section analyses, however, made the looser requirements $E_T$ ($P_T$) > 20 GeV and $\not{E}_T$ > 20 GeV (we cut at 30 and 30), so the acceptances and the event samples (as well as the backgrounds) were larger. And the cross sections were determined not from a fit, but from simple event counting after a background subtraction.

## 8.3 Systematic Uncertainties

The systematic uncertainties that affect this analysis are of two types:

1. Those that affect the shape of the transverse mass distributions, and therefore change the relative values of $\alpha$ and $\beta$;

2. Those that affect the overall rate, and therefore change the number of expected events by a common scale factor.

Uncertainties of the first type are dominated by uncertainties in the $W$ and $W'$ $P_T$ distributions and in the underlying event model, while those of the second type include uncertainties in the lepton selection efficiencies and the overall 6.8% uncertainty in the luminosity normalization[73]. We will generically denote uncertainties of the first type by $\Delta\alpha$, and those of the second type by $\Delta n$.

To take account of uncertainties in the boson $P_T$ distributions, we generated new Monte Carlo transverse mass distributions with the nominal $P_T$ of the boson scaled by a factor of $\pm 25\%$. Changing the $P_T$ results in a small change in the acceptance, and we normalized the distributions to the new acceptances. We then performed a new likelihood fit to the data. A harder (*i.e.* less steeply-falling) $P_T$ distribution for the $W$ broadens the high-mass tail of the transverse mass distribution, causing the actual events in the tail to be attributed to $W$'s rather than to $W'$'s. Conversely, a softer $P_T$ distribution leads to an excess of events in the tail compared to the Monte Carlo prediction for $W$'s, and for certain $W'$ masses the fitter will prefer a nonzero $W'$ fraction to make up the difference. Figure 61 shows the effect of the changes in the $W$ $P_T$ on the tail of the transverse mass distribution. The Monte Carlo predictions are overlaid with the muon data.

The transverse mass distributions are affected, albeit to a lesser extent, by uncertainties in the model of the underlying event. In particular, the transverse mass distributions are sensitive to the amount by which the portion of the underlying

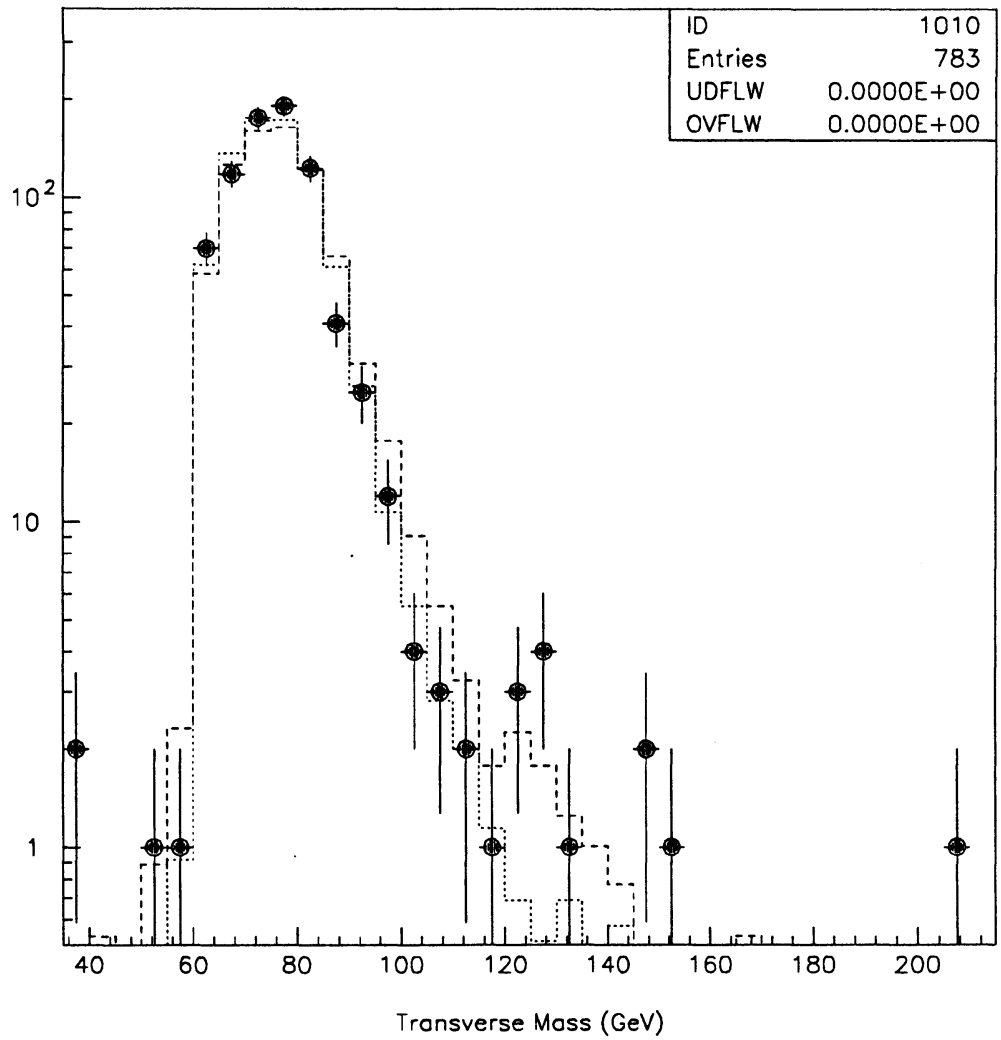


Figure 61. Effect of varying the $W$ $P_T$ distribution. The muon data are shown together with Monte Carlo predictions made by varying the $W$ $P_T$ distribution by a scale factor of 0.75 (dots) and 1.25 (dashes).

event parallel to the boson direction, $u_{\|}$, is smeared. This smearing is controlled by a parameter called COH_RES, via

$$\sigma_{u_{\|}} = \text{COH_RES}\sqrt{P_T^W},$$

where $P_T^W$ is the true $P_T$ of the boson. (The dependence on the square root arises from the nature of the calorimeter resolution, which is determined by the counting statistics of photoelectrons.) The nominal value of COH_RES is 0.75; to determine the systematic uncertainty in $\alpha$ due to this parameter we refit the data using COH_RES = 0.60 and 1.20, again normalizing the Monte Carlo transverse mass distributions to the (very slightly) modified acceptances.

It is a feature of this analysis that for higher $W'$ masses—above 200 GeV or so—variations in these parameters have little effect on the fitted value of $\alpha$. This is because the $W$ and $W'$ distributions are so dissimilar that the fitter has no trouble telling them apart, regardless of effects that may broaden the peaks.

We use as the uncertainties $\Delta\alpha$ the average shift in the best-fit value of $\alpha$ when the parameter in question is varied. If $\alpha$ itself does not change (as happens for higher-mass $W'$'s, where $\alpha$ is zero no matter what), we take the average change in the statistical error on $\alpha$ returned by MINUIT as an estimate of the systematic uncertainty. Because the individual contributions to $\Delta\alpha$ from variations in the $P_T$ distributions and underlying event model are expected to be uncorrelated, we add them in quadrature to determine the overall $\Delta\alpha$ for each value of $M_{W'}$.

The other systematic uncertainties, $\Delta n$, do not require refitting the transverse mass distributions, as they affect only the overall rates. They are known in advance from the efficiency study ($\Delta n_{eff}$ = 6.0% for the muons and 3.5% for the electrons) and from the common CDF luminosity uncertainty ($\Delta n_{lum}$ = 6.8%). We also include a 1% systematic uncertainty on the acceptances. These systematic uncertainties are added in quadrature to give overall scale uncertainties of 7.7% (electrons) and 9.1% (muons).

The two types of systematic uncertainties must be incorporated into the probability distribution in different ways. This method has been applied previously in the CDF search for the top quark[74]. The $\Delta\alpha$'s are folded into the one-parameter probability distribution $\mathcal{P}_0(\alpha)$ by smearing the nominal value of $\alpha$ by a gaussian with a sigma of $\Delta\alpha$:

$$\mathcal{P}'(\alpha') = \int_0^\infty \mathcal{P}_0(\alpha'')G(\alpha'' - \alpha'; 0, \Delta\alpha)d\alpha''.$$

Note that $\alpha$ is constrained to be non-negative. Finally, the scale uncertainties $\Delta n$ are folded in by performing a convolution of the smeared probability distribution $\mathcal{P}'$ with a gaussian with a mean of 1 and a $\sigma$ of $\Delta n$:

$$\mathcal{P}(\alpha) = \int_0^\infty \mathcal{P}'(\alpha')G(\alpha'/\alpha; 1, \Delta n)d\alpha'.$$

It is this probability distribution that we integrate to obtain the 95% confidence-level limit on the $W'$ fraction. We then multiply by the conversion factor $(\sigma \cdot B)_{Std.\ Str.}$ (from Tables 3 and 4) to get an absolute limit on the $W'$ cross section times branching ratio. The integrals above are evaluated numerically according to the following algorithm, which is worth spelling out:

1. Pick a random value of $\alpha$ according to the unsmeared distribution $\mathcal{P}_0$.

2. Let $G(\bar{x}, \sigma)$ be a random number drawn from a Gaussian distribution with mean $\bar{x}$ and standard deviation $\sigma$. We choose a number $\sigma_1 = G(0, 1)$, and then perform the smearing

$$\alpha \rightarrow \alpha + \Delta\alpha \cdot \sigma_1$$

3. Now smear the new value by the $\Delta n$-type uncertainty. Let $\sigma_2 = G(1, \Delta n)$. Then

$$\alpha \rightarrow \alpha \cdot \sigma_2$$

   Bin the resulting $\alpha$ into a new histogram. This step is repeated many (roughly 1000) times.

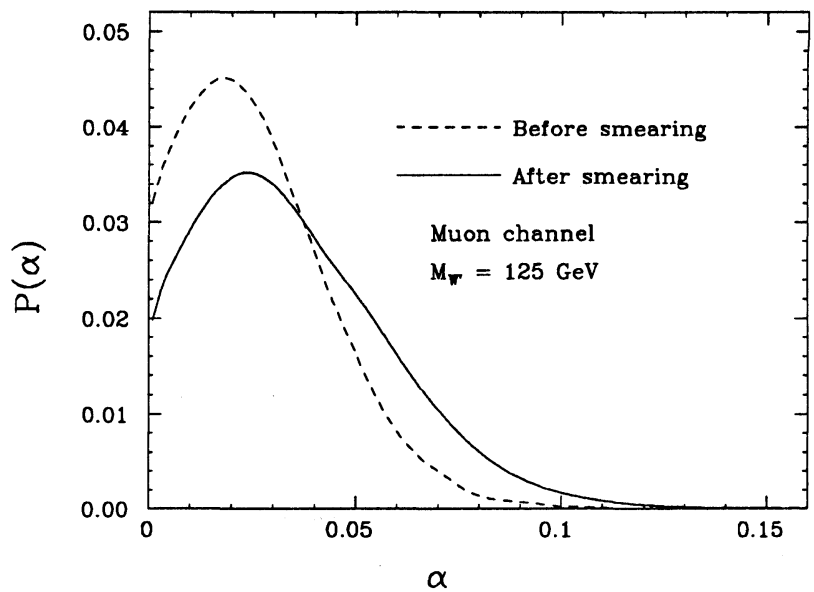


Figure 62. Probability distributions for a 250 GeV $W'$ in the muon channel, before and after smearing.

4. Return to Step 1 and choose a new $\alpha$. Repeat several thousand times.

In Figure 62, the probability distribution for a 125 GeV $W'$ in the muon channel is shown before and after smearing. The effect is large here (larger, in fact, than for any other $W'$ mass) because the input $P_T$ distribution for the bosons has a great deal to do with whether or not the events in the tail near 120 GeV are attributed to $W$ or to $W'$ by the fitter, and $\Delta\alpha$ is therefore large. A more typical situation is shown in Figure 63, with the smeared and unsmeared probability distributions for a 250 GeV $W'$, again in the muon channel. The effect of smearing is mainly visible near $\alpha = 0$. The sharp peak turns over after smearing because of the constraint that $\alpha \geq 0$, so that a point near zero can move to the right but not to the left.

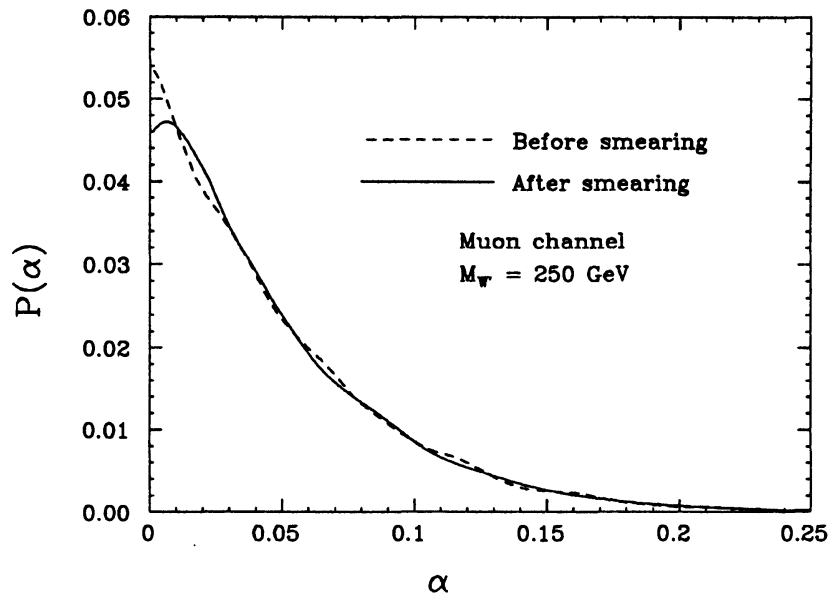


Figure 63. Probability distributions for a 250 GeV $W'$ in the muon channel, before and after smearing.

## 8.4 Limits on $W'$ Production and Decay

We have already indicated how to obtain the limits on $\sigma \cdot B(W' \to l\nu)$ in the electron or muon channel, by integrating the smeared probability distribution to obtain the 95% confidence-level limit on the $W'$ fraction $\alpha$, and then multiplying by the appropriate standard-strength cross section and branching ratio. We now present these limits for the electron, muon, and combined channels.

### *8.4.1 Limits on $W' \to e\nu$ and $W' \to \mu\nu$*

The 95% confidence-level limits on the processes $W' \to e\nu$ and $W' \to \mu\nu$ are shown in Figure 64. The plot shows our limit on the cross section times branching ratio, as a function of the $W'$ mass. The standard-strength prediction is also shown. We emphasize that our experimentally derived limit is independent of this theoretical prediction. In Figure 65, the same result is presented as a limit on the ratio of the actual $W'$ coupling $\lambda^2 B$ to the standard-strength value $\lambda^2_{SM} B = 1 \cdot \frac{1}{12}$. If one assumes that the $W'$ has standard-strength couplings, these limits can be converted to a limit on the $W'$ mass itself. For the electron channel, this limit is

$$M_{W'} > 490 \text{ GeV (95\% confidence level)}.$$

For the muon channel, the limit is

$$M_{W'} > 435 \text{ GeV (95\% confidence level)}.$$

### *8.4.2 Combined Limit on $W' \to l\nu$*

To combine the limits, in the absence of systematic uncertainties, we would form the product of the individual probability distributions, $\mathcal{P}_{0,e}$ and $\mathcal{P}_{0,\mu}$, and

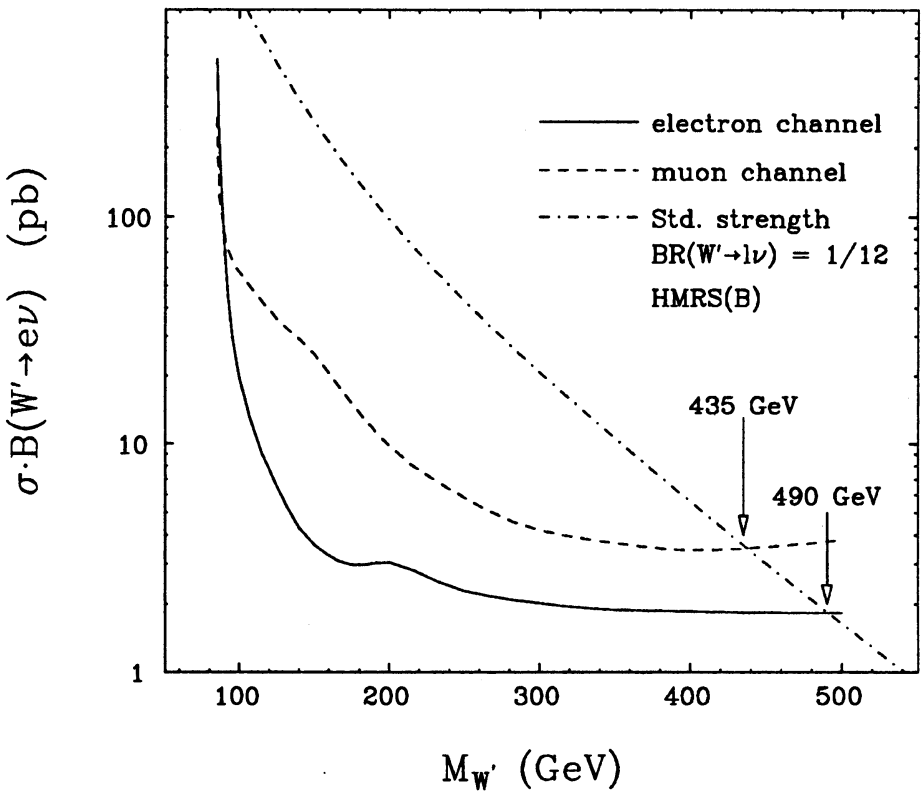


Figure 64. 95% confidence-level limits on $\sigma \cdot B(W' \to e\nu)$ and $\sigma \cdot B(W' \to \mu\nu)$. The area above the curves is disallowed. Also shown is the prediction for standard-strength couplings.

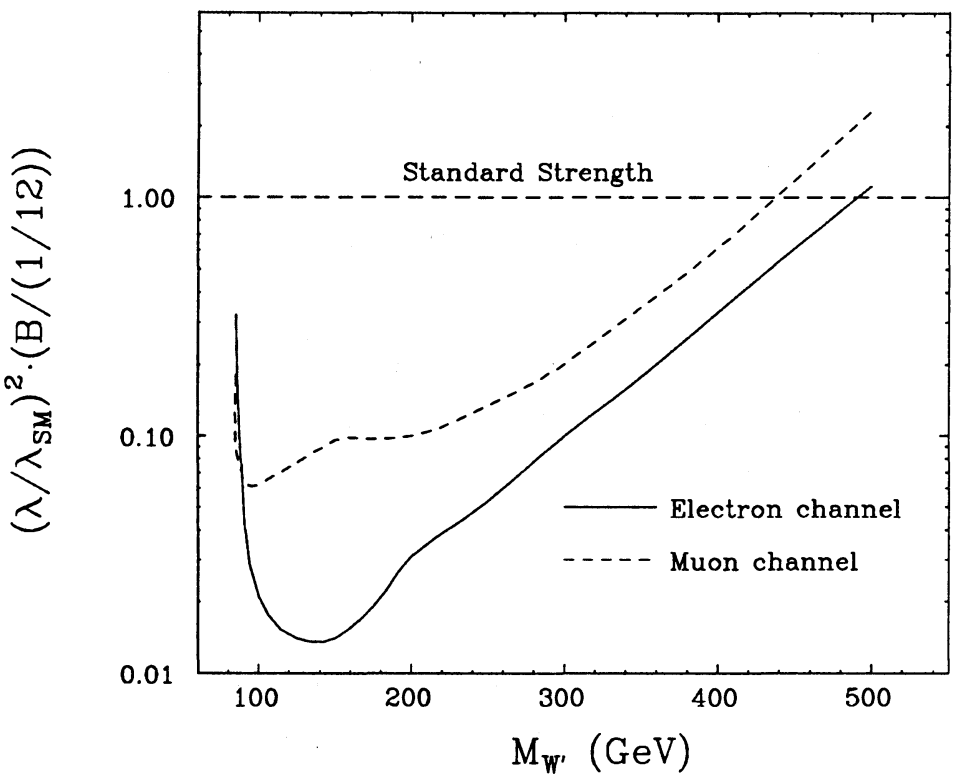


Figure 65. 95% confidence-level limits on the ratio of $\lambda^2 B$ to its standard-strength value of 1/12. The region above the curves is excluded.

integrate the result to obtain the limit. Systematic uncertainties are folded in as before, except that now one must take care to account for possible correlations. The luminosity uncertainty is obviously common to both channels. Electrons and muons, however, are selected with completely different triggers and sets of cuts, so we treat the uncertainties in the efficiencies as uncorrelated. The $\Delta\alpha$-type uncertainties we treat as completely correlated, since the $P_T$ distribution and underlying event for $W'$'s should be the same regardless of which lepton the $W'$ decides to decay into. The procedure for combining the limits is as follows:

1. Values $\alpha_e$ and $\alpha_\mu$ are drawn according to the unsmeared probability distributions $\mathcal{P}_{0,e}(\alpha)$ and $\mathcal{P}_{0,\mu}(\alpha)$.

2. Let $G(\bar{x}, \sigma)$ be a random number drawn from a gaussian distribution with mean $\bar{x}$ and standard deviation $\sigma$. We choose a number $\sigma_1 = G(0,1)$, and then perform the smearing:

$$\begin{aligned} \alpha_e &\rightarrow \alpha_e + \Delta\alpha_e \cdot \sigma_1 \\ \alpha_\mu &\rightarrow \alpha_\mu + \Delta\alpha_\mu \cdot \sigma_1. \end{aligned}$$

3. The new values are then smeared by both correlated and uncorrelated $\Delta n$-type uncertainties, $\Delta n^c$ and $\Delta n^u$. Let $\sigma_2 = G(1, \Delta n^c)$. Then

$$\begin{aligned} \alpha_e &\rightarrow \alpha_e \cdot \sigma_2 \cdot G(1, \Delta n_e^u) \\ \alpha_\mu &\rightarrow \alpha_\mu \cdot \sigma_2 \cdot G(1, \Delta n_\mu^u) \end{aligned}$$

   The resulting smeared $\alpha$'s are binned into separate histograms. This step is repeated many (roughly 1000) times.

4. Return to Step 1 and choose new $\alpha$'s. This step is repeated many (several thousand) times.

5. Finally, take the product of the smeared distributions, and integrate it to obtain the combined 95% confidence level limit. Figure 66 shows the two smeared probability distributions for a 250 GeV $W'$, together with their product.

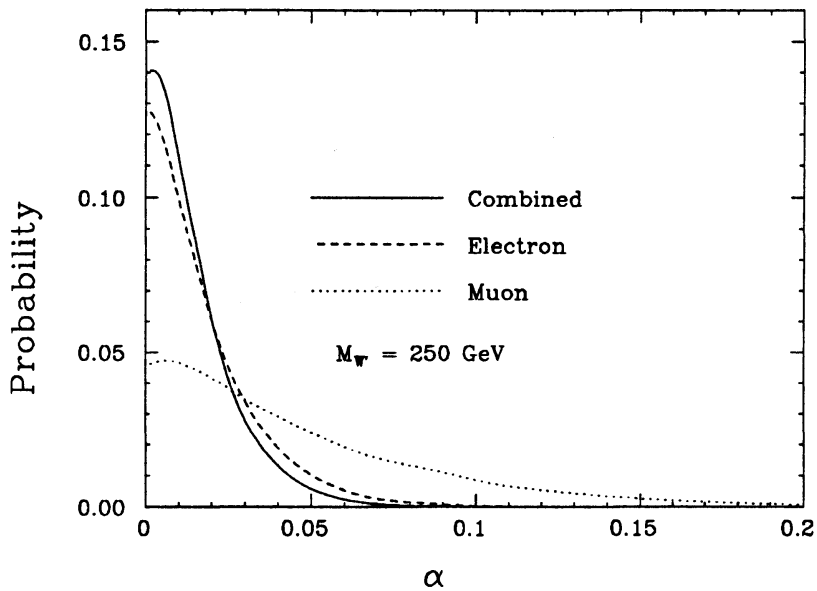


Figure 66. Smeared electron, muon, and combined probability distributions for $M_{W'} = 250$ GeV.

The 95% confidence-level limit on the process $W' \to l\nu$ based on the combined electron and muon results, is shown in Figure 67. Also shown in this figure are the electron and muon results. The standard-strength prediction is also shown. We emphasize that our experimentally derived limit is independent of this prediction. This plot is the major result of this thesis. In Figure 68, the same result is presented as a limit on the ratio of the actual $W'$ coupling $\lambda^2 B$ to the standard-strength value $\lambda^2_{SM} B = 1 \cdot \frac{1}{12}$. If one assumes that the $W'$ has standard-strength couplings, these limits can be converted to a limit on the $W'$ mass itself. Combining the electron and muon channels, the limit is

$$M_{W'} > 520 \text{ GeV (95\% confidence level)}.$$

The limits are summarized in Table 5, which also lists the results of the fit.

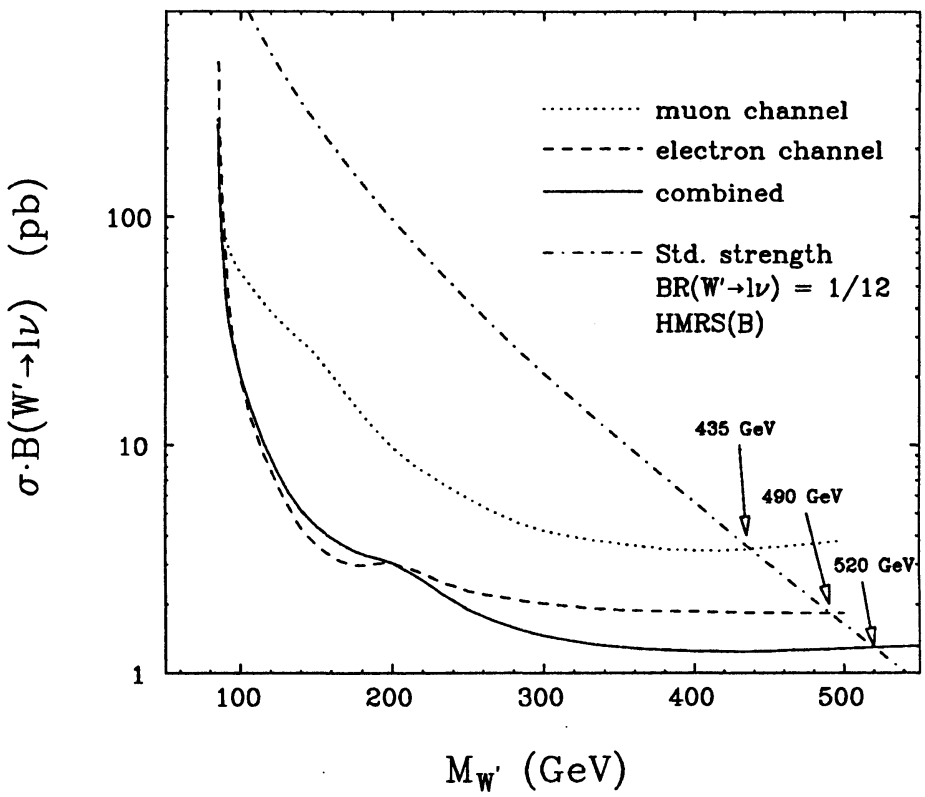


Figure 67. 95% confidence-level limits on the $W'$ cross section times branching ratio in the electron, muon, and combined channels. The area above the curves is disallowed. Also shown is the prediction for standard-strength couplings.

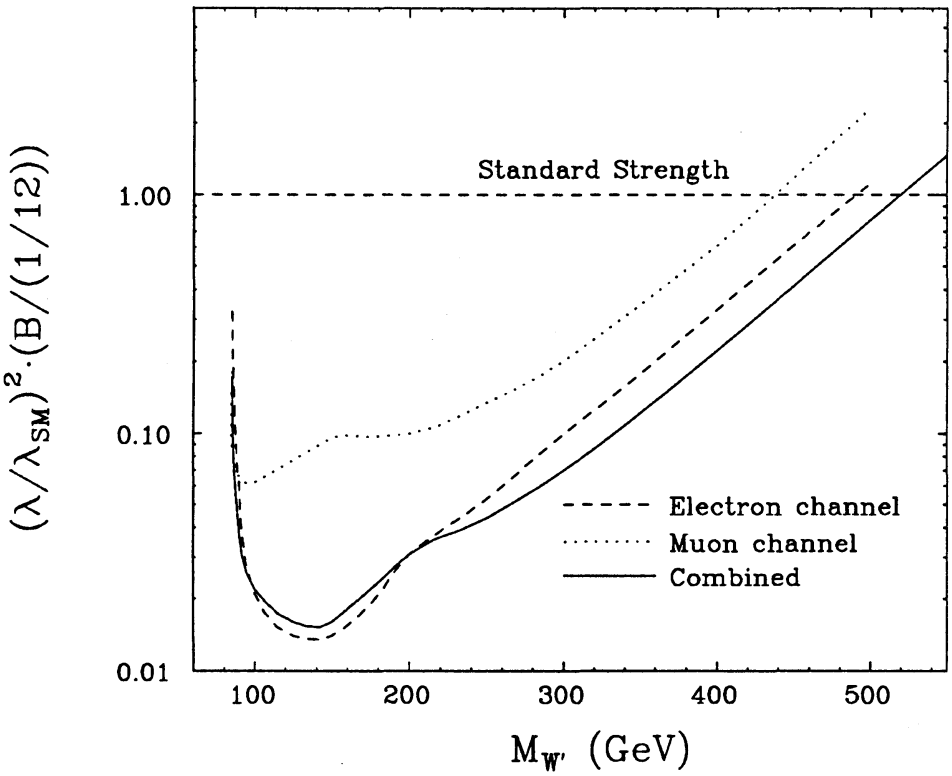


Figure 68. 95% confidence-level limits on the ratio of $\lambda^2 B$ to its nominal value of 1/12, for the electron, muon, and combined channels. The region above the curves is excluded.

Table 5. Summary of results. Limits in the last three columns are at the 95% confidence level

| $M_{W'}$ (GeV/$c^2$) | $\alpha \pm$ (stat) $\pm$ (syst) (electron) | $\alpha \pm$ (stat) $\pm$ (syst) (muon) | $\sigma \cdot B$ (pb) (std. str.) | $\sigma \cdot B$ (pb) (electron) | $\sigma \cdot B$ (pb) (muon) | $\sigma \cdot B$ (pb) (combined) |
|---|---|---|---|---|---|---|
| 85 | $0.079^{+0.100}_{-0.078} \pm 0.093$ | $0^{+0.025}_{-0} \pm 0.023$ | 1490 | $< 480$ | $< 270$ | $< 260$ |
| 90 | $0^{+0.011}_{-0} \pm 0.008$ | $0^{+0.012}_{-0} \pm 0.005$ | 1260 | $< 69$ | $< 82$ | $< 46$ |
| 100 | $0^{+0.004}_{-0.000} \pm 0.004$ | $0^{+0.008}_{-0.000} \pm 0.024$ | 920 | $< 20$ | $< 57$ | $< 20$ |
| 125 | $0^{+0.003}_{-0.000} \pm 0.001$ | $0.017^{+0.021}_{-0.017} \pm 0.022$ | 460 | $< 6.5$ | $< 36$ | $< 7.4$ |
| 150 | $0^{+0.003}_{-0.000} \pm 0.001$ | $0.028^{+0.025}_{-0.020} \pm 0.022$ | 260 | $< 3.6$ | $< 25$ | $< 4.4$ |
| 175 | $0^{+0.004}_{-0} \pm 0.001$ | $0.017^{+0.030}_{-0.017} \pm 0.022$ | 156 | $< 3.0$ | $< 15$ | $< 3.4$ |
| 200 | $0^{+0.010}_{-0.000} \pm 0.003$ | $0^{+0.060}_{-0.000} \pm 0.016$ | 98 | $< 3.0$ | $< 10$ | $< 3.0$ |
| 250 | $0^{+0.012}_{-0} \pm 0.003$ | $0^{+0.040}_{-0} \pm 0.005$ | 43 | $< 2.3$ | $< 5.8$ | $< 1.9$ |
| 300 | $0^{+0.018}_{-0.000} \pm 0.002$ | $0^{+0.037}_{-0.000} \pm 0.002$ | 21 | $< 2.0$ | $< 4.2$ | $< 1.5$ |
| 350 | $0^{+0.030}_{-0} \pm 0.002$ | $0^{+0.059}_{-0} \pm 0.001$ | 11 | $< 1.9$ | $< 3.7$ | $< 1.3$ |
| 400 | $0^{+0.056}_{-0.000} \pm 0.002$ | $0^{+0.105}_{-0.000} \pm 0.002$ | 5.6 | $< 1.9$ | $< 3.4$ | $< 1.3$ |
| 450 | $0^{+0.101}_{-0} \pm 0.002$ | $0^{+0.200}_{-0} \pm 0.002$ | 3.0 | $< 1.8$ | $< 3.5$ | $< 1.3$ |
| 500 | $0^{+0.188}_{-0.000} \pm 0.001$ | $0^{+0.389}_{-0.000} \pm 0.002$ | 1.6 | $< 1.8$ | $< 3.8$ | $< 1.3$ |

The result of this thesis excludes a $W'$ with standard-strength couplings with a mass less than 520 GeV. However, it is simple to obtain $W'$ mass limits for models in which the couplings are other than what we have called standard-strength. One can simply calculate the nominal $W'$ cross section times leptonic branching ratio for the new model, and overlay this curve with our limit. The new mass limit is the point where the curves intersect. This is possible because our limits apply to any spin-1 particle that decays into an electron or muon and a light, stable neutrino, and couples to light quarks though a CKM matrix that is essentially diagonal.

## 8.5 Future Prospects

May you live in interesting times.

—Chinese Curse

As this thesis was being written, a new collider run was underway at Fermilab. During this run, known as Run IA, CDF is hoping to record 25 $pb^{-1}$ of data, six times more than was recorded in 1988–89. During future collider runs, the luminosity is expected to rise even more. Run IB, scheduled to begin in mid- to late 1993, is hoped to deliver 75–100 $pb^{-1}$. Run II, tentatively scheduled for 1995, may result in several hundred additional $pb^{-1}$. And with the arrival of the Main Injector in the late 1990's, integrated luminosities of 1 $fb^{-1}$ may be possible. With these kinds of integrated luminosities, the range of the $W'$ search will be expanded considerably. Figure 69 shows the prospective $W'$ limit versus integrated luminosity. In the Main Injector era, the $W'$ limit could approach 1 TeV, although to achieve this kind of a limit a great deal of effort will be required, especially in understanding the response of the calorimeters to very high energy electrons.

Thus, the data on which our result is based is only a small fraction of what will become available over the next decade. Although CDF is now a very mature

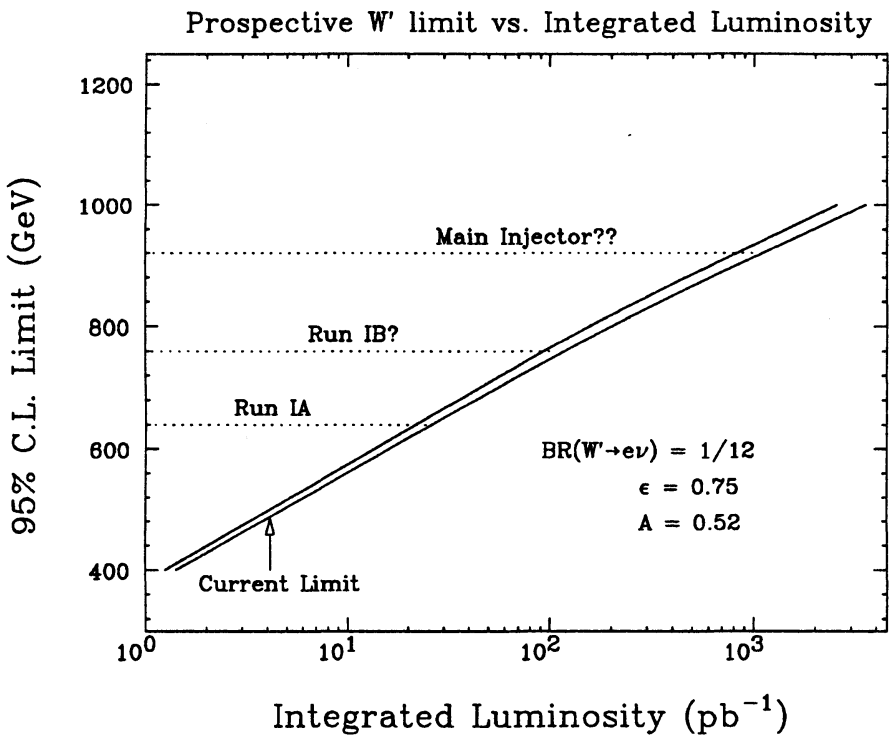


Figure 69. Prospective $W'$ limit versus integrated luminosity.

experiment, in a sense the collider program at Fermilab is still in its infancy. The coming years promise to be an exciting time of search and discovery.

*The end of a thing is better than the beginning...*

—Ecclesiastes

# APPENDIX A

# A WORD ON JET CORRECTIONS

Some 40% of the $W$'s produced at CDF are produced in conjunction with one or more hadronic jets. Jets can complicate the missing-$E_T$ measurement, from which we infer the momentum of the neutrino, because of several effects:

1. Jets are extended objects, and the CDF calorimeter is not hermetic. Particles can go down cracks and other uninstrumented regions, causing the energy of the jet to be underestimated.

2. The CDF calorimeter is neither compensating nor completely linear. This means that the response is different for electromagnetic and hadronic particles of the same energy, and the response is different for a 5 GeV pion than for a 50 GeV pion. (The former actually deposits less than 1/10 the energy of the latter.) Because a parton of a given initial energy can fragment into a variety of final states, with differing numbers of particles and particle energies, it is difficult to reconstruct the energy of the primary parton from the observed energy of the jet.

3. Even without the above two effects, there would still be uncertainties in the jet energy measurement due to the nature of the CDF jet-clustering algorithm. The algorithm[75] includes all energy in a cone of size 0.7 in $\eta$-$\phi$ space, surrounding the $E_T$-weighted centroid of the cluster. Thus, particles from the initial parton that fall outside the cone are not included in the measurement, while unrelated energy from the underlying event is included.

It is possible to correct for all of these effects on a statistical basis. Through the use of dijet and jet-photon balancing studies, the QCD group within CDF has developed a "jet correction" procedure[75] that *on average* results in an improved measurement of jet energies. When the $W'$ analysis was in its later stages, the question arose[76] of whether or not we should be using corrected jet energies in our calculation of the $\not{E}_T$. (Throughout the analysis we had used the observed jet energies.) We argue here that the use of jet corrections is likely to result in a somewhat improved $W'$ limit in the range $M_{W'} \lesssim 125$ GeV, i.e. in the tail of the $W$ transverse mass distribution, where events may move around as a result of jet corrections. But we will also argue that jet corrections have no effect in the high-mass range that is of the greatest interest in this analysis.

We begin with the obvious remark that the limit in the high mass region will not be affected by jet corrections if new events do not appear in this region when the corrections are applied. The highest transverse mass events are at 185 GeV in the electron channel and 205 GeV in the muon channel. If, after jet corrections, new events move into this region, or if these events move to even higher transverse mass, the limit there will become less stringent as the fitter attributes the new events to $W'$ production.

Before we actually apply the corrections, let us estimate the transverse mass resolution we can expect in the electron and muon samples. The transverse mass is

$$\begin{aligned} M_T &= \sqrt{2E_T\not{E}_T(1-\cos\Delta\phi^{l\text{-}\nu})} \\ &\simeq 2\sqrt{E_T\not{E}_T}. \end{aligned}$$

So,

$$\begin{aligned}\sigma_{M_T} &\simeq \sigma_{E_T}\sqrt{\frac{\not{E}_T}{E_T}} \oplus \sigma_{\not{E}_T}\sqrt{\frac{E_T}{\not{E}_T}} \\ &\simeq \sigma_{E_T} \oplus \sigma_{\not{E}_T},\end{aligned}$$

where the $\oplus$ indicates that the two terms are to be added in quadrature. Now, $\sigma_{E_T}$ comes from the measurement (in the CEM for electrons and CTC for muons) of the primary lepton:

$$\begin{aligned}\sigma_{E_T} &= 13.5\%\sqrt{E_T} \oplus 2\% \qquad \text{(electron)} \\ \sigma_{P_T} &= 0.11\% P_T^2 \qquad \text{(muon).}\end{aligned}$$

The missing-$E_T$ resolution, $\sigma_{\not{E}_T}$, is determined by the rest of the event, including the jets (if any) and the underlying event. Typically[77] (before corrections),

$$\begin{aligned}\sigma_{\not{E}_T} &\simeq 0.5\sqrt{\sum E_T} \\ &\simeq \text{a few GeV},\end{aligned}$$

where the sum under the square root is over all scalar $E_T$ in the event other than that of the primary lepton. For electrons, the transverse mass resolution is therefore expected to be 3-5 GeV over the entire mass range of interest, while for muons the transverse mass resolution is approximated by $3 \times 10^{-4} M_{W'}^2$. The worsening transverse mass resolution at high mass (for $M_{W'} = 400$ GeV the resolution in the muon channel is roughly 50 GeV) is a result of the lower momentum resolution for high-momentum tracks, but is not related to jets or the underlying event. This effect can be seen by comparing Figures 56 and 57. For typical $W$ events, the transverse mass resolution in both channels is of order a few GeV.

Thus, we expect that most events should not move in transverse mass by more than this amount when jet corrections are applied. Typically we expect $\Delta M_T < 0$, since in the common process where an electron or muon recoils against a jet, we underestimate the energy of the jet and hence overestimate the $\not{E}_T$.

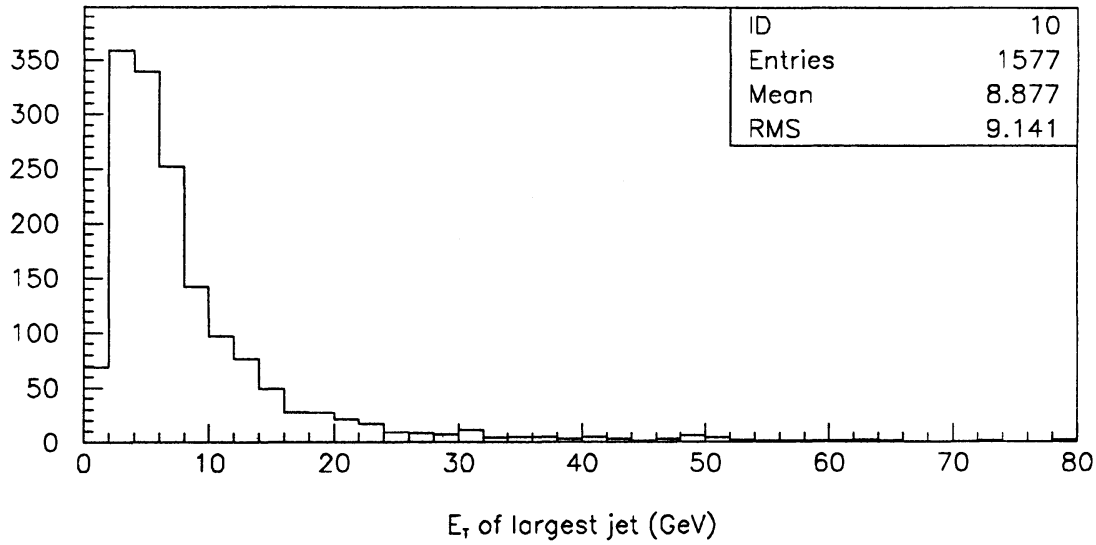


Figure 70. Uncorrected energy of the highest-$E_T$ jet for events in the electron sample.

To investigate this, we corrected the jets and unclustered energy according to the following procedure:

1. Jets with uncorrected $E_T$ greater than 15 GeV were corrected using the jet correction routine QDJSCO.

2. Jets with $E_T$ less than 15 GeV, as well as unclustered energy, were scaled up by a factor of 1.4. (This is the average energy correction factor returned by QDJSCO. However, QDJSCO was not tuned on jets with $E_T < 20$ GeV, so it is probably not reliable to apply the routine to jets much lower than 15 GeV.)

We then remade the analysis samples by cutting on the new $\not{E}_T$. Figure 70 shows the uncorrected energy of the highest-$E_T$ jet for events in the electron sample. Most jets have $E_T < 10$ GeV, but there is a tail of higher-$E_T$ jets, and these have the greatest potential to affect the $\not{E}_T$ measurement. QDJSCO returns a correction factor for each jet; a plot of the correction factor versus the detector $\eta$ centroid of the jet is

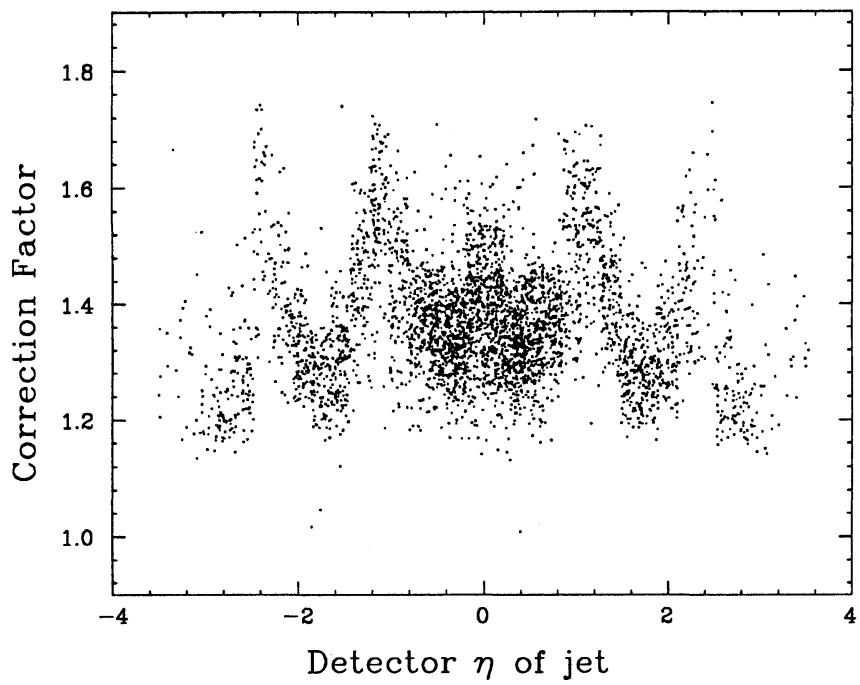


Figure 71. Jet correction factor from QDJSCO versus jet $\eta$. Jets near regions with cracks receive a higher correction factor.

shown in Figure 71. Clearly visible are the higher correction factors for jets near the 90° crack, and near the cracks between the central and plug, and plug and forward, calorimeters. The difference in transverse mass before and after corrections is shown for the electron sample in Figure 72. The *rms* of this distribution is less than 3 GeV, consistent with the rough calculation above. The average event goes down in $M_T$ by something less than 1 GeV, with a tail extending toward lower values. The change in transverse mass depends on the total $E_T$ in the rest of the event, as shown in Figure 73. Events with a lot of jet activity usually get a bigger change, and the result of the correction is usually to lower the transverse mass. This is especially true of events whose transvese mass changes by the greatest amount. No event in the electron sample goes up in transverse mass by more than 8 GeV. Figures 74 and 75 show the same plots for the muon sample, where we reach similar conclusions.

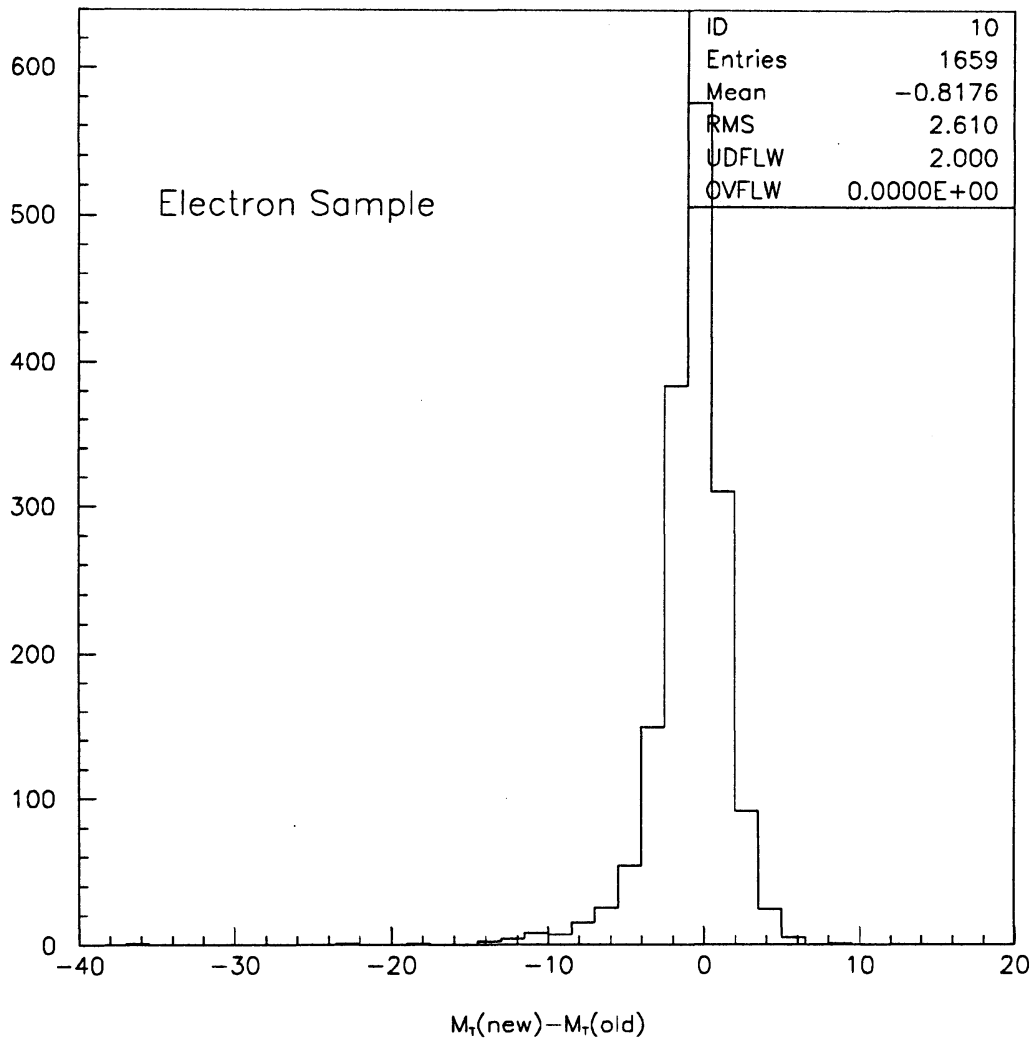


Figure 72. Difference in $M_T$ (GeV) for events in the electron sample before and after jet and underlying event corrections.

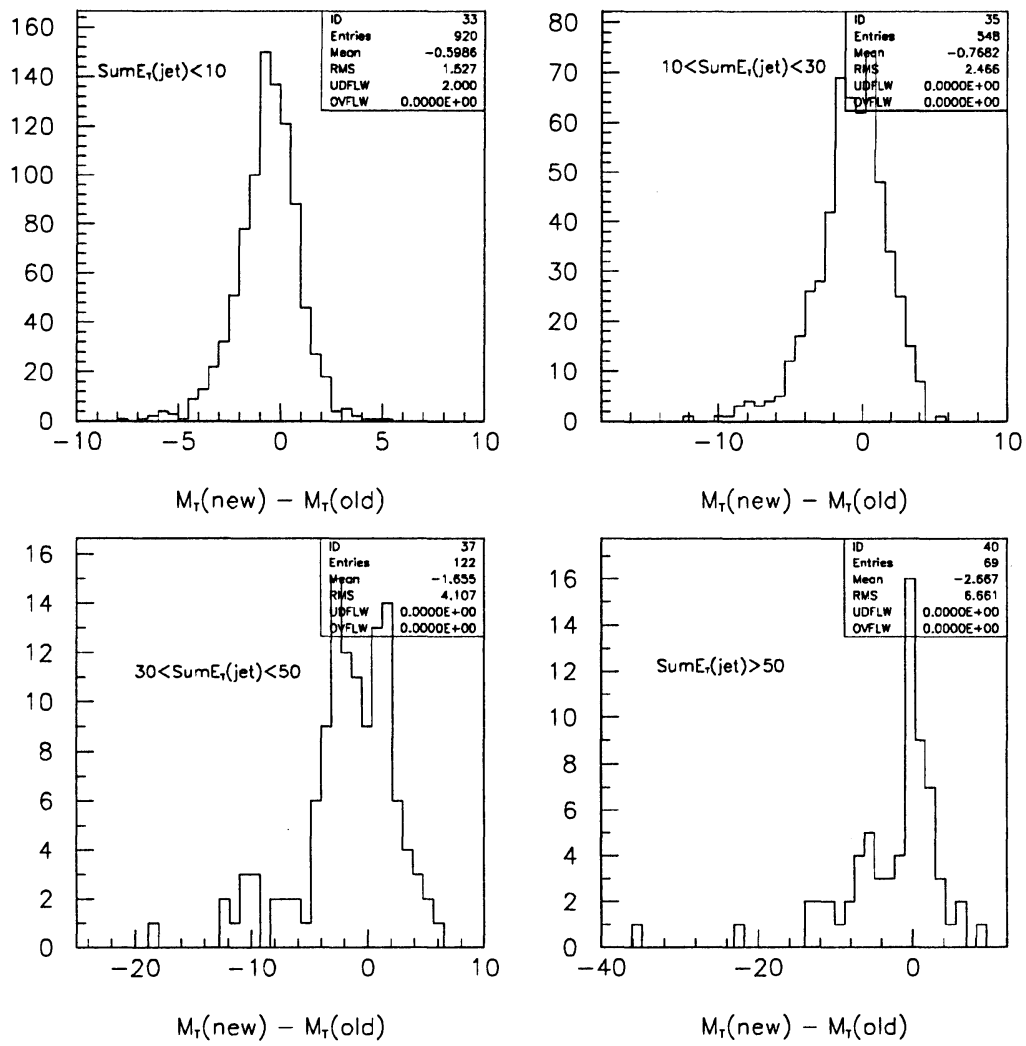


Figure 73. Difference in $M_T$ (GeV) for events in the electron sample before and after corrections, for various intervals of uncorrected $\sum E_T(jet)$.

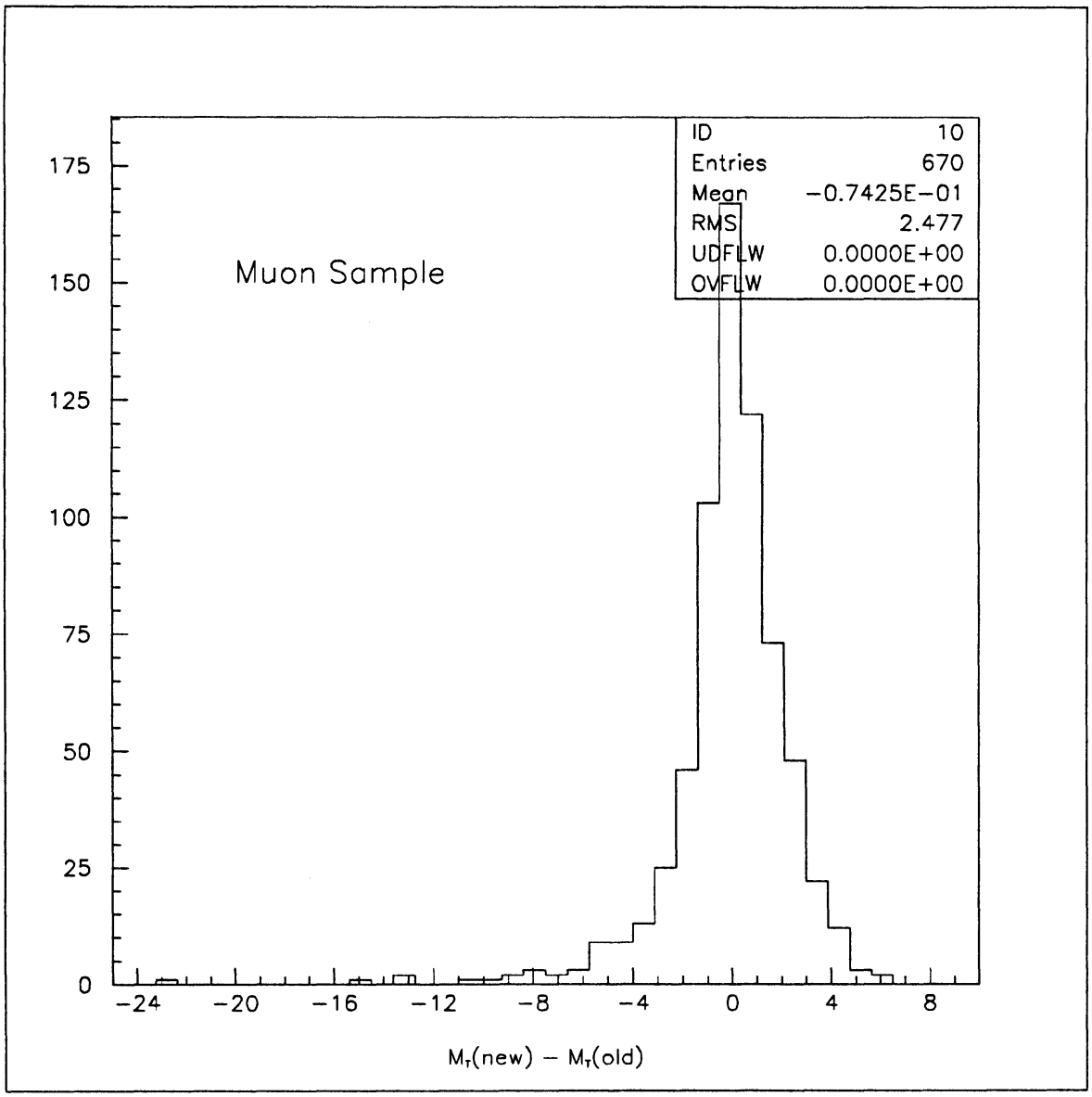


Figure 74. Difference in $M_T$ (GeV) for events in the muon sample before and after jet and underlying event corrections.

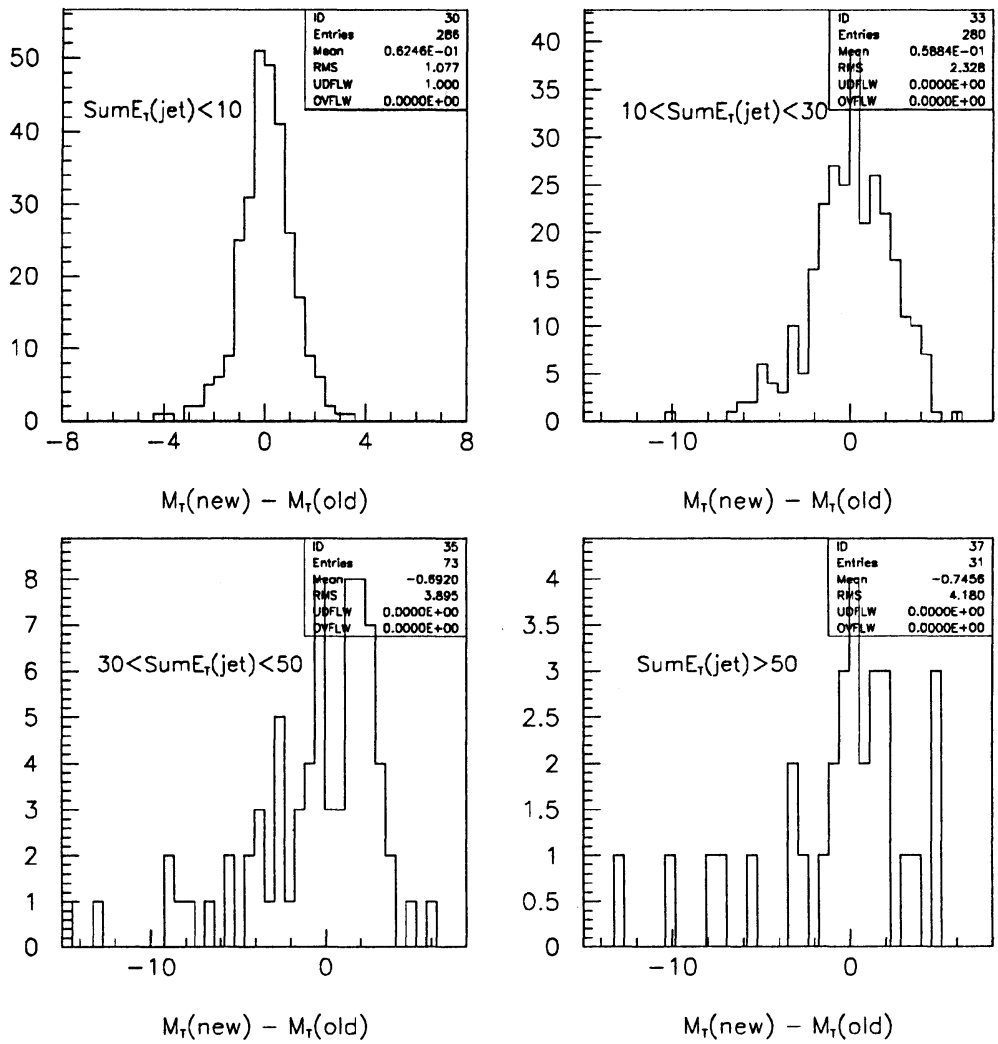


Figure 75. Difference in $M_T$ (GeV) for events in the muon sample before and after corrections, for various intervals of uncorrected $\sum E_T(jet)$.

Finally, in Figures 76 and 77, we compare the transverse mass distributions for the electron and muon samples before and after the corrections. Perhaps somewhat surprisingly, the highest transverse mass events in both samples do not move by very much. The general effect of the corrections is to make the tail of the transverse mass distributions fall more rapidly. In particular, we note that the hint of a peak in the tail of the muon sample—which caused us such concern in Chapter 5 and which the fitter persistently attributed to $W'$ production—has largely disappeared after the corrections. Note that there are fewer events in the corrected samples. This is because, as mentioned above, the effect of jet corrections is often to lower the $\not{E}_T$; hence fewer events pass the 30 GeV $\not{E}_T$ cut.

From the fact that no new events appear at high $M_T$ after the corrections, we conclude that the $W'$ limit in this region would be unchanged. In particular, our combined limit of $M_{W'} > 520$ GeV is unaffected. However, the tail of the $W$ $M_T$ distribution sharpens up somewhat after corrections, and this should lead to a better separation of the $W$ and $W'$ signals in the region $M_{W'} \lesssim 125$ GeV. We expect that the limit in this region would therefore improve if the analysis were redone using corrected jets.

But if one were really interested in setting the best possible $W'$ limit in this low-mass regime, a different approach is probably better. One should simply impose a no-jet cut (as was done in the CDF $W$ mass measurement[77]) to sharpen the transverse mass distributions even more and avoid the messy issue of jet corrections entirely.

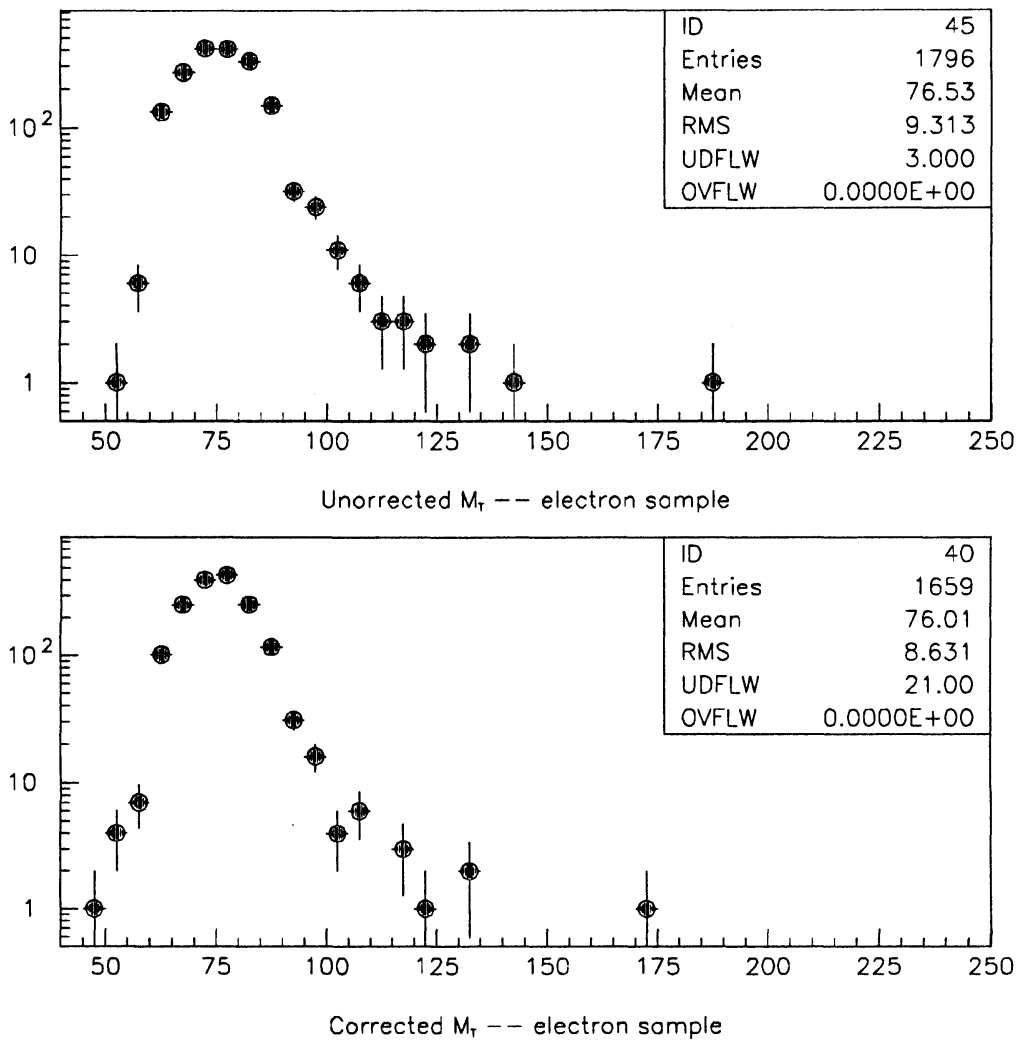


Figure 76. Comparison of $M_T$ distributions for the electron sample before and after jet and underlying event corrections.

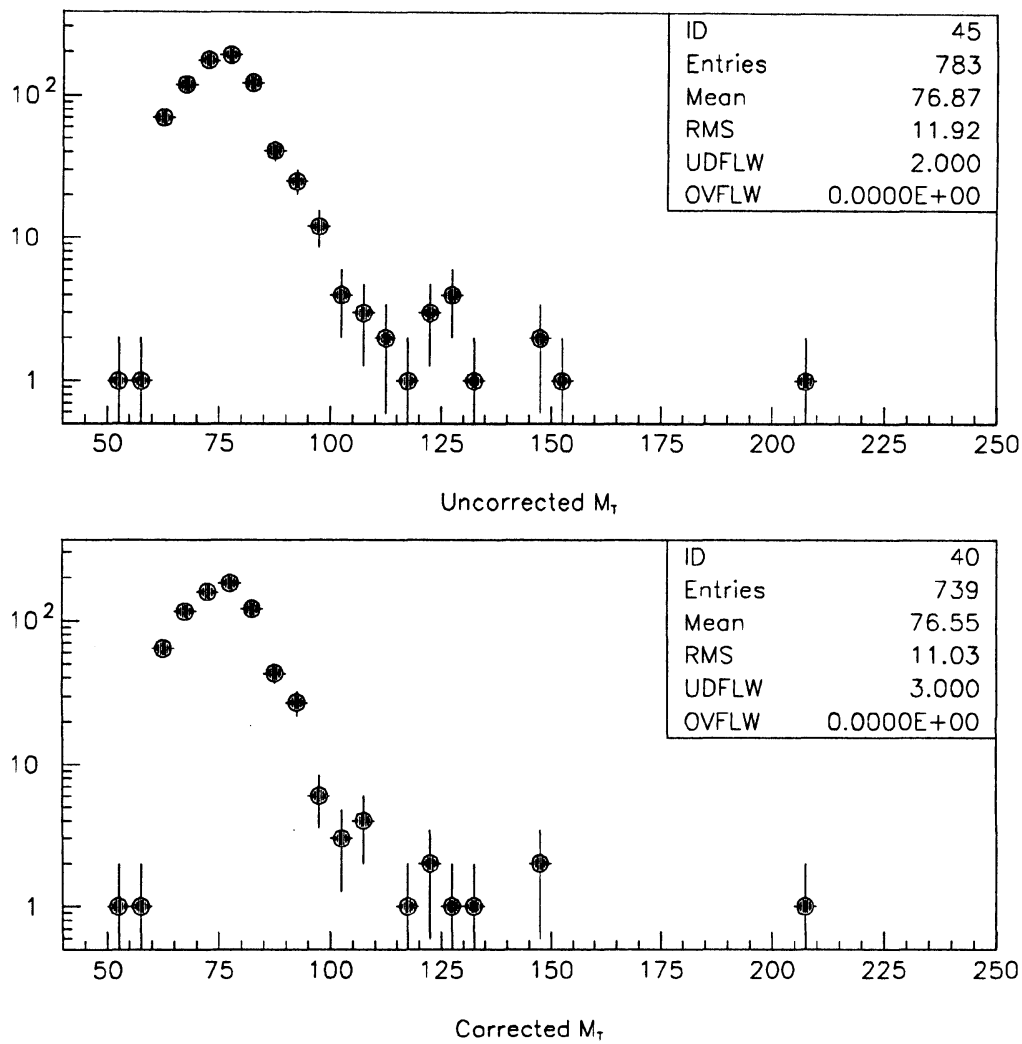


Figure 77. Comparison of $M_T$ distributions for the muon sample before and after jet and underlying event corrections.

# APPENDIX B

# Text of the $W'$ Paper in Physical Review Letters

# Search for $W' \to e\nu$ and $W' \to \mu\nu$ in $\bar{p}p$ Collisions at $\sqrt{s} = 1.8$ TeV

F. Abe,[9] D. Amidei,[4] G. Apollinari,[16] M. Atac,[4] P. Auchincloss,[15] A. R. Baden,[6] N. Bacchetta,[11] M. W. Bailey,[14] A. Bamberger,[4,a] B. A. Barnett,[8] A. Barbaro-Galtieri,[10] V. E. Barnes,[14] T. Baumann,[6] F. Bedeschi,[13] S. Behrends,[2] S. Belforte,[13] G. Bellettini,[13] J. Bellinger,[21] J. Bensinger,[2] A. Beretvas,[4] J. P. Berge,[4] S. Bertolucci,[5] S. Bhadra,[7] M. Binkley,[4] R. Blair,[1] C. Blocker,[2] V. Bolognesi,[13] A. W. Booth,[4] C. Boswell,[8] G. Brandenburg,[6] D. Brown,[6] E. Buckley-Geer,[17] H. S. Budd,[15] G. Busetto,[11] A. Byon-Wagner,[4] K. L. Byrum,[21] C. Campagnari,[3] M. Campbell,[3] R. Carey,[6] W. Carithers,[10] D. Carlsmith,[21] J. T. Carroll,[4] R. Cashmore,[4,a] A. Castro,[11] F. Cervelli,[13] K. Chadwick,[4] G. Chiarelli,[5] W. Chinowsky,[10] S. Cihangir,[4] A. G. Clark,[4] D. Connor,[12] M. Contreras,[2] J. Cooper,[4] M. Cordelli,[5] D. Crane,[4] M. Curatolo,[5] C. Day,[4] F. DeJongh,[4] S. Dell'Agnello,[13] M. Dell'Orso,[13] L. Demortier,[2] B. Denby,[4] P. F. Derwent,[3] T. Devlin,[17] D. DiBitonto,[18] R. B. Drucker,[10] S. Edner,[3] J. E. Elias,[4] R. Ely,[10] S. Eno,[3] S. Errede,[7] B. Esposito,[5] B. Flaugher,[4] G. W. Foster,[4] M. Franklin,[6] J. Freeman,[4] H. Frisch,[3] T. Fuess,[4] Y. Fukui,[9] Y. Funayama,[19] A. F. Garfinkel,[14] A. Gauthier,[7] S. Geer,[4] D. W. Gerdes,[3] P. Giannetti,[13] N. Giokaris,[16] P. Giromini,[5] L. Gladney,[12] M. Gold,[10] K. Goulianos,[16] H. Grassmann,[13] C. Grosso-Pilcher,[3] C. Haber,[10] S. R. Hahn,[4] R. Handler,[21] K. Hara,[19] R. M. Harris,[4] J. Hauser,[4] C. Hawk,[17] T. Hessing,[18] R. Hollebeek,[12] L. Holloway,[7] P. Hu,[17] B. Hubbard,[10] B. T. Huffman,[14] R. Hughes,[12] P. Hurst,[5] J. Huth,[4] M. Incagli,[13] T. Ino,[19] H. Iso,[19] H. Jensen,[4] C. P. Jessop,[6] R. P. Johnson,[4] U. Joshi,[4] R. W. Kadel,[10] T. Kamon,[18] S. Kanda,[19] D. A. Kardelis,[7] I. Karliner,[7] E. Kearns,[6] L. Keeble,[18] R. Kephart,[4] P. Kesten,[2] R. M. Keup,[7] H. Keutelian,[4] D. Kim,[4] S. Kim,[19] L. Kirsch,[2] K. Kondo,[19] J. Konigsberg,[6] E. Kovacs,[4] S. E. Kuhlmann,[1] E. Kuns,[17] A. T. Laasanen,[14] J. I. Lamoureux,[21] S. Leone,[13] W. Li,[1] T. M. Liss,[7] N. Lockyer,[12] C. B. Luchini,[7] P. Lukens,[4] P. Maas,[21] M. Mangano,[13] J. P. Marriner,[4] M. Mariotti,[13] R. Markeloff,[21] L. A. Markosky,[21] R. Mattingly,[2] P. McIntyre,[18] A. Menzione,[13] T. Meyer,[18] S. Mikamo,[9] M. Miller,[3] T. Mimashi,[19] S. Miscetti,[5] M. Mishina,[9] S. Miyashita,[19] Y. Morita,[19] S. Moulding,[2] J. Mueller,[17] A. Mukherjee,[4] L. F. Nakae,[2] I. Nakano,[19] C. Nelson,[4] C. Newman-Holmes,[4] J. S. T. Ng,[6] M. Ninomiya,[19] L. Nodulman,[1] S. Ogawa,[19] R. Paoletti,[13] A. Para,[4] E. Pare,[6] J. Patrick,[4] T. J. Phillips,[6] R. Plunkett,[4] L. Pondrom,[21] J. Proudfoot,[1] G. Punzi,[13] D. Quarrie,[4] K. Ragan,[12] G. Redlinger,[3] J. Rhoades,[21] M. Roach,[20] F. Rimondi,[4,a] L. Ristori,[13] T. Rohaly,[12] A. Roodman,[3] W. K. Sakumoto,[15] A. Sansoni,[5] R. D. Sard,[7] A. Savoy-Navarro,[4] V. Scarpine,[7] P. Schlabach,[7] E. E. Schmidt,[4] M. H. Schub,[14] R. Schwitters,[6] A. Scribano,[13] S. Segler,[4] Y. Seiya,[19] M. Sekiguchi,[19] M. Shapiro,[10] N. M. Shaw,[14] M. Sheaff,[21] M. Shochet,[3] J. Siegrist,[10] P. Sinervo,[12] J. Skarha,[8] K. Sliwa,[20] D. A. Smith,[13] F. D. Snider,[8] L. Song,[12] R. St. Denis,[6] A. Stefanini,[13] G. Sullivan,[3] R. L. Swartz, Jr.,[7] M. Takano,[19] F. Tartarelli,[13] K. Takikawa,[19] S. Tarem,[2] D. Theriot,[4] M. Timko,[18] P. Tipton,[4] S. Tkaczyk,[4] A. Tollestrup,[4] J. Tonnison,[14] W. Trischuk,[6] N. Turini,[13] Y. Tsay,[3] F. Ukegawa,[19] D. Underwood,[1] S. Vejcik, III,[8] R. Vidal,[4] R. G. Wagner,[1] R. L. Wagner,[4] N. Wainer,[4] J. Walsh,[12] T. Watts,[17] R. Webb,[18] C. Wendt,[21] H. Wenzel,[13] W. C. Wester, III,[10] T. Westhusing,[13] S. N. White,[16] A. B. Wicklund,[1] H. H. Williams,[12] B. L. Winer,[15] J. Wyss,[11] A. Yagil,[4] A. Yamashita,[19] K. Yasuoka,[19] G. P. Yeh,[4] J. Yoh,[4] M. Yokoyama,[19] J. C. Yun,[4] A. Zanetti,[13] F. Zetti,[13] and S. Zucchelli[13]

(CDF Collaboration)

[1]*Argonne National Laboratory, Argonne, Illinois 60439*
[2]*Brandeis University, Waltham, Massachusetts 02254*
[3]*University of Chicago, Chicago, Illinois 60637*
[4]*Fermi National Accelerator Laboratory, Batavia, Illinois 60510*
[5]*Laboratori Nazionali di Frascati, Istituto Nazionale di Fisica Nucleare, Frascati, Italy*
[6]*Harvard University, Cambridge, Massachusetts 02138*
[7]*University of Illinois, Urbana, Illinois 61801*
[8]*The Johns Hopkins University, Baltimore, Maryland 21218*
[9]*National Laboratory for High Energy Physics (KEK), Tsukuba, Ibaraki 305, Japan*
[10]*Lawrence Berkeley Laboratory, Berkeley, California 94720*

© 1991 The American Physical Society

[11]Istituto Nazionale di Fisica Nucleare, Sezione di Padova, I-35131 Padova, Italy
[12]University of Pennsylvania, Philadelphia, Pennsylvania 19104
[13]Istituto Nazionale di Fisica Nucleare, University and Scuola Normale Superiore of Pisa, I-56100 Pisa, Italy
[14]Purdue University, West Lafayette, Indiana 47907
[15]University of Rochester, Rochester, New York 14627
[16]Rockefeller University, New York, New York 10021
[17]Rutgers University, Piscataway, New Jersey 08854
[18]Texas A&M University, College Station, Texas 77843
[19]University of Tsukuba, Tsukuba, Ibaraki 305, Japan
[20]Tufts University, Medford, Massachusetts 02155
[21]University of Wisconsin, Madison, Wisconsin 53706
(Received 29 July 1991)

The $W'$ is a charged, heavy, vector boson predicted to exist by some extensions of the standard model. We have searched for the processes $W' \to e\nu$ and $W' \to \mu\nu$ for $M_{W'} > 100$ GeV/$c^2$, in $\bar{p}p$ collisions at $\sqrt{s} = 1.8$ TeV, using data taken with the Collider Detector at Fermilab. The nonobservation of these processes leads to a lower limit of 520 GeV/$c^2$ (95% confidence level) on the mass of the $W'$, assuming standard-strength couplings to three fermion generations.

PACS numbers: 13.85.Rm, 12.15.Cc, 14.80.Er

The $W'$ is a charged, heavy ($M_{W'} > M_W$), vector boson that appears in certain attempts to enlarge the $SU(2)_L \times U(1)_Y$ gauge group of the standard model. Left-right symmetric models [1], for example, feature a right-handed SU(2) and corresponding new gauge bosons, including a heavy, right-handed $W'$, denoted $W_R$. Previous direct searches [2] for the process $W' \to e\nu$ in $\bar{p}p$ collisions have set a lower limit of 220 GeV/$c^2$ (90% confidence level) on the $W'$ mass, assuming standard couplings to fermions. A variety of experiments [3] have searched for a right-handed charged-current interaction by looking for departures from the expected $V-A$ angular distribution in polarized muon decay. In this way a lower limit of 450 GeV/$c^2$ (90% confidence level) was obtained for the mass of the $W_R$, assuming a light right-handed neutrino ($m_{\nu_R} \lesssim 10$ MeV/$c^2$). We have searched for the processes $W' \to e\nu$ and $W' \to \mu\nu$ for $M_{W'} > 100$ GeV/$c^2$, in $\bar{p}p$ collisions at a center-of-mass energy $\sqrt{s} = 1.8$ TeV, using data taken with the Collider Detector at Fermilab (CDF) during the 1988–1989 Tevatron Collider run. The signature of these processes is a high-$P_T$ lepton together with missing energy from the neutrino. The analysis presented below applies to both left- and right-handed $W'$'s provided that the associated neutrino is not too heavy ($m_{\nu_R} \lesssim 15$ GeV/$c^2$) and does not decay to observable particles before exiting the detector.

The CDF has been described in detail elsewhere [4]. Here we give a brief description of the components relevant to this analysis. The location of the event vertex is determined to within 1 mm along the beam direction using a vertex time projection chamber. The momenta of charged particles are measured in the central tracking chamber (CTC), which is immersed in a 1.4-T axial magnetic field and has a resolution of $\delta P_T/P_T = 0.0011 P_T$, where the transverse momentum $P_T$ is expressed in GeV/$c$ and the track is constrained to pass through the event vertex. Outside the CTC, electromagnetic and hadronic calorimeters, arranged in a projective tower geometry, cover the pseudorapidity region $|\eta| < 4.2$ [where $\eta = -\ln\tan(\theta/2)$ and $\theta$ is the polar angle with respect to the direction of the proton beam], allowing reliable measurements of the imbalance in transverse energy ($E_T = E\sin\theta$) due to the undetected neutrino in $W$ or $W'$ boson decay. In the central region ($|\eta| < 1.1$), the electromagnetic and hadronic calorimeters are organized in projective towers of size $\delta\eta \times \delta\phi = 0.1 \times 15°$. The central electromagnetic calorimeter, on which the electron portion of this analysis is based, provides an energy resolution $\sigma_{E_T}/E_T$ of $(13.5\%/E_T^{1/2}) \pm 2\%$. Outside the calorimeters, at a radius of 3.5 m, drift chambers in the region $|\eta| < 0.61$ provide muon identification.

Events for this measurement were collected using inclusive electron and muon triggers. The electron trigger required an energy cluster in the central electromagnetic calorimeter with $E_T > 12$ GeV, together with an associated CTC track with transverse momentum $P_T > 6$ GeV/$c$. The ratio of hadronic to electromagnetic energy in the cluster (HAD/EM) was required to be less than 12.5%. This trigger was measured to be $(97.3 \pm 0.5)\%$ efficient for electrons with $15 < E_T \lesssim 150$ GeV [5]. Very-high-$E_T$ electrons ($E_T \gtrsim 150$ GeV) may exceed the single-tower dynamic range and lead to trigger inefficiency. For such events, a trigger requiring only a calorimeter energy cluster with $E_T > 60$ GeV was available, ensuring nearly full trigger efficiency at high $E_T$. The muon trigger required a match between a CTC track with $P_T > 9$ GeV/$c$ and a track segment in the muon chambers. This trigger was measured to be $(91 \pm 2)\%$ efficient for muons with $P_T > 20$ GeV/$c$.

From events passing the above triggers, we have selected electron and muon events with cuts designed to remain very efficient for high-$P_T$ leptons. Electron candidates were required to be in a fiducial region of the central electromagnetic calorimeter and to have HAD/EM $< 10\%$. In addition, the ratio of the calorimeter energy $E$ to the track momentum $P$ was required to be less than

2. An algorithm was applied to reject electrons coming from photon conversions [6]. Muon candidates were required to have an energy deposition in the calorimeters characteristic of a minimum-ionizing particle. A cut on the impact parameter of the track relative to the beam position was used to reject muons coming from the decay in flight of pions and kaons. Muon tracks were also required to pass quality cuts and to extrapolate to a fiducial region of the muon chambers. Cosmic rays were rejected with a filter determined to be over 99% efficient for real, primary muons with $P_T > 20$ GeV/$c$. Both electron and muon candidates were required to have less than 5 GeV of $E_T$ in the neighboring calorimeter towers. This cut reduces background from nonisolated particles in jets that may fake a high-$P_T$ lepton. Events were also rejected if there existed a second electromagnetic cluster (for electron events) or track (for muon events) whose invariant mass with the first lepton was within 25 GeV/$c^2$ of the $Z^0$ mass. The combined efficiency of the electron identification cuts is $0.88 \pm 0.04$ for electrons typical of $W$ decay, and falls to $0.75 \pm 0.04$ for 250-GeV electrons due to increased bremsstrahlung (which lowers the $E/P$ and isolation efficiencies) and greater leakage of the electromagnetic shower into the hadronic calorimeter (which lowers the HAD/EM efficiency). The combined efficiency of the muon identification cuts is $0.75 \pm 0.06$, and is independent of $P_T$ for $P_T > 20$ GeV/$c$.

In addition to the above identification cuts, electrons were required to have cluster $E_T > 30$ GeV, and muons were required to have track $P_T > 30$ GeV/$c$. The missing transverse energy ($\not{E}_T$), defined as the magnitude of the vector sum of transverse energy over all calorimeter towers in the region $|\eta| < 3.6$, was required to be greater than 30 GeV. In muon events, the calorimeter energy of the muon was removed and the $\not{E}_T$ was recalculated to account for the muon $P_T$. The electron sample contains 1796 events in an integrated luminosity of $4.15 \pm 0.28$ pb$^{-1}$, and the muon sample contains 783 events in $3.54 \pm 0.24$ pb$^{-1}$. The acceptance, including all fiducial and kinematic cuts, was determined from Monte Carlo studies to be 23% for electrons and 13% for muons from $W$ decay. The acceptance rises quickly to 55% for electrons and 34% for muons from higher-mass $W'$s ($M_{W'} \gtrsim 200$ GeV/$c^2$), whose decay leptons are more likely to be in the central rapidity region and less likely to fail the $E_T$ and $\not{E}_T$ cuts. The acceptance uncertainty was determined to be $\pm 1\%$ in all cases.

For each event, we form the transverse mass, $M_T = [2E_T\not{E}_T(1-\cos\phi^{l\nu})]^{1/2}$, where $\phi^{l\nu}$ is the angle in the azimuthal plane between the lepton vector and the missing energy vector. The transverse mass resolution $\sigma_{M_T}$ is $\sim 3\times 10^{-4} M_{W'}^2$ in the muon channel, with $M_{W'}$ in GeV/$c^2$. In the electron channel, $\sigma_{M_T}$ is 3–5 GeV/$c^2$ and is independent of $M_{W'}$ over the mass range of this search. The $M_T$ distribution should show a Jacobian peak near the mass of any heavy object that decays to an electron or muon plus a neutrino. Backgrounds at high $M_T$ from other electroweak processes, such as $W \to \tau\nu$ and $Z^0$ decay in which one lepton was lost, were determined to be less than 0.1 event. Two-jet events in which one jet fakes a lepton, while the balancing jet is poorly measured resulting in substantial $\not{E}_T$, contribute less than 3 events to each sample. Residual cosmic rays contribute $3 \pm 2$ events by the muon sample. The $M_T$ distributions for the electron and muon samples are shown in Fig. 1, together with a Monte Carlo prediction for $W$ boson decay (see below). The data are well described by $W$ production and decay alone. The highest transverse mass events are at 185 GeV/$c^2$ in the electron channel and 205 GeV/$c^2$ in the muon channel.

To search for a $W'$ signal, we have generated Monte Carlo transverse mass distributions $W'(M_T)$ for a variety of $W'$ masses, and have performed a binned likelihood fit of the observed transverse mass spectrum by the superposition

$$\frac{dN}{dM_T^{\rm obs}} = \alpha W'(M_T) + \beta W(M_T),$$

where $W(M_T)$ is the Monte Carlo $M_T$ distribution for $W$ decay. Throughout the fit, the $W'$ fraction $\alpha$ was constrained to be non-negative. The Monte Carlo distribution generated $W$ and $W'$ bosons from the leading-order diagram $q\bar{q} \to W(W')$ using the HMRS(B) structure functions [7]. The leading-order cross section was multiplied by a $K$ factor of $1+(8\pi/9)\alpha_s(M_{W'}^2)$ to account for higher-order QCD effects. The $P_T$ distributions for the $W$ and $W'$ were taken from a next-to-leading-order QCD calculation [8]. The width of the $W'$ was taken to have the form $\Gamma_{W'} = (2.76\ \text{GeV}) M_{W'}/M_W$, where 2.76 GeV is

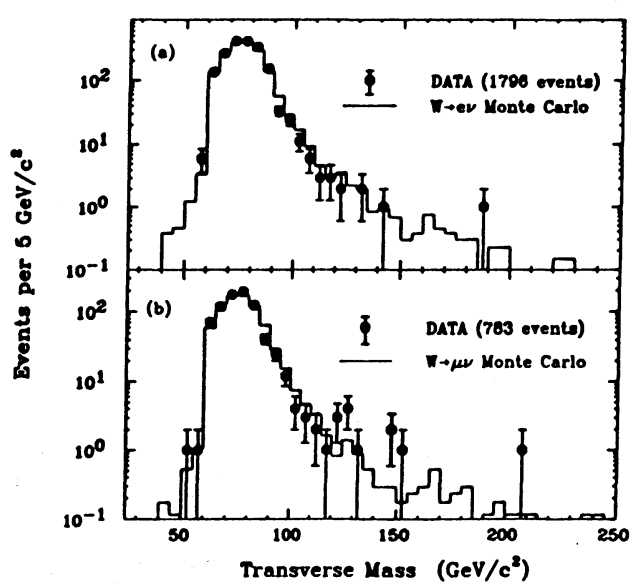


FIG. 1. Observed transverse mass distributions for the (a) electron and (b) muon samples. Error bars are statistical. Superimposed is the Monte Carlo prediction for $W$ boson decay, normalized to the $W$ fraction $\beta$ obtained from the fit.

TABLE I. The fitted $W'$ fraction $\alpha$ for the electron and muon samples, the predicted cross section times branching ratio ($\sigma B$) for standard couplings, and the 95%-confidence-level limits on the cross section times branching ratio for the electron, muon, and combined channels.

| $M_{W'}$ (GeV/$c^2$) | $\alpha \pm$ (stat) $\pm$ (syst) (electron) | $\alpha \pm$ (stat) $\pm$ (syst) (muon) | $\sigma B$ (pb) (standard strength) | $\sigma B$ (pb) (electron) | $\sigma B$ (pb) (muon) | $\sigma B$ (pb) (combined) |
|---|---|---|---|---|---|---|
| 100 | $0^{+0.004}_{-0.000} \pm 0.004$ | $0^{+0.000}_{-0.000} \pm 0.024$ | 920 | < 20 | < 57 | < 20 |
| 125 | $0^{+0.001}_{-0.000} \pm 0.001$ | $0.017^{+0.011}_{-0.011} \pm 0.022$ | 460 | < 6.5 | < 36 | < 7.4 |
| 150 | $0^{+0.001}_{-0.000} \pm 0.001$ | $0.028^{+0.025}_{-0.020} \pm 0.022$ | 260 | < 3.6 | < 25 | < 4.4 |
| 200 | $0^{+0.010}_{-0.000} \pm 0.003$ | $0^{+0.000}_{-0.000} \pm 0.016$ | 98 | < 3.0 | < 10 | < 3.0 |
| 300 | $0^{+0.010}_{-0.000} \pm 0.002$ | $0^{+0.017}_{-0.000} \pm 0.002$ | 21 | < 2.0 | < 4.2 | < 1.5 |
| 400 | $0^{+0.006}_{-0.000} \pm 0.002$ | $0^{+0.105}_{-0.000} \pm 0.002$ | 5.6 | < 1.9 | < 3.4 | < 1.3 |
| 500 | $0^{+0.100}_{-0.000} \pm 0.001$ | $0^{+0.102}_{-0.000} \pm 0.002$ | 1.6 | < 1.9 | < 3.8 | < 1.3 |

the standard model width of the $W$ with decays available to three generations of light fermions. For lighter $W'$'s the top-quark decay channel may be fully or partially closed, but the limits presented below are insensitive to the $W'$'s intrinsic width, which is smeared out by detector effects. The Monte Carlo distributions $W(M_T)$ and $W'(M_T)$ were then obtained using a simple detector model, with nominal energy and momentum resolutions and a $\not{E}_T$ resolution determined from a full detector simulation. The distributions were normalized to the number of events expected in the data, assuming standard-strength couplings and the nominal branching ratios to each lepton family of $\frac{1}{9}$ for $W$'s and $\frac{1}{12}$ for $W'$'s. The result of the fit was a likelihood function for the $W'$ fraction $\alpha$ as a function of $M_{W'}$. The value of $\alpha$ is statistically consistent with zero for all values of $M_{W'}$. Fitted values of $\alpha$ are shown in Table I. For all $W'$ masses, the data are well fitted by $\beta = 0.92$–$0.94$.

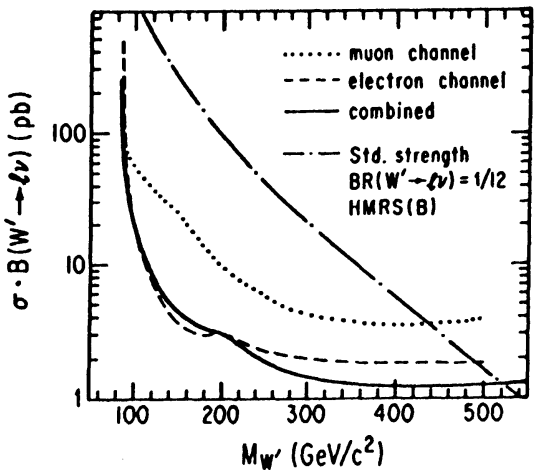


FIG. 2. The 95%-confidence-level limits on the cross section times branching ratio, $\sigma B$, for $W' \to \mu\nu$ (dotted line), $W' \to e\nu$ (dashed line), and combined (solid line). Also shown (dot-dashed line) is the predicted value, assuming standard-strength couplings to quarks and a branching ratio of $\frac{1}{12}$ to each lepton family.

Systematic uncertainties in this analysis are of two types: those that affect the shape of the Monte Carlo transverse mass distributions, and hence change the relative values of $\alpha$ and $\beta$, and those that affect only the overall event rates. Uncertainties of the first type are dominated by the uncertainties in the $W$ and $W'$ $P_T$ distributions. We have varied the $P_T$ of the $W$ and $W'$ by an overall scale of $\pm 25\%$, based on the theoretical error in the calculation, to assign these uncertainties, which are shown in Table I. Uncertainties of the second type include uncertainties in the lepton identification efficiencies and the overall 6.8% uncertainty in the luminosity normalization [5]. These uncertainties were incorporated into the likelihood function using a Monte Carlo procedure that has been used previously [6]. The resulting likelihood function was integrated to obtain the 95%-confidence-level limit on the $W'$ fraction in the data, as a function of $M_{W'}$.

These results, expressed as a limit on $\sigma B(W' \to l\nu)$, are shown in Table I and Fig. 2 for the electron, muon, and combined channels. If one assumes that the $W'$ has standard-strength couplings, these limits can be converted into a limit on the $W'$ mass itself. We emphasize that the limits on the cross section times branching ratio are independent of such assumptions. To calculate the standard-strength production cross section as a function of $M_{W'}$, we have used the HMRS(B) structure functions. Other recent structure function sets [9,10] bracket the HMRS(B) prediction and lead to similar mass limits to those given below (within $\pm 15$ GeV/$c^2$). For standard-strength couplings and a branching ratio of $\frac{1}{12}$ to each lepton family, the limit is $M_{W'} > 490$ GeV/$c^2$ in the electron channel, and $M_{W'} > 435$ GeV/$c^2$ in the muon channel, both at 95% confidence level. Combining the two channels we find $M_{W'} > 520$ GeV/$c^2$ at 95% confidence level.

We thank the Fermilab Accelerator Division and the technical and support staff of our respective institutions for their exceptional performance. We also thank Peter Arnold for making his $W$ and $W'$ $P_T$ distributions available to us. This work was supported by the Department

of Energy, the National Science Foundation, Istituto Nazionale di Fisica Nucleare, the Ministry of Science, Culture and Education of Japan, and the A. P. Sloan Foundation.

---

[a]Visitor.

[1] J. Pati and A. Salam, Phys. Rev. D **10**, 275 (1974); R. E. Marshak and R. N. Mohapatra, Phys. Lett. **91B**, 222 (1980).

[2] UA2 Collaboration, R. Ansari *et al.*, Phys. Lett. B **195**, 613 (1987); UA1 Collaboration, C. Albajar *et al.*, Z. Phys. C **44**, 15 (1989).

[3] J. Carr *et al.*, Phys. Rev. Lett. **51**, 627 (1983); A. E. Jodidio *et al.*, Phys. Rev. D **34**, 1967 (1986); **37**, 237(E) (1988); B. Balke *et al.*, Phys. Rev. D **37**, 587 (1988).

[4] F. Abe *et al.*, Nucl. Instrum. Methods Phys. Res., Sect. A **271**, 387 (1988).

[5] F. Abe *et al.*, Phys. Rev. D **44**, 29 (1991).

[6] F. Abe *et al.*, Phys. Rev. D **43**, 664 (1991).

[7] P. N. Harriman, A. D. Martin, R. G. Roberts, and W. J. Stirling, Phys. Rev. D **42**, 798 (1990).

[8] P. Arnold (private communication); P. Arnold and M. H. Reno, Phys. Rev. D **40**, 912 (1989); P. Arnold and R. Kauffman, Nucl. Phys. **B349**, 381 (1991).

[9] M. Diemoz, F. Ferroni, E. Longo, and G. Martinelli, Z. Phys. C **39**, 21 (1988).

[10] J. Morfin and W. K. Tung, Fermilab Reports No. Fermilab-Pub-90/74 and No. Fermilab-Pub-90/155 [Z. Phys. C (to be published)].

# REFERENCES


[1] T. D. Lee and C. N. Yang, Phys. Rev. **104**, 254 (1956).

[2] C. S. Wu *et al.*, Phys. Rev. **105**, 1413 (1957).

[3] M. L. Goldhaber, L. Grodzins, and A. Sunyar, Phys. Rev. **109**, 1015 (1958).

[4] S. L. Glashow, Nucl. Phys. **22**, 579 (1961).

[5] S. Weinberg, Phys. Rev. Lett **19**, 1264 (1967).

[6] A. Salam, in *Elementary Particle Theory*, N. Svartholm, editor (Almquist and Wiksells, Stockholm, 1968), p. 367.

[7] J. Pati and A. Salam, Phys. Rev. D. **10**, 275 (1974).

[8] R. N. Mohapatra and J. C. Pati, Phys. Rev. D. **11**, 566, 2558 (1975).

[9] G. Senjanovic and R. N. Mohapatra, Phys. Rev. D. **12**. 1520 (1975).

[10] Among the many good references on this subject are T. Cheng and L. Li, *Gauge Theory of Elementary Particle Physics*, (Oxford: Clarendon Press, 1984); I. J. R. Aitchison and A. J. G. Hey, *Gauge Theories in Particle Physics*, (Bristol: IOP Publishing Ltd., 1989); C. Quigg. *Gauge Theories of the Strong, Weak, and Electromagnetic Interactions*, (Menlo Park: Benjamin/Cummings, 1983).

[11] F. J. Hasert *et al.*, Phys. Lett. **46B**, 138 (1973); F. J. Hasert *et al.*, Nucl. Phys. **B73**, 1 (1974).

[12] G. Arnison *et al.*, Phys. Lett. **122B**, 103 (1983); G. Arnison *et al.*, Phys. Lett. **126B**, 398 (1983).

[13] M. Banner *et al.*, Phys. Lett. **122B**, 476 (1983).

[14] P. Bagnaia *et al.*, Phys. Lett. **129B**, 130 (1983).

[15] Here we follow the discussion in R. Mohapatra, *Unification and Supersymmetry*, (New York: Springer-Verlag, 1986), pp. 118-120.

[16] P. N. Harriman *et al.*, Phys. Rev. D. **42**, 798 (1990).

[17] F. Abe *et al.*, Phys. Rev. D. **45**, 3921 (1992).

[18] W. Marciano and A. Sirlin, Phys. Rev. D. **29**, 945 (1984); D. Bardin *et al.*, Z. Phys. **C32**, 121 (1986); U. Amaldi *et al.*, Phys. Rev. D. **36**, 1385 (1987); P. Langacker and M. Luo, Phys. Rev. D. **44**, 817 (1991); J. R. Carter, in Proceedings of the International Lepton-Photon Symposium, CERN, Geneva, 1991 (to be published).

[19] V. Barger and R. Phillips, *Collider Physics*, (Redwood City, CA: Academic Press, 1987), p. 239.

[20] Ibid, p. 260.

[21] UA1 Collaboration, R. Ansari *et al.*, Phys. Lett. **B195**, 613 (1987).

[22] UA2 Collaboration, C. Albajar *et al.*, Z. Phys. **C44**, 15 (1989).

[23] A. E. Jodidio *et al.*, Phys. Rev. D. **34**, 1967 (1986).

[24] B. Balke *et al.*, Phys. Rev. D. **37**, 587 (1988).

[25] J. Imazato *et al.*, Phys. Rev. Lett **69**, 877 (1992).

[26] G. Beall, M. Bender, and A. Soni, Phys. Rev. Lett **48**, 848 (1982); R. N. Mohapatra, G. Senjanovic, and M. Tran, Phys. Rev. D. **28**, 546 (1983); H. Harari and M. Leurer, Nucl. Phys. **B233**, 221 (1984); F. Gilman and M. H. Reno, Phys. Rev. D. **29**, 937 (1984).

[27] F. Abe *et al.*, Phys. Rev. Lett **67**, 2609 (1991). This paper is reproduced in Appendix B.

[28] M. J. Shochet, FERMILAB-CONF-91/341-E (1991) (to be published in the proceedings of the Les Houches Summer School, Particles in the 90's, Ecole d'Eté de Physique Théorique, Les Houches, France, June 30–July 26, 1991.)

[29] D. Möhl *et al.*, Phys. Rep. **58**, 73 (1980); D. Kline and C. Rubbia, Phys. Today **33**, 44 (Aug., 1980).

[30] S. Van Der Meer, "Stochastic Cooling of Betatron Oscillations at the ISR," CERN-ISR PO/72/31 (1972).

[31] "Fermilab Program through 1997 and Beyond," Supplemental materials submitted to the 1992 HEPAP Subpanel on their site visit to Fermilab, Feb. 27-28, 1992 (unpublished).

[32] See F. Abe *et al.*, Nucl. Inst. and Meth. **A271**, 387 (1988), and references therein.

[33] F. Snider *et al.*, Nucl. Inst. and Meth. **A268**, 75 (1988).

[34] F. Bedeschi *et al.*, Nucl. Inst. and Meth. **A268**, 50 (1988).

[35] F. Abe *et al.*, Phys. Rev. D. **43**, 2070 (1991).

[36] L. Balka *et al.*, Nucl. Inst. and Meth. **A267**, 272 (1988).

[37] S. R. Hahn *et al.*, Nucl. Inst. and Meth. **A267**, 351 (1988).

[38] K. Yasuoka *et al.*, Nucl. Inst. and Meth. **A267**, 315 (1988).

[39] S. Bertolucci *et al.*, Nucl. Inst. and Meth. **A267**, 301 (1988).

[40] F. Abe *et al.*, Phys. Rev. Lett **62**, 613 (1989).

[41] Y. Fukui *et al.*, Nucl. Inst. and Meth. **A267**, 280 (1988).

[42] G. Brandenburg *et al.*, Nucl. Inst. and Meth. **A267**, 257 (1988); C. Cihangir *et al.*, Nucl. Inst. and Meth. **A267**, 249 (1988).

[43] G. Ascoli *et al.*, Nucl. Inst. and Meth. **A268**, 33 (1988).

[44] K. Byrum *et al.*, Nucl. Inst. and Meth. **A268**, 46 (1988).

[45] F. Abe *et al.*, Nucl. Inst. and Meth. **A271**, 387 (1988).

[46] D. Amidei *et al.*, Nucl. Inst. and Meth. **A269**, 51 (1988).

[47] Aaron Roodman, Ph.D. thesis, University of Chicago, 1991.

[48] G. Ascoli *et al.*, Nucl. Inst. and Meth. **A269**, 63 (1988).

[49] A. Gauthier, CDF Internal Note 937.

[50] S. Eno, D. Kardelis, D. A. Smith, and R. Swartz, CDF Internal Note 1629.

[51] G. W. Foster *et al.*, Nucl. Inst. and Meth. **A269**, 93 (1988).

[52] A. Gauthier and D. Kardelis, CDF Internal Note 1106.

[53] Paul F. Derwent, Ph.D. thesis, University of Chicago, 1990; F. Abe *et al.*, Phys. Rev. D. **44**, 29 (1991).

[54] Just follow the simple instructions in the *CDF Offline Reference Guide*, Volumes I–IV.

[55] Electron identification in the CDF detector is discussed in detail in ref. [53].

[56] M. Miller, CDF Internal Note 1086.

[57] R. Swartz and D. Kardelis, CDF Internal Note 1220.

[58] J. P. Berge, private communication.

[59] A. Byon-Wagner *et al.*, CDF Internal Note 1260.

[60] C. Campagnari, CDF Internal Note 1025.

[61] D. Kardelis, CDF Internal Note 1301.

[62] M. Miller and P. Derwent, CDF Internal Note 1166.

[63] M. Gold, CDF Internal Note 913.

[64] M. Gold, CDF Internal Note 1161.

[65] Brian Winer, Ph.D. thesis, University of California, Berkeley, 1991; F. Abe *et al.*, Phys. Rev. Lett **66**, 2951 (1991).

[66] P. Arnold and M. H. Reno, Nucl. Phys. **B319**, 37 (1989); P. Arnold and M. H. Reno, Nucl. Phys. **B330**, 284(E) (1990).

[67] P. Arnold and R. P. Kauffman, Phys. Lett. **B349**, 381 (1991).

[68] P. Arnold, private communication.

[69] F. Paige and S. Protopopesceau, BNL Report No. BNL38034, 1986 (unpublished).

[70] F. E. James and M Roos, Comput. Phys. Commun. **10**, 343 (1975).

[71] Particle Data Group, G. P. Yost *et al.*, Phys. Lett. **B204**, 74 (1988).

[72] F. Abe *et al.*, Phys. Rev. Lett **69**, 28 (1992).

[73] C. Grosso-Pilcher and S. White, CDF Internal Note 1202; F. Abe *et al.*, Phys. Rev. D. **44**, 29 (1991).

[74] F. Abe *et al.*, Phys. Rev. D. **43**, 664 (1991); R. Hollebeek, P. Sinervo, J. Walsh, and H. Williams, CDF Internal Note 1016.

[75] F. Abe *et al.*, Phys. Rev. D. **45**, 1448 (1992).

[76] John Skarha, J. C. Yun, and Melissa Franklin, private communications.

[77] F. Abe *et al.*, Phys. Rev. D. **43**, 2070 (1991).